Disposal Package Design for Heat Generating High Level Waste

Group 4 - Conceptual Design Project (CDP)

Authors:
Pablo Hernández Fernández *(6368514)*
Elías Larrea Redondo *(6551645)*
Ana Santana Martín *(6374417)*
Jonas Ary Bergwerff *(5888808)*
Pietro Belloli *(6425526)*
Andrea Do *(6416047)*

Supervisors:
Dr. Erika Neeft
Dr. ir. Robin de Kruijff

Technical advisors:
Dr. Anne-Catherine Dieudonné
Ir. Martijn van Gent

2026-06-24

Contents

List of Figures

List of Tables

Listings

Nomenclature

Abbreviations

1D	1 Dimensional
2D	2 Dimensional
AM	Alumina Modulus
BF	Basalt Fibers
BP	Boiling Point
CAPEX	Capital Expenditures
CF	Cash flow
COVRA	Centrale Organisatie Voor Radioactief Afval
EBS	Engineered Barrier System
ECR	Effective Carbon Rates
EW	Exempt Waste
FU	Functional Unit
GDF	Geological Disposal Facility
GHGs	Greenhouse Gases
HAZOP	Hazard and Operability Study
HoQ	House of Quality
HRA	Hoogradioactief Afval
HSE	Health, Safety and Environmental
HVAC	Heating, ventilation and air conditioning
IAEA	International Atomic Energy Agency
IDLH	Immediately Dangerous to Life or Health
ILW	Intermediate Level Waste
ISrD	Inherent Safer Design
LCA	Life Cycle Assessment
LEU	Low Enriched Uranium
LILW	Low- and Intermediate-Level Waste
LLW	Low Level Waste
LMRA	Laag- en Middel Radioactief Afval
LSF	Lime Saturation Factor
MP	Melting Point
NORM	Naturally Occuring Radioactive Material

NPV	Net present value flow
OECD NEA	Organisation for Economic Co-operation and Development Nuclear Energy Agency
OPEX	Operational Expenditures
OSBL	Outside Battery Limits
P&ID	Piping and Instrumentation Diagram
PDI	Pressure Differential Controller
PEL	Permissible Exposure Limit
PET	Positron Emission Tomography
PFD	Process Flow Diagram
PFS	Plug Flow System
PIC	Pressure Indicating Controller
PID	Proportional–Integral–Derivative
PUREX	Plutonium Uranium Redox EXtraction
PWR	Pressurized water reactor
QFD	Quality Function Deployment
R&D	Research and Development
REL	Recommended Exposure Limit
SM	Silica Modulus
SNF	Spent Nuclear Fuel
SPECT	Single Photon Emission Computerized Tomography
ss	Stainless steel
TIC	Temperature Indicating Controller
TRIZ	Theory of Inventive Problem Solving
vHLW	Vitrified High Level Waste
VSLW	Very Short Lived Waste
VVER	Vodo-Vodyanoi Enyergeticheskiy Reaktor
WC	Working Capital

Symbols

ΔP	Pressure drop (bar)
$\dot{m}$	Mass flow (kg/s)
$\dot{V}$	Volumetric air flow rate (m^3/s)
λ	Thermal conductivity (W/mK)
μ	Attenuation coefficient(g/cm^2)
ρ	Density (kg/m^3)
ρ_u	Density air (kg/m^3)
$\sigma_{1,max}$	Maximum first principal stress (MPa)
θ	Angle degree ()
ε	Concrete porosity ($-$)
A	Area (m^2)
a	Cement characteristic parameter ($-$)
$A(t_{storage})$	Total gamma activity (Bq)
a_{CO_2}	CO_2 needed per m^3 carbonated (mol/m^3)
b	Cement characteristic parameter ($-$)
c	CO_2 concentration in air (mol/m^2)
C_{air}	Air entrainment coefficient ($-$)
C_{DPC}	Direct plant cost (€)
C_{DPI}	Direct permanent investment (€)
C_{env}	Environmental coefficient ($-$)
C_{kiln}	Cost of rotary kiln (€)
$c_{p,air}$	Specific heat capacity of air (kJ/(kgC))
C_s	Surface concentration (mol/m^3)
C_{TCI}	Total capital investment (€)
C_{TDC}	Total plant cost (€)
C_{TPI}	Total permanent investment (€)
C_x	Cl^- concentration (mol/m^3)
D	Diameter (m)
d	Falling distance (m)
d	Penetration depth (cm)
d_f	Falling distance (m)
d_v	Ventilation duct inner diameter (m)
D_{ax}	Axial dispersion coefficient ($-$)

D_{Cl}	Cl^- diffusion coefficient (m^2/s)
D_{CO_2}	CO_2 diffusion coefficient (m^2/s)
D_{rate}	Dose rate (Sv/s)
E/t_U	Expenses per tonne of uranium (€$/tonne$)
E_C	Modulus of elasticity ($-$)
$E_{\beta,max}$	Maximum beta decay energy (MeV)
E_{dep}	Energy deposited by gamma photon on worker (Bq)
E_{max}	Maximum gamma emission energy (keV)
E_X	Bremsstrahlung energy (MeV)
f	Darcy friction coefficient ($-$)
F_C	Construction factor ($-$)
F_M	Material of construction factor ($-$)
f_{ck}	Characteristic compressive strength (MPa)
$F_{clinker}$	Mass flow of clinker ($tonne/day$)
f_{cm}	Mean compressive strength (MPa)
F_{hit}	Fraction of emitted photons ()
F_{OSBL}	OSBL factor ($-$)
F_{PI}	Process type factor ($-$)
F_{PR}	Production rate factor ($-$)
g	Gravity (m/s^2)
H	Height (m)
I/t_U	Income per tonne of uranium (€$/tonne$)
I_i	Ray intensity ($-$)
K_{CO_2}	Carbonization coefficient ($ms^{1/2}$)
L_d	Length ventilation duct (m)
m	Mass (kg)
m_{worker}	Mass of worker (kg)
MC	Module cost (€)
N	Functional units ($-$)
n	Number of disposal packages per tunnel ($-$)
P	Pressure (bar)
P/t_{VW}	Disposal price per tonne of vitrified waste (€$/tonne$)
P_{design}	Operating pressure (bar)
P_{ref}	Reference pressure (bar)

Pe	Péclet number $(-)$
Q	Heat load (kW)
Q	Plant capacity (ton/year)
R	Mass ratio between reactor HLW and processed vHLW $(-)$
r_{ext}	Vitrified waste external radius (m)
R_{out}	Outer radius (m)
Re	Reynolds number $(-)$
S	Concrete saturation $(-)$
s	Reactors conversion $(-)$
S_p	Source term $(-)$
T	Temperature (K)
t	Time (s)
T_{cool}	Cooling temperature (C)
T_{in}	Inlet temperature (C)
T_{max}	Maximum temperature (C)
T_{ref}	Reference temperature (K)
u^*	Friction velocity (m/s)
V	Volume (m^3)
V_d	Disposal tunnel volume (m^3)
V_s	Shaft volume (m^3)
V_t	Transport tunnel volume (m^3)
v_v	Velocity air (m/s)
V_{tot}	Total excavation volume (m^3)
x_{Cl}	Cl^- penetration depth (m)
x_{CO_2}	CO_2 penetration depth (m)
Z	Atomic number $(-)$

Chemicals

^{137}Cs	Caesium-137
^{137}Th	Thulium-170
^{244}Cm	Curium-244
^{246}Cm	Curium-246
^{60}Co	Cobalt-60
^{90}Sr	Strontium-90
Al_2O_3	Aluminium oxide *(A)*
B_2O_3	Boron oxide
$Ca(OH)_2$	Calcium hydroxide
$Ca_2Al_2Fe_2O_5$	Tetracalcium alumino ferrite (C_4AF)
Ca_2SiO_4	Dicalcium silicate (C_2S)
$Ca_3Al_2O_6$	Tricalcium aluminate (C_3A)
Ca_3SiO_5	Tricalcium silicate (C_3S)
$CaCO_3$	Calcium carbonate
CaO	Calcium oxide *(C)*
$CaSO_4 \cdot 2\,H_2O$	Gypsum
$CaSO_4$	Calcium sulfate
Cl^-	Chloride ion
CO_2	Carbon dioxide
CO	Carbon monoxide
e^-	Electron
$Fe(OH)_2$	Iron (II) hydroxide
$Fe_2O_3\ \cdot H_2O$	Iron(III) oxide-hydroxide
Fe_2O_3	Iron(III) oxide *(F)*
Fe_3O_4	Magnetite
Fe^{2+}	Iron(II) ion
$FeCl_2 \cdot 4\,H_2O$	Iron(II) chloride tetrahydrate
$FeCl_2$	Iron(II) chloride
Fe	Iron
H^+	Proton
H_2CO_3	Carbonic acid
H_2O	Water
H_2	Molecular hydrogen

NO_x	Nitrogen oxides
O_2	Oxygen
OH^-	Hydroxide ion
Pu	Plutonium
SiO_2	Silicon oxide *(S)*
SO_2	Sulphur dioxide
U	Uranium

Abstract

Nuclear waste poses a danger to the public and the environment if not handled properly. Therefore, the processing, storage, and disposal of waste must be performed with the utmost care and precision. Among the nuclear waste, a small fraction is highly radioactive and heat-generating, and is consequently labelled High Level Waste (HLW). Management of this waste poses more challenges compared to others due to its large emission rates of ionising radiation and its heat-generating nature. In the Netherlands, the Centrale Organisatie Voor Radioactief Afval (COVRA) is responsible for the management of all nuclear waste produced within the country, including HLW. The current plan considered by COVRA for the disposal of HLW consists of its definitive emplacement in an underground disposal facility, after an initial period of over-ground storage.

Many aspects have to be considered in the design of such a disposal facility. Among these, this report mainly investigates the design of a disposal package encasing the HLW during the operational phase of the facility, and later acting as a component of a multi-barrier system separating the HLW from the outside environment. In addition to the disposal package, the emplacement of waste, as well as the operation and the backfilling of the facility tunnels are studied.

The final design consists of an external buffer composed of high-density magnetite concrete, and an internal carbon steel overpack containing the HLW canister. For the emplacement of the disposal package and for backfilling, an air-cushion supported vehicle and foamed concrete were respectively selected. All design choices are supported through a Quality Function Deployment (QFD), House of Quality (HoQ), and Pugh matrix assessment.

Regarding the core deliverable of the project, the design of a disposal package for heat generating HLW, the following properties were assessed as the main design drivers: radioactivity shielding, thermally induced mechanical stresses and corrosion.

The corrosion study put an emphasis on the first 1200 years of disposal, as during this period it is essential for the multi-barrier system to effectively prevent contact between pore water and the waste. It was found that corrosion does not pose a significant issue, to such an extent that introducing steel reinforcements into the concrete buffer layer could be feasible. However, due to the limited amount of literature available on this topic, the lack of sufficient experimental data, and the objective limitations in the corrosion assessment performed in this work, these results are not to be considered definitive. Rebar reinforcement was therefore not adopted, in line with the project's demonstrated technology requirement. Further evaluation in this aspect was found to be a future step of great importance.

A COMSOL model was used for the thermo-mechanical stress analysis, performing both steady-state and transient simulations of the stresses present in the disposal package. The main concern found for the disposal package was the cracking of the buffer due to large circumferential tensile stresses in its outer layers. Impact stresses were then also explored, finding that the buffer would experience tensile stresses far exceeding the tensile strength of concrete, even for drops as low as 2 cm. From this it is concluded that the disposal package should be handled with extreme care, and preventative measures should be taken to ensure its safe handling.

A ray-tracing software was developed to estimate the radiation doses to which workers will be exposed inside the disposal tunnels after emplacement. It was found that only gamma radiation will contribute significantly to radiation doses. Several scenarios considering the possible loss of shielding caused by damaging of the disposal package were assessed, indicating that the dose rates will be only lightly affected as long as such damage is minor. Highly dangerous rates were instead found in the case of major mechanical failure of the magnetite concrete shielding. Hence, to assess the hazard of ionization radiation a bow-tie diagram was developed to determine the control and mitigation barriers that would prevent the exposure of workers or equipment to the mentioned hazard.

Based on thermo-mechanical stresses and ionising radiation exposure, an optimization of pre-emplacement storage time and buffer radius was performed, indicating what values would exclude the failure of the containment function of this protection layer. The optimum for these paired parameters was found to be 90 years and 0.9 m.

An economic assessment was performed to estimate the total cost per disposed package in the disposal facility, as a function of disposal package radius. This analysis included material, handling, tunnelling, and other associated costs. The final estimate is of approximately 140 k€ per disposed package at a 0.9 m radius, with an associated carbon footprint of around 34 t of CO_2 per emplaced disposal package.

1 Introduction

The safe disposal of radioactive waste is crucial to protect human and environmental health. Different types of waste can present distinct types of radiation profiles, heat generation and half-lives, thus requiring specific shielding, encapsulation and heat dissipation. For further reference, in table 1, each type of waste was listed with its key characteristics and the required facilities for safe disposal. Despite representing less than 1% of total waste production volume, High Level Waste (HLW) disposal remains the most challenging due to its extreme radiological properties.

Table 1: Dutch nuclear waste classification per type[1].

Waste type	**Disposal facility**	**Characteristics**
Exempted	Exception	Activity and concentration are so low that monitoring is not necessary. Not treated as radioactive waste.
Short lived	Decay storage	Half life lower than 100 days. After sufficient temporary storage at the producer's premises, it can be treated as exempted waste.
Laag- en Midden Radioactief Afval (LMRA)	Storage, then underground disposal	Composed of items that contacted radioactive contaminants (gloves, clothing...) or small sources (calibration, smoke detectors). Consists of both long lived and short lived isotopes.
Naturally Occuring Radioactive Materials (NORM)	Storage, then underground disposal	Subcategory of LMRA waste referring to naturally occurring radioactive substances, concentrated by industrial processes (e.g. enrichment).
Hoogradioactief Afval (HRA)	Storage, then underground disposal	From spent nuclear fuel (SNF) reprocessing, fuel assemblies and medical isotopes production. Always requires heavy shielding, part of it is heat generating HLW.

The nuclear fuel cycle starts with the extraction and enrichment of uranium to produce electricity. This process generates SNF, which cannot be fully treated and reused, resulting in a waste stream of highly hazardous radioactive materials. SNF is usually composed of fission products ranging from bromine to the lanthanides, displaying higher nuclide concentrations around atomic numbers 95 and 137, as well as heavier minor actinides like americium, curium and neptunium[2]. While U and Pu can be separated and reprocessed, the remaining highly radioactive waste containing the aforementioned products and minor actinides, combined with neutron-activated metallic fuel assembly components, must be immobilised into a stable form before long-term storage and disposal.

Therefore, this project investigates the disposal of vitrified High Level Waste (vHLW), which is produced by mixing calcined HLW with borosilicate glass at high temperatures (1150-1200°C), forming a melt that is further poured into a stainless steel canister and subsequently welded shut[3, 4]. This study aims to explore several design alternatives for the disposal package, as well as a safe emplacement process in an underground disposal facility constructed in poorly indurated clay. In addition, other product-relevant processes were investigated, such as the manufacturing and assembly of the several components that form the disposal package and related phenomena to ensure their long-term stability.

To attain this goal, customer requirements from the Centrale Organisatie Voor Radioactief Afval (COVRA) were translated into engineering characteristics, via an opportunity assessment. These customer requirements were utilised to arrive at a final design concept. To assess the feasibility of the disposal package, a study was performed on corrosion effects, thermo-mechanical stresses and radiation shielding. Finally, environmental, health and sustainability considerations were studied in combination with an economical evaluation of the proposed solution to further investigate the feasibility of the project. This study preferentially applies industry-proven and established product and process methods for vHLW disposal.

It should be noted that, in addition to the disposal package, the backfill material was also explored, as its properties influence other aspects of the design. The disposal package, as well as the backfill both are part of a multi-barrier containment system (see figure 1), which makes use of both geological and engineered barriers. A good understanding of the different barriers is essential in assessing the other design aspects. The natural barrier system is formed by the surrounding rock formations and the Paleogenic clay host rock, which serves as an impermeable layer preventing the migration of ions, as well as offering a higher degree of isolation of the waste package. As for the engineered barriers, they consist of the waste form, a stainless steel canister, a carbon steel overpack, a concrete buffer, the tunnel backfill and the tunnel liner, which provide mechanical stability to the system, reducing the risk of crack formation and low permeability to reduce radionuclide migration into the environment[5].

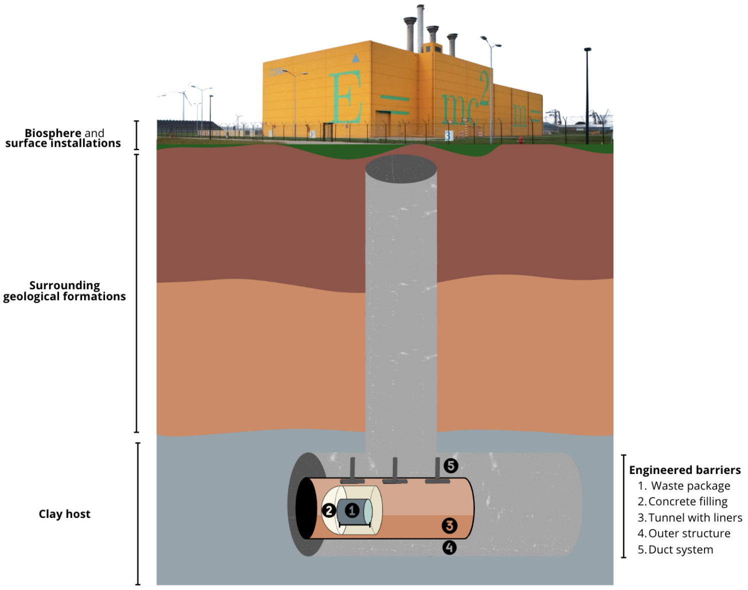

Figure 1: Visualisation of a geological disposal facility for HLW disposal.

2 Concept stage

2.1 Market analysis

2.1.1 COVRA's current role and future outlook

The principal of this design report is COVRA, the sole entity in the Netherlands responsible for radioactive waste management, as its operations are mainly dictated by safety requirements and government regulations instead of market competition[6]. COVRA's activities comprise temporary storage and future disposal of radioactive waste, which is carried out in cooperation with the International Atomic Energy Agency (IAEA), the Organisation for Economic Co-operation and Development (OECD), and the Nuclear Energy Agency (NEA).

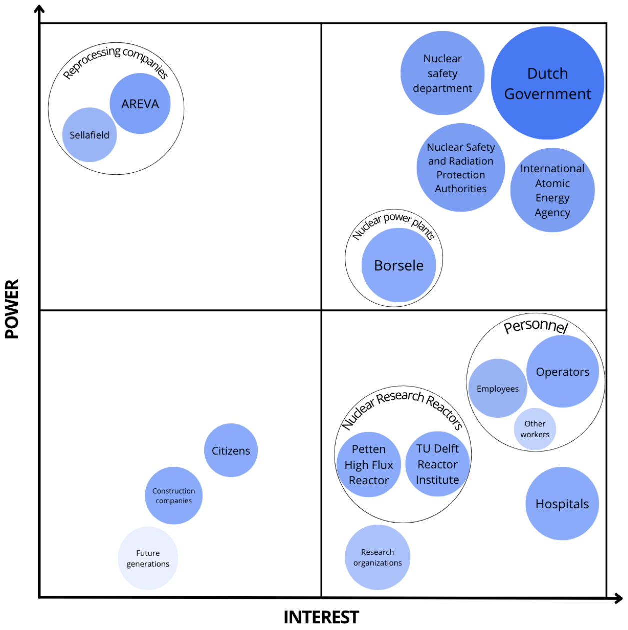

Figure 2: COVRA's stakeholder mapping (darker color and larger size indicate higher importance).

COVRA's customers include nuclear power plants, hospitals, research centres, and industrial facilities generating radioactive waste. Its broader stakeholder network comprises government organisations, suppliers, and public groups such as academic institutions, which have been classified by influence and interest, as shown in figure 2, to guide engagement strategies[1]. COVRA's future plans include the construction of a deep geological disposal facility in Paleogene clay formations, selected for their low permeability, which limits radionuclide migration, and shows self-healing properties. The facility will be located 200-1000 m below the surface, consisting of a tunnel network connected to the surface via vertical shafts[5].

2.1.2 Economic impact of a monopoly

A relevant factor that must be considered due to its unusual occurrence in the chemical engineering field is the presence of a monopoly: COVRA is the only company that handles nuclear waste generated in the Netherlands[6], with no competitors present in the country. This entails control by the company over the totality of the market, a position which can be translated into a high control over pricing and elimination of customer choice. Furthermore, lack of competitive pressure could devolve into a relaxation of the scrutiny with which activities are performed, as well as a deceleration in Research and Development (R&D) efforts due to the lack of a necessity to improve current technology.

In contrast, this unique market positioning also offers some significant advantages, especially valuable in a field operating on very long time-scales, and requiring maximal levels of safety. Indeed, the lack of a market push to increase profit margins or to generate rapid returns for investors, makes COVRA able to place the safety of their geological disposal facility and the reliability of the multi-barrier system constructed above all other requirements.

2.1.3 Value chain analysis

COVRA operates at the end of several value chains, including the nuclear power generation and radionuclide enrichment and generation for (non-)medical applications. For example, the value chain for nuclear power generation and COVRA's position therein is illustrated in figure 3. Here, it can be seen that the nuclear power generation value chain contains some steps, of which COVRA is active in the last two, namely the treatment, storage and disposal. Most monetary value is created in the earlier steps, where ore is mined and converted into valuable fuel for nuclear reactors, followed by the generation of electricity. The position where COVRA operates generates relatively low profit, however, it does provide immense societal value, as the safe storage and disposal of highly radioactive waste is essential in ensuring the safety of the public.

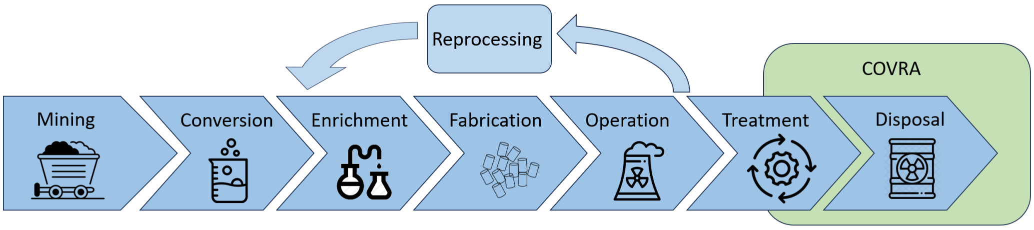

Figure 3: Nuclear power generation value chain, including COVRA's position in this value chain.

2.2 Technical requirements

As mentioned before, this project will primarily focus on the design of the disposal package while considering backfill and emplacement methods. Thermo-mechanical and radiological assessments during different stages of operation will determine the final design. Overpack manufacturing and buffer casting (with or without reinforcements) directly around the vHLW canister, the emplacement process and the backfill used to seal off the disposal tunnels, will be also studied. Based on the project scope and stakeholder expectations, the following main customer requirements can be highlighted: safety of the system with respect to ionising radiation, resistance to environmental conditions, and safe handling and placement.

The Quality Function Deployment (QFD) was the method selected to translate the customer requirements to engineering properties. A House of Quality (HoQ) was constructed for each design aspect to relate customer needs to technical parameters (see figures A1, A2 and A3). As a result, a relative weight was calculated for each functional requirement in the disposal package, the backfill and the emplacement method; reflecting the importance of different design options and the results shown in table 2.

---

[1] The classification of stakeholders was covered during lectures of CH3803 by A. de Haan.

Table 2: Most relevant characteristics within the time frame of interest (∼1200 years: as long as the host rock is heated by the vHLW) as identified via the House of Quality methodology.

House of Quality category	Quality Characteristic	Relative weight per category (%)	Importance
Disposal package	Package geometry (including optimal carbon overpack sizing with/out reinforced concrete)	13.0	Promote efficient packing in geological disposal facility
	Package size	12.6	Be able to enclose the container
	Permeability	12.4	Prevent diffusion of ions and water in/out of the canister
Backfill	Composition	14.1	Match design requirements of flowability and thermo-mechanical resistance
	Tensile strength	12.2	Resist mechanical loads and geological movements
	Flexural strength	12.2	Resist mechanical loads and geological movements
Emplacement Method	Remote control system of machinery	30.7	Reduce radiation exposure
	Energy efficient system	14.2	Reduce cost of operation
	Wear resistance	12.7	System reliability

3 Product concept options and selection

In the design of the disposal package, two configurations are explored. The first consists of a carbon steel overpack around the waste canister, with a buffer encasing it. The other design omits the overpack and instead relies on the mechanical strength added through rebar reinforcements. In addition, the emplacement process and tunnel backfill were also investigated. Once the most relevant engineering characteristics were identified with a QFD analysis, a Pugh matrix was then used to compare and select the best options for the concepts of the disposal package, emplacement method, and backfill.

Each concept was evaluated against the currently considered design, which utilises an overpack with a concrete buffer. Several criteria were formed based on the customer requirements and applied to the concepts. The selected criteria include safety, resistance to environmental conditions, mechanical performance, durability and cost. Each concept is compared to the reference using a simple scale, where green indicates better performance, orange similar performance and red worse performance.

3.1 Disposal package

The disposal package is set to satisfy a number of requirements. It should provide adequate shielding in order to limit the additional radiation dose to workers to 6 mSv per year. It should prevent the ingress of water for as long as the host rock is being heated by the vHLW, which is approximately 1200 years[5]. It should withstand the thermo-mechanical stress present due to the heat-generating nature of the vHLW. Another important design requirement is that the disposal package should be made from materials with demonstrated and well-understood physical and chemical characteristics.

Using several creative ideation methods, a large number of concepts were generated. Out of these concepts, four designs were chosen to be investigated further. The concepts consist of three options which make use of a carbon steel overpack around the vHLW canister, surrounded by a buffer made from various materials. The last option consists of a rebar-reinforced concrete disposal package, without the overpack. A graphical representation of these concepts is shown in figure 4. The different options are outlined below:

- **Bentonite:** Bentonite consists for the most part of montmorillonite, a type of phyllosilicate mineral. This material has been explored in multiple studies dating back to the 1970s for its use in disposal facilities[7–9]. The main advantages are the low hydraulic permeability and self-healing abilities due to its swelling pressure[7]. Its primary downside is that it cannot be cast as regular concrete and either has to be compacted around the HLW in-situ, or mixed in with concrete[10].

- **Concrete with magnetite aggregates:** This concept makes use of the addition of magnetite to the concrete to increase its radioactive shielding performance. The chemical composition of magnetite is $Fe^{2+}Fe^{3+}_2O_4$, being an oxide it shows excellent chemical stability. The regular aggregate in concrete can be (partially) replaced by magnetite, which will increase the density and linear attenuation coefficient (LAC). This has been the subject of numerous studies[11–13]. A main advantage of this approach is that the strength of the concrete remains suitable for the buffer[14]. A downside of the aggregate is that the higher density aggregates require better mixing to ensure a homogeneous casting[15].

- **Concrete with basalt fibres:** Similar to the last concept, but instead of magnetite, basalt fibres (BF) are added. These fibres consist of mostly silica, with alumina, iron oxides and calcium oxide making up the rest of the composition[16]. This composition makes it chemically very inert, testing has also shown a good resistance to γ radiation[16]. The addition of BF is found to increase mechanical performance and ductility of the concrete samples[17]. Furthermore, research has shown that including BF also increases the shielding of the concrete[18–20]. This concept combines better shielding with increased strength. However BF concrete is much more expensive with a production process that requires very high temperatures and provides less radiation shielding than magnetite[21].

- **Reinforced concrete buffer without overpack:** This concept utilises rebar-reinforced concrete to provide additional strength. Due to this increase in mechanical strength, the overpack can be omitted. Reinforced concrete is one of the most used materials in the world which means its behaviour is well-understood[22]. The higher mechanical strength of the reinforced concrete would lower the chance of fracturing due to tensile forces[23] and scores as well as the basalt fibre concept. There are some concerns regarding post-closure stability due to the corrosion of the rebar, as it sits closer to the outer surface of the disposal package, which could lead to premature failure of the buffer[23].

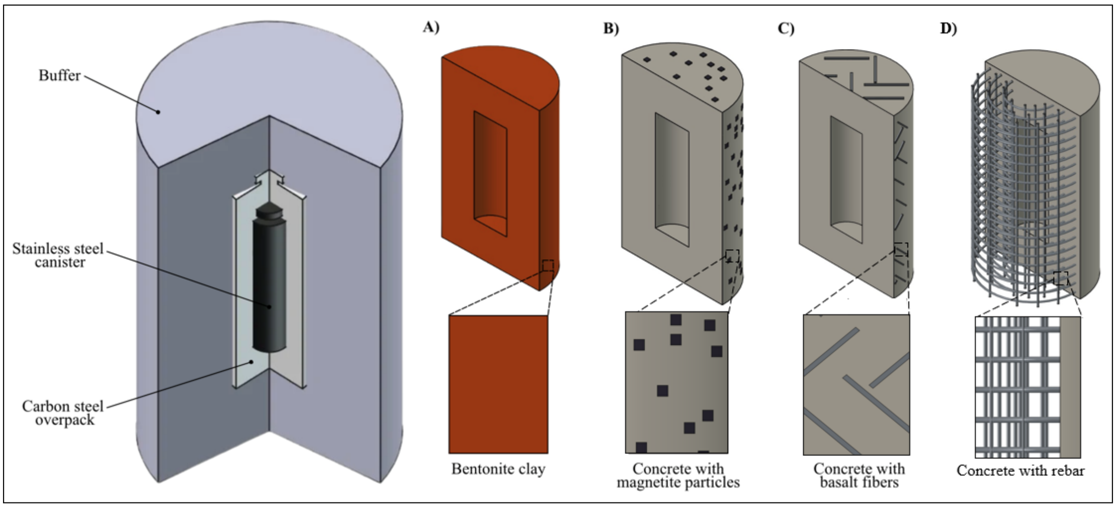

Figure 4: Disposal package design options: bentonite (A), concrete with magnetite (B), concrete with basalt fibres (C), and rebar-reinforced concrete without overpack (D).

To judge which disposal package concept would be most suitable, the four ideas are compared with the properties of concrete mixtures commonly used in civil engineering applications such as ordinary Portland cement concrete. The concepts are judged on six aspects: mechanical strength covers compressive and tensile strength. The cost covers an estimated cost per disposal package. The radiation shielding is based on attenuation coefficients and penetration depths. The density is taken as the bulk property of the selected material. The permeability is based on diffusion coefficients and permeabilities found in literature. The corrosion resistance is based on the alkalinity of the medium, combined with chemical stability, taking into account the distance moisture and other chemical species have to travel in order to reach corrosion-sensitive materials.

Table 3: Pugh matrix for different disposal package designs.

Concepts	**Mechanical strength**	**Cost**	**Radiation shielding**	**Density**	**Permeability**	**Corrosion resistance**
Bentonite (1a)	🟥	🟧	🟧	🟥	🟩	🟩
Magnetite (1b)	🟧	🟧	🟩	🟩	🟧	🟩
Basalt fibres (1c)	🟩	🟧	🟧	🟧	🟧	🟩
Rebar-reinforced (1d)	🟩	🟩	🟧	🟧	🟧	🟥

From the matrix, concept 1b (magnetite) scores the best. However, it does fall short of basalt fibre-reinforced concrete in mechanical strength, and it falls behind bentonite in terms of permeability. The rebar-reinforced option scores similarly to the basalt fibre concept, but since the rebar is present closer to the outer surface, corrosion may become an issue in earlier stages. In an ideal case, a combination of magnetite and basalt fibres should be taken. This will lead to improved mechanical strength and shielding. However, no literature is available covering the properties of concrete with both magnetite and basalt fibres. Since only known and applied materials are suitable for this project, this combination cannot be used, and instead the magnetite concrete is taken as the final concept. To summarise, basalt fibres will allow for greater tensile strength, magnetite will lead to major improvements in shielding, and bentonite will lower permeability. It is assumed here that shielding will be the limiting factor determining buffer diameter, and therefore magnetite aggregates are selected.

3.2 Emplacement

The emplacement includes the movement of the disposal package from its casting place to the disposal tunnels, more specifically including the transportation from its casting location to the elevator shaft leading into the subterranean disposal facility, the lowering of the disposal package, and the transport from the elevator to the final disposal location within the tunnels. Since each step would require a different system and, with that, its own research, it was decided to limit the scope of this project to the subterranean transport of the disposal package.

The most important factors to consider for the emplacement are reliability, since a failure of the systems carrying highly radioactive waste has to be avoided at all cost. The system should be compact to save on tunnelling costs, and it should limit the radiation exposure to workers, either by remote control or shielding. Three concepts were selected, a visual representation is shown in figure 5. The emplacement techniques are explained below:

- **Rail-based transportation:** For this system, tracks have to be installed throughout the subterranean facility. The disposal package can be loaded onto a carrier wagon, a remotely controlled electric locomotive is used to move the wagon carrying the disposal package to its designated tunnel. After it has been moved to its place, the locomotive will decouple, leaving the disposal package and wagon behind.
- **Air Cushion Transport:** This system makes use of a thin air film beneath a rubber seal to lift heavy objects with little friction. In this case, the disposal package would be loaded onto the transporter and subsequently moved to its resting place, after which it has to be unloaded again. Since the air cushion system has no inherent directionality, either workers or a motorised vehicle would have to be used. A downside of this method is that it requires a very flat floor, otherwise the air film will not be able to form.
- **Drum-transporters:** Here, a custom-built machine would have to be used. Similar machines are used for the transportation of drums[24]. Again, the machine would be loaded with the disposal package at the elevator and subsequently moved through the facility, unloading it at its designated location. An advantage of this system is that it can be compact, and no material is left with the disposal package, unlike with the rail-based alternative. This machine could be designed to be remotely controlled or automated to prevent excessive exposure to radiation.

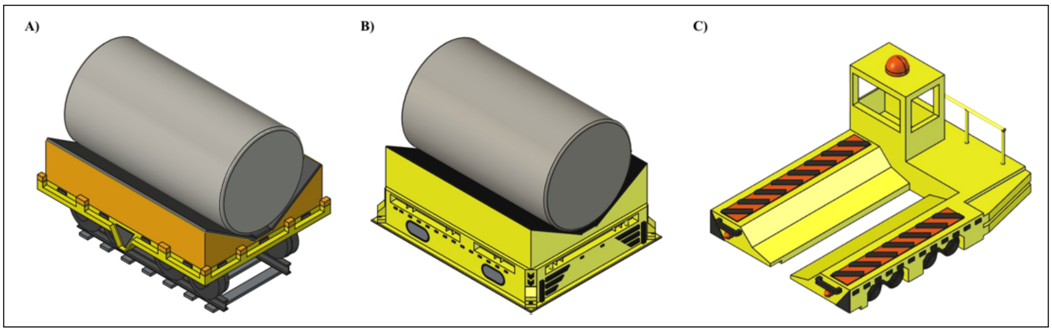

Figure 5: Emplacement system options: rail-based (A), air-cushion (B) and drum transporter (C).

For the emplacement system, the scoring was not performed based on a comparison to a particular type of emplacement. Instead, the following colour scheme is used: red indicates expected difficulties, such as insufficient load capacity; orange indicates expected sufficient performance, but improvements are possible; green indicates expected excellent performance.

The concepts are judged on six criteria. Load capacity covers the expected load the emplacement system can handle. Placement time covers the expected time for the emplacement of a single disposal package. The reliability takes into account the mechanical complexity and reliability of the machines used. The installation cost covers the expenses of preparing the tunnels for use of this system (laying tracks, preparing floors), together with the expected cost of the machine itself. The remote operability judges based on the extent to which the system can be operated remotely/autonomously. The post-closure criteria take into account possible problems arising after pouring the backfill due to the emplacement method.

Table 4: Pugh matrix for the different emplacement methods.

Concepts	**Load capacity**	**Placement time**	**Reliability**	**Installation cost**	**Remote operability**	**Post-closure**
Rail-based (2a)	🟩	🟩	🟩	🟥	🟩	🟥
Air-cushion (2b)	🟩	🟧	🟧	🟧	🟧	🟩
Drum transporter (2c)	🟥	🟩	🟩	🟩	🟩	🟩

Based on the matrix, concept 2c (drum-transporter) appears to be the most suitable. However, no data was readily available for machines with a suitable capacity to move a concrete cylinder of dimensions (2.5x2 m d x h) with a safety margin. The air cushion transporter does have the capacity, however, it performs worse in emplacement time, reliability, installation cost and remote operability. The rail transport option suffers from a high installation cost due to the need for an extensive track and switch system. The steel rails can start to corrode post-closure, which could lead to damage to the backfill caused by gas accumulation or expansion of the corroding metal, making this concept not seem as suitable.

Since the drum transporter option performs well everywhere except for the load capacity, it was chosen to combine this concept with the air cushion, giving rise to the concept of an air-cushion drum transporter. This combined concept will have the required load capacity, at the cost of a slightly worse emplacement time and reliability.

3.3 Backfill

The backfill is another part of the system that was investigated, since the type of backfill will influence the diffusion of water towards the disposal package. After the placement of the disposal packages into the disposal tunnel, a 10 year observation period is taken. After this time, the rest of the tunnel will be backfilled using a cementitious or clay-like substance (see figure 6). This backfill is meant as the final closure of the tunnel system, permanently locking the buffers in place and working as an additional engineered barrier[5, 25, 26]. Backfill materials have been researched in several studies[5, 26]. However, the nature of the geological site will inherently change the backfill material used for the specific case. Therefore, only concepts applied in disposal facilities in clay layers were considered for this project.

The backfill has similar requirements to the disposal package, however, the thermally induced stress is not considered. The backfill will be further away from the heat source, leading to a lower heat flux per volume. This will result in lower temperature gradients and therefore lower thermal-mechanical stress. The radiation shielding is also less important, since after the backfill is in place, it will not be possible to get close to the containers. The backfill should work as an additional barrier against water ingress, and it should be resistant to cracking. Since a larger volume of backfill is required compared to the disposal package, the cost becomes a more important factor for the considerations. Different material types were considered, as well as options for the method of placing the backfill. Combining the material options and placement methods yielded the following concepts:

- **Compacted bentonite:** For this concept, highly compacted bentonite blocks or pellets would be installed around the disposal package to fill out the tunnels. They would act as the primary hydraulic sealing barrier, as upon contact, bentonite readily absorbs water and swells. This generates a swelling pressure, allowing it to seal any fractures. Bentonite also has great thermal stability[27].
- **Claystone-bentonite mixture:** For this concept, bentonite is mixed with crushed claystone sourced from sedimentary rock and clay minerals such as argillite. This makes use of the higher structural strength of the claystone while maintaining the swelling and sealing behaviour of bentonite[28]. This mixture was found to show excellent swelling performance, low permeability, and low gas migration[29]. In research, a 7:3 claystone:bentonite ratio was found to perform best. The research performed on this mixture was done in the HADES project in Belgium, which tested it in Boom Clay, making this a suitable backfill for disposal facilities in Paleogene clay. A downside is the emplacement, as the mixture showed poor flowability during backfilling[29].

- **Foamed concrete:** This concept explores a low-density cementitious material, saturated with air pores, created through foaming agents. Foamed concrete has decent thermal insulation and structural support, with a relatively short curing time as the pores relieve vapour pressures and adapt to the deformations generated by thermo-mechanical stress. This material is inexpensive, well-studied and has good flowability. However, it has a higher permeability than the bentonite-based concepts[30–32]. In the work of *Sycheva et al.*[33], foamed concrete of class D700 shows great thermal and mechanical performance up to a temperature of $400°C$, which is significantly higher than the maximum expected temperature of <100°C. Furthermore, during long-term exposure to elevated temperatures, the formation of calcium hydrosilicates sites occurs, increasing the thermal stability[33].

For the backfill, the selected options will be compared to a generic concrete backfill. The concepts are judged based on five criteria. Mechanical strength covers multiple aspects, of which compressive strength is the most important. The cost covers the volumetric cost of the different materials. This factor is more important for the backfill since a larger volume will be required than for the disposal packages. The temperature stability is important since the vHLW generates heat, which means the backfill has to sustain elevated temperatures, around 60°C according to initial estimations, for long time periods. The permeability dictates the rate at which moisture is able to permeate through the backfill. The flowability indicates how easy this material can be pumped, which is important for the filling process.

Table 5: Pugh matrix for the backfill materials.

Concepts	**Mechanical strength**	**Cost**	**Temperature stability**	**Permeability**	**Flowability**
Bentonite (3a)	🟧	🟥	🟧	🟩	🟥
Claystone-bentonite (3b)	🟩	🟧	🟧	🟩	🟥
Foamed concrete (3c)	🟩	🟩	🟩	🟥	🟩

Based on the Pugh matrix, foamed concrete appears to be the best option, only lacking in terms of permeability. However, its better flowability is considered to be more important, as a worse flowability means the backfilling process will require more labour, increasing the radiation exposure of workers. Therefore, the foamed concrete is selected as the final concept for the backfill. Foamed concrete shows great mechanical and thermal stability, with a relatively low permeability. Furthermore, this material was also selected by a previous report released by COVRA[5]. Hence, the vHLW waste canisters will be stored as it is shown in the figure 6, where the canister is surrounded by a magnetite buffer and placed in a pre-filled foamed concrete divot. After that the whole tunnel will be filled with foamed concrete.

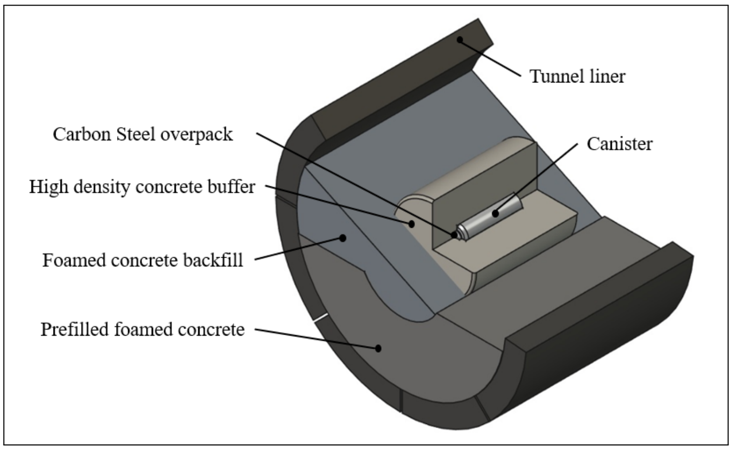

Figure 6: Sketch of the disposal tunnel (see dimensions in Table A1).

3.3.1 Backfill placement

For the placement of the backfill, multiple options are possible. Since the chosen backfill material is foamed concrete, this can be pumped relatively easily into the tunnels and requires no vibration to settle[34]. How the concrete is deposited throughout the entire tunnel is a bigger challenge. Previous work by COVRA has suggested the use of the air ducts to position the concrete delivery pipes[5]. However, during the backfilling process, this would require the continuous removal of duct sections since no material should be left in the tunnels. Instead of this, it is opted to first fully retract the venting system and use the mounting system for the duct to place a retractable concrete pipe all the way to the back of the tunnel. This can be used to fill the tunnel from the back to the front, retracting the concrete line in the process.

To ensure a homogeneous backfill, the floor is cast using the same material. However, the flooring has to incorporate some additional functions. Since the buffer is cylindrical, a divot in the flooring is made. This divot can be designed to ensure good alignment of the buffer within the tunnel, as well as preventing further movement after placing. Additionally, an epoxy coating has to be applied to the floor to allow for the use of the air-cushion vehicle, as these require a very flat floor to operate.

3.4 Final concept selection

Based on the analysis of the options for the buffer, emplacement and backfill. Three concepts were selected as shown in figure 7: a buffer made from concrete with magnetite aggregate, which will be emplaced using an air-cushion drum loading vehicle, after which the tunnels will be backfilled using foamed concrete.

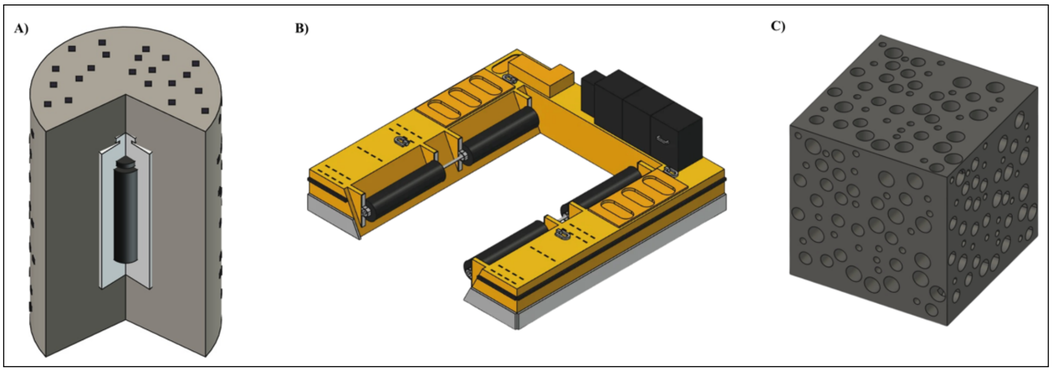

Figure 7: Final concept selection: concrete with magnetite buffer (A), air-cushion drum transporter vehicle (B) and low-density foamed concrete backfill (C).

4 Product concept assessment

4.1 Corrosion effects analysis

Corrosion of ferrous materials within the disposal package could lead to its failure before the intended lifespan of 1200 years is reached, thus an assessment of this phenomenon was conducted to validate the long-term stability of the design. Concrete provides high protection against corrosion under strongly basic conditions (pH ≈ 13), which is further improved by a low water/cement ratio to reduce the material's permeability. Under these conditions, a thin, passive oxide film forms on the steel surface, limiting corrosion to rates below 1μm per year[5, 35]. However, this protection isn't unconditional as carbonation and the diffusion of chloride ions through the concrete can degrade the passive film [36].

Moreover, the ingress of water inside the concrete can lead to anoxic corrosion[37], generating hydrogen gas and potentially damaging the multi-barrier engineered system[38, 39]. Under anoxic conditions the steel can be oxidised due to water reduction[36]. The water in the pores of the concrete leads to the dissolution of iron ions on the anode side and resulting in a loss of metal mass (reaction R1).

$$\mathrm{Fe} \rightarrow \mathrm{Fe}^{2+} + 2\mathrm{e}^- \tag{R1}$$

$$\mathrm{H_2O} + \frac{1}{2}\mathrm{O_2} + 2\mathrm{e}^- \rightarrow 2\,\mathrm{OH}^- \tag{R2}$$

$$2\mathrm{H}^+ + 2\mathrm{e}^- \rightarrow \mathrm{H_2} \tag{R3}$$

The overall redox reaction under aerobic conditions is given in reaction R4, where ferrous hydroxide was produced, and subsequently, after further oxidation and hydration were performed to produce ferric hydroxide (reaction R5)[40]. Finally, hydrated ferric oxide (rust) was produced as shown in reaction R6. Based on the Pourbaix diagram (see figure B1) at pH>10, the product R6 is thermodynamically stable, which offers a protective passivation film, R4 and R5 are intermediates. However, due to the non-homogeneous nature of concrete, there is more or less pore water in different zones. This means that in zones with more moisture, the formation of hydroxides is preferred, while drier zones result in oxide formation, thus both forms can coexist[41].

$$2\,Fe + O_2 + 2\,H_2O \rightarrow 2\,Fe(OH)_2 \tag{R4}$$

$$4\,Fe(OH)_2 + O_2 + 2\,H_2O \rightarrow 4\,Fe(OH)_3 \tag{R5}$$

$$2\,Fe(OH)_3 \rightarrow Fe_2O_3 \cdot H_2O + 2\,H_2O \tag{R6}$$

Under sealed underground conditions, oxygen is rapidly depleted, thus the predominant reduction process that occurs is reaction R3, which results in the formation of hydrogen gas and magnetite (reaction R7), a stable product based on the Pourbaix diagram. In figure 8, a schematic representation of the process under these conditions showcases the problem of the formation of rust and volatile gases.

$$3\,Fe + 4\,H_2O \rightarrow Fe_3O_4 + 4\,H_2 \tag{R7}$$

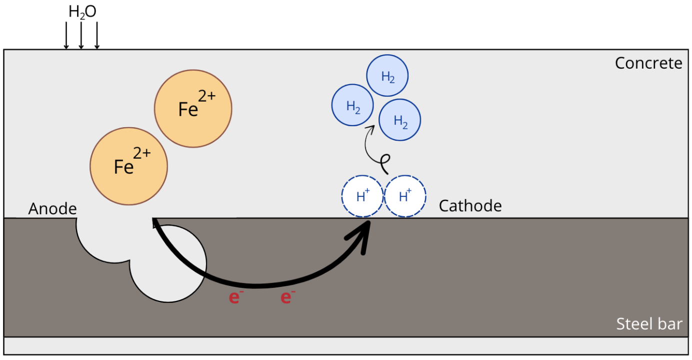

Figure 8: Simplified scheme of concrete reinforcement corrosion process under anoxic conditions.

The inclusion of steel rebar as reinforcement in the concrete buffer raises significant corrosion concerns. Corrosion of embedded steel produces solid oxide and hydroxide. These corrosion (rusting) products occupy substantially greater volumes than the original metal between 2 and 6.5 times the volume of the original steel bar as seen in Appendix B1. [42]. This volumetric expansion generates internal tensile stresses in the concrete, which can lead to micro-cracking, spalling, and ultimately loss of structural integrity[43, 44]. In addition, these expansive forces can also cause longitudinal splitting along the rebar when the concrete cover is insufficient to resist such forces[45, 46].

In addition, under anoxic conditions, water reduction becomes the dominant reduction reaction, which produces hydrogen gas, which the accumulation of, may significantly cause failure of the multi-engineered barrier[36, 39]. If hydrogen cannot be evacuated at the rate at which it is produced, gas will accumulate and, due to the hydrostatic pressure, low permeability of the surrounding barriers and low solubility of hydrogen gas, this could lead to very high hydrogen pressures and create additional internal pressure that further contributes to cracking[43–46].

For example, in bentonite, once the buffer is saturated, due to the extremely low permeability and high capillary entry pressure, gas, such as hydrogen, accumulates and can generate internal pressures of 4-30 MPa. At these conditions, three gas breakthrough mechanisms are possible: capillary, which is the displacement of pore water; mechanical, when gas pressure approaches the minimum principal stress of the buffer, physically fracturing the material along preferential pathways; and interfacial, which occurs along construction interfaces between materials[38, 43–45]. Therefore, the main corrosion mechanisms relevant to the proposed disposal system were further analysed through the effect of carbonation and chloride diffusion.

4.1.1 Carbonation-induced corrosion

Carbonation occurs when atmospheric CO_2 dissolves in the concrete pore water to form carbonic acid (H_2CO_3), which then reacts with the calcium hydroxide present in the cement formulation to produce calcium carbonate ($CaCO_3$), lowering the pH from 13 to below 9. At these conditions, the passive protective layer of the reinforcements is no longer stable, and corrosion can initiate on the steel surface, in the presence of water or oxygen[36]. The reactions occurring during this process are shown in R8 and R9.

$$CO_2 + H_2O \rightarrow H_2CO_3 \tag{R8}$$

$$Ca(OH)_2 + H_2CO_3 \rightarrow CaCO_3 + 2\,H_2O \tag{R9}$$

Therefore, one of the main factors that affects this process is the concentration of carbon dioxide, making penetration depth analysis a crucial assessment to estimate corrosion, structural damage, and lifespan shortening for the structure due to carbonation[47]. Nevertheless, other environmental factors, namely humidity and temperature, as well as concrete-related properties, such as water to cement ratio and porosity, may amplify the negative effects of this process[48]. The main problem studied here is the contact between the carbonation layer and the steel of the rebar, or other steel elements inside the concrete[47].

Several models have been developed to calculate the diffusion coefficient, but most heavily depend on experimental measurements of the properties of the concrete structure at the time of the testing [47]. Among these, for a theoretical approach, equations 1 and 2[48] are selected. In this method the penetration depth (x_{CO_2}) was computed as a function of a carbonization coefficient (K_{CO_2}), time (t), characteristic concrete strength (f_{ck}) and several standardised coefficients in alignment with the European code, namely environment (C_{env}=0.2), air entrainment (C_{air}=1) and based on the cement type (a=1800; b=-1.7). As a result, it was obtained that in the timespan before backfilling ($\sim$ 10 years) the penetration of CO_2 would be approximately 1.9mm.

$$x_{CO_2}(t) = K_{CO_2} \cdot \sqrt{t} \tag{1}$$

$$K_{CO_2} = C_{env} \cdot C_{air} \cdot a \cdot (f_{ck} + 8)^b \tag{2}$$

Moreover, to verify the results obtained with the first model, K_{CO_2} was defined as formulated in equation 3[49], with D_{CO_2} the diffusion of CO_2 into the concrete, c the amount of CO_2 in the atmosphere (430 ppm[50]) and a_{CO_2} the amount of CO_2 needed for m^3 carbonated.

$$K_{CO_2} = \sqrt{\frac{2D_{CO_2} \cdot c}{a_{CO_2}}} \tag{3}$$

The parameter a represents the maximum amount of CO_2 that reacts inside the concrete (see equation B1). Calculating it requires the concentration of $Ca(OH)_2$ in concrete, as it is the reactant that is transformed into $CaCO_3$ (as shown in reaction R9). $Ca(OH)_2$ is produced when CaO in cement undergoes a hydration reaction as cement is being mixed with water to create concrete. As all the reactions have a 1:1 stoichiometry, the number of moles of CO_2 that reacts inside the concrete are equal to the number of moles of CaO inside the cement. For the disposal container, the amount of CaO is 2867.33 mol_{CO_2}/m^3 using the data from chapter 5. Moreover, the variable c is the CO_2 concentration in air, for which a value of 430 ppm was used, giving rise to a value of 0.0176 mol of CO_2 per cubic meter (see equation B2)[50].

The diffusion of CO_2 through concrete can be calculated using the formula 4[50]. In this scenario, the temperature was estimated to be 50°C and pressure 1 atm, while the reference temperature and pressure were 25°C and 1 atm, respectively. Moreover, S is the saturation degree of the concrete, and ε is the porosity of the concrete (chosen here to be S=0.7 and ε=0.2), yielding $D_{CO_2} = 3.2 \cdot 10^{-9} m^2/s$ as a result.

$$D_{CO_2} = 8 \cdot 10^{-7} \cdot \varepsilon^{\frac{4}{3}} \cdot (1-S)^{\frac{10}{3}} \cdot \left(\frac{T}{T_{ref}}\right)^{0.934} \cdot \left(\frac{P}{P_{ref}}\right)^{3.11} \tag{4}$$

Using all of these parameters as an input, the data shown in figure 9 is retrieved. As shown, the final length of carbonation is x_{CO_2}=2.7 mm after 10 years, giving a similar estimation as the one obtained with the former method, showcasing how corrosion due to carbonation was not found to be a significant issue. Therefore, carbonation-induced corrosion was not considered a significant concern during the operational period, as not even the rebar (35 mm from outer surface) was reached during the pre-backfill time where still the disposal package would be exposed to air.

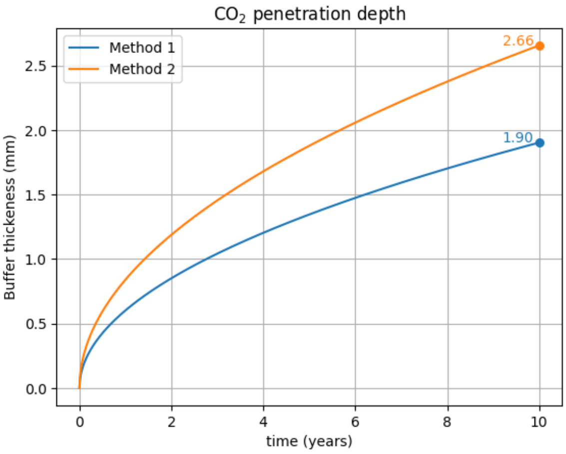

Figure 9: Penetration profile of CO_2 before backfilling (see python code in listing H1).

However, after 10 years the whole disposal tunnel is backfilled, meaning no significant source of CO_2 will be present after this time. Therefore, further corrosion due to carbonation can be neglected. The calculations made here are only estimates with the assumption that diffusion coefficients are constant over time and treat carbonation independently of leaching. Leaching increases porosity, thus accelerating ingress, by removing the calcium that sustains the alkalinity of the material[35]. The overall effects of carbonation still remain difficult to quantify.

4.1.2 Chloride-induced corrosion

Another mechanism to consider is the presence of chloride ions in the surrounding host rock, namely in Palaeogene clay, as pore water trapped in this layer has been found to present relevant quantities of the mentioned species (134.3-2270 mmol/kg), with a strong dependence on the salinity of the aqueous solution[5, 51]. Over long time scales, the diffusion of ions may lead to the deterioration of the cementitious material due to the corrosion of the reinforcements.

This second mechanism differs from carbonation, as no pH change is involved. Instead, a breakdown of the protective film surrounding the steel components is undergone, with reactions R10 and R11 providing an overview of the chemical transformations that take place during this step[36]. The principal mode of chloride ion transport was considered to be by diffusion due to a concentration gradient. However, a more complete description should also account for pressure-induced flow, electromigration or wick action to obtain a more reliable estimation[52, 53]. The overall diffusion is influenced by factors such as chloride binding capacity[54], porosity[53], composition, and external conditions[55].

Once steel is exposed and chloride accumulation occurs locally, leading to pitting corrosion above a threshold of 0.2 wt% of Cl^- by weight of cement when O_2 and H_2O are available, and 1 wt% when not[56]. During this process, cavities are formed in the material due to the detachment of iron ions which will decrease the load-bearing capacity of the material and promote further cracking[57], as well as releasing hydrogen gas, potentially causing pressure build-up and increasing loads on the surrounding materials. Description of these phenomena is highly challenging, because the pits are small and localized, which means they are difficult to characterise and an extensive preliminary analysis needs to be performed to ensure that pitting is not an issue[36].

$$\mathrm{Fe^{2+} + 2\,Cl^- + 4\,H_2O \rightarrow FeCl_2 \cdot 4\,H_2O} \tag{R10}$$

$$\mathrm{FeCl_2 \cdot 4\,H_2O \rightarrow Fe(OH)_2 + 2\,Cl^- + 2\,H^+ + 2\,H_2O} \tag{R11}$$

To evaluate the corrosion due to Cl^- ions, the penetration depth was first calculated by applying Fick's second law assuming a semi infinite medium along which an unreactive species diffuses under non-steady state conditions (see equation 5)[52, 58]. The boundary conditions used to write this expression are:

$$C_s = 0 \;\text{ at }\; t = 0,\; 0 < x < \infty; \quad C_x = C_s \text{ at } x = 0,\; 0 < t < \infty$$

The diffusion coefficient (D_{Cl}) is, here, assumed to be constant during the studied period. A more precise estimate would require empirical measurements under analogous conditions, allowing for the prediction of the effect of water to cement ratio, aggregate size, and overall concrete quality, among other factors which affect the diffusion of chloride ions[52].

Due to the different properties of the backfill and buffer materials, specific diffusion coefficients were used for each layer, namely $D_{Cl}=1 \cdot 10^{-9} m^2/s$[59] and $D_{Cl}=1 \cdot 10^{-11} m^2/s$[43], respectively. Therefore, the mentioned equation was used to plot an analogous variable to the concentration of Cl^- (C_x) as a function of the penetration depth (x_{Cl}), surface concentration (C_s), diffusion coefficient (D_{Cl}) and time (t) as depicted in figure 10.

$$C_x = C_s \left[1 - \mathrm{erf}\left(\frac{x_{Cl}}{2\sqrt{D_{Cl} \cdot t}}\right)\right] \tag{5}$$

This type of corrosion would only take place once the backfilling of the tunnels has taken place, as the main source of Cl^- is the saline pore water of the clay host rock[5]. To calculate the corrosion due to the amount of chlorides inside the disposal container, first the amount of pore water and Cl^- in the clay had to be computed as shown in equation B3, which was done using literature data, yielding a value of 3.67 kg_{Cl}/m^3[5, 60].

Once this is calculated, to ensure that there is no corrosion, all concentration values of Cl^- have to be divided by the amount of cement used in the concrete (240 kg/m^3 for magnetite concrete and 400 kg/m^3 for foamed concrete), obtaining the weight percent to evaluate whether there is pitting inside the concrete.

As depicted in figure 10, the diffusion of Cl^- ions was plotted at the rebar and overpack depth, as well as along the thickness of the entire tunnel using three scenarios with different salinities[5]. Due to the lack of available data with regard to the tunnel liner, it was modelled assuming that these supports were not present and their space was filled with foamed concrete. Hence, results obtained should be considered as a conservative approximation, as the liner theoretically exhibits a lower permeability, which would reduce migration.

It was observed how maximum values in the first critical depth were approximately 0.03, 0.10 and 0.42 wt%, respectively after 1200 years, while the second only reached 0.003, 0.013 or 0.052 wt%. An additional assessment was performed over the entire system at t=1200 years, where presence of Cl^- ions was expected to be the highest. In this scenario, wt% values were found to be below the 1 wt% threshold at depths of 1.535 and 2.255 m.

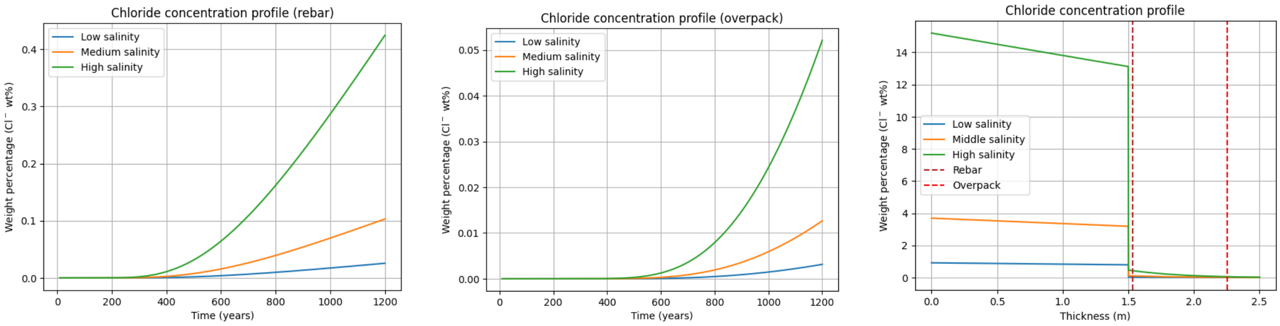

Figure 10: Chloride ions diffusion profiles at the rebar (A) and overpack (B) depths over time and along the tunnel width after 1200 years (C) (see python codes in listings H2 and H3).

As a result, the assessment of chloride diffusion yielded that in the studied time no significant concentration of these ions would be present near any metallic materials of the design choice made, allowing this phenomena to be disregarded as a design restriction. Nonetheless, presence of highly saline environments around the disposal facility could have a negative impact on the design, especially if optimization to reduce the disposal package diameter was conducted. In addition, Fick's law calculation assumes a constant chloride diffusion coefficient, but in reality, this coefficient increases as chemical degradation opens the pore network (due to carbonation and mechanical loading) with longer timescales[35].

4.1.3 Passive state corrosion, water ingress and limitations

Under fully anoxic alkaline conditions, dissolved iron corrosion products may be incorporated into cementitious minerals, preventing corrosion products build up upon the rebar, and thus making iron dissolution the rate determining step of the corrosion process[42]. Furthermore, corrosion rates decrease as concrete becomes less saturated with water, hence access to water is a primary controlling factor[61]. The cementitious environment also has a very low permeability, which means that the diffusion coefficients within it are generally low, and water ingress is limited. Therefore, corrosion can only consume the water initially present in the capillary pore system, or the small amount still entering through diffusion. In addition, as local humidity decreases, corrosion rates decline further, making constantly high rates more unlikely[61]. Considering these phenomena and in combination with the results obtained previously when assessing major corrosion mechanisms, it was concluded that corrosion is not expected to be a significant limiting factor in design selection.

However, under anoxic conditions, the kinetics of iron uptake by cementitious minerals, as well as the impact of this iron incorporation on concrete strength, are currently unknown. The rate at which a protective passive film develops under anoxic conditions cannot be quantified. Furthermore, the effect of this iron incorporation on concrete mechanical strength is also uncharacterised. Quantification of anoxic corrosion rates in dense concrete is not yet available, due to the difficulty to measure hydrogen production. A study by Kaneko et. al, tried to measure hydrogen evolution from carbon steel in concrete for 500 days and detected no hydrogen during that observation time. This means that hydrogen generated by corrosion migrates too slowly through the dense concrete pore structure to be detected at the external surface[62, 63].

Although steel corrodes at a very low rate ($< 1\ \mu$m/year), corrosion products can accumulate during long time spans and become sufficiently thick and rigid to exert significant expansive stresses on the surrounding concrete. Passive state oxide layers can reach thicknesses of up to 0.5 mm within 500 years, and the progressive transformation of corrosion products may increase stiffness to values around 30 GPa. The combination of volumetric expansion and increased rigidity can generate non-negligible expansive stresses on surrounding concrete which would affect long term integrity[35]. Moreover, if there is loss of material due to corrosion, it can weaken the overall structure to external loads and create an easier access for water to the vHLW inside the canister. These conditions are even more important in the reinforced concrete concept, where the canister lacks the overpack that mitigates these effects.

Additionally, other minor modes of steel degradation, such as sulphite diffusion, are not explored here, and in combination with carbonation and chloride induced corrosion, they could have a significant impact. Indeed, as seen in B2, in Appendix B1, iron incorporated into sulfate or chloride-bearing cementitious phases, creates secondary minerals with molar volumes up to 22 times that of metallic iron, hence such expansions could generate significant internal stress and cracking over geological timescales[42]. Despite the non-apparent corrosion issues, a greater number of experimental studies in the appropriate conditions, with in-depth analysis of multiple mechanisms should be carried out and modelled (diffusion coefficients, pH, initial concentrations, material's properties, among others), in order to have a more definitive certainty on the matter. For safety reasons, and given the effectively irreversible nature of geological disposal, the use of rebar inside the high-level waste disposal package was deemed to lack a sufficient level of confidence. Moreover, to be in line with the project requirement to apply only demonstrated technologies, reinforcement cannot responsibly be justified on theoretical premises alone. The carbon steel overpack is therefore retained and reinforcement excluded from the disposal package. This decision could be revisited if long-duration anoxic corrosion rate and hydrogen generation measurements on rebar in magnetite concrete, over representative timescales and conditions, confirmed the durability and stability of the disposal package.

4.2 Thermo-mechanical calculations

One of the most important design aspects is the mechanical stability of the disposal package. The disposal package has to withstand several stresses that could lead to failure, among which the most important factors are the thermo-mechanical stress induced by the heat-generating nature of the waste and possible impact stresses which could occur during emplacement. Due to the complex nature of the interaction between the thermo-mechanical and impact-induced stresses, the problem is split into the separate stresses.

4.2.1 Thermally induced stress

The vHLW generates a significant amount of heat due to the decay of radionuclides contained in the glass matrix. The heat flux ranges from around 2000 W at the time of casting the vHLW into the canister down to 200 W around 130 years, as seen in figure 11.

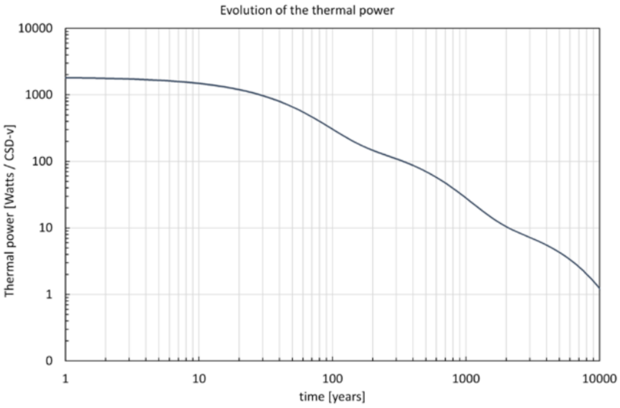

Figure 11: Thermal power of vHLW over time, adapted from COPERA CLAY 2024[5].

When the vHLW is placed into the buffer, the buffer will be heated until the cooling due to natural convection on the external surface will equal the thermal power of the vHLW. Both during the heating, and at steady state, the thermal stresses are an important factor in assessing the mechanical stability of the system. To get an accurate estimate for the thermo-mechanical stress in the buffer, the initial conditions have to be specified at first (see table 6). For the buffer, room temperature can be assumed, given that the vHLW will be placed into the buffer within a secured facility. For the vHLW itself, an initial calculation has to be performed, as the vHLW will be at an elevated temperature before placement into the buffer. For this calculation, a steady-state calculation was performed in which an equilibrium between the thermal power and natural convection on the outside of the overpack is reached. From these calculations, three temperatures are used, namely the mean temperature of the vHLW and the temperature of the canister and overpack.

Table 6: Initial conditions for steady-state thermo-mechanical stress simulations.

Component	**Initial temperature**	**Function**
vHLW	Determined by steady-state calculations	Heat source within model
Canister and Overpack	Determined by steady-state calculations	Conduct heat away from vHLW
Buffer	Room temperature (293.15 K)	Acts as insulator between vHLW and air
Flooring	Room temperature (293.15 K)	Heat sink by conduction located below the disposal package
Air	Room temperature (293.15 K)	Cooling source by natural convection

Since the disposal package consists of exclusively cylindrical geometries, a 2D axisymmetrical model was used, as this greatly reduces computational cost while maintaining a close resemblance to the physical problem at hand. For the model, it was chosen to simulate the vHLW in the overpack placed with its bottom on a concrete slab. A natural convection heat flux on the outer surfaces was applied to both the buffer and floor. Taking the storage time as a variable, the surface temperature both on top and on the side of the cylinder is plotted, as depicted in figure 12. Using this calculation, a minimum storage time of 49 years is found, being the thermal power 690 W at this storage time. This minimum time is based on the maximum allowable temperature of the buffer, which is set to be 90°C, as above this value the concrete will start drying out, which could lead to premature failure. For further analysis, a storage time of 50-130 years will be considered in time steps of 10 years.

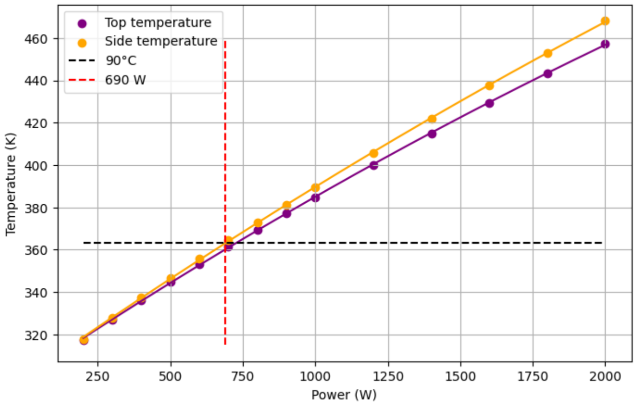

Figure 12: Maximum top and side temperature of the overpack for a specified thermal power.

After placing the vHLW canister and overpack in the buffer, the system cannot be considered under steady state conditions. The buffer acts as a large heat sink, and the temperatures of the overpack will initially drop before heating up again. After 360 h, the top and side of the overpack have reached within 3°C of the steady-state temperature. This was determined by transient calculation of the system using the initial conditions specified in table 6. The thermal and mechanical properties of concrete with magnetite aggregates have been researched in several studies, such as in the work of *Jaskulski et. al.* The most representative values presented are based on concrete with 60 vol% magnetite of the total mix volume[14]. In further research, it would be valuable to look into higher magnetite ratios, since these would have better shielding properties. The Young's modulus and Poisson ratio are not covered by the paper, so an estimation was made in accordance with EN 1992-1-1[64]:

$$E_{cm} = 22\left(\frac{f_{cm}}{10}\right)^{0.3} \qquad f_{cm} = f_{ck} + 8[\text{MPa}] \tag{6}$$

Where E_{cm} is the modulus of elasticity, f_{cm} is the mean compressive strength in MPa, and f_{ck} is the characteristic compressive strength. It must be noted that these are the values for a cylinder, while in the work of *Jaskulski et. al*, the compressive strength of a cube is measured. Table 3.1 from EN 1992-1-1 covers a conversion from cubic to cylindrical. This gives a value for f_{cm} of 41 MPa (cubic compressive strength). Filling in the relevant values yields an elastic modulus of 35.4 GPa. The Poisson ratio is taken as 0.2, and the linear coefficient of thermal expansion is taken as $10{\cdot}10^{-6}$, both based on EN 1992-1-1[64].

The temperature of the top of the overpack was determined using a time-dependent study over the span of 480 hours. This was done for storage times ranging from 50-130 years and yielded the results shown in figure 13. This shows that the buffer acts as a heat sink, as the temperature sharply drops after inserting the vHLW. This initial drop is caused by the fact that the buffer is initially at room temperature, while the vHLW is at elevated temperatures. After roughly 16 hours, the surface temperature reaches a minimum. Past this point, the temperature starts to increase again. The temperature at the top of the overpack is critical for the casting and curing process for the concrete used to seal in the waste. Therefore, it is recommended to start casting around 16 h after placing the vHLW canister, this gives more than 3 days of curing time at reasonable temperatures ($<$ 40°C) for the storage times of 80 years and longer.

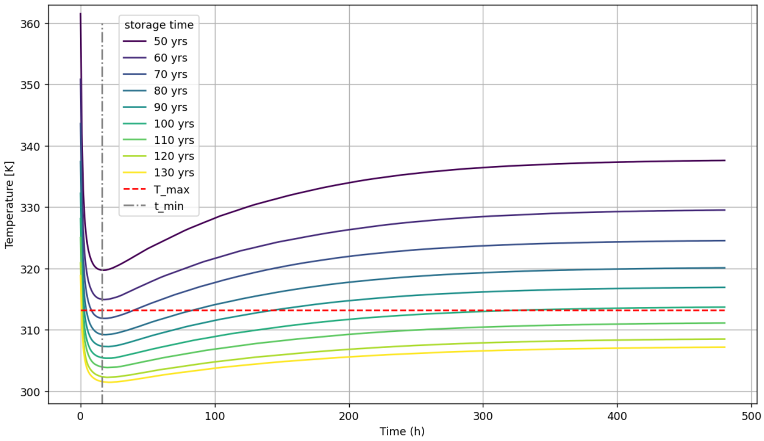

Figure 13: Temperature of the top of the overpack after placing the canister into the buffer for different storage times. Tmax indicates the maximal allowable temperature for casting and tmin is the storage time at which the overpack temperature reaches a minimum.

To determine the final thermal profiles and, with that, the thermo-mechanical stresses, a set of initial conditions has to be chosen again. For the overpack and canister temperature, the temperature at the top of the overpack at 16 hours from the previous study was selected (see figure 13). For the vHLW, the mean temperature of the vHLW at the same time point was used. The maximum temperature and maximum first principal stress ($\sigma_{1,max}$) were determined for the different storage times, these values have been summarised in table 6. The thermo-mechanical stresses for a storage time of 130 years are shown in figure 14.

The maximum first principal stress is an indicator for the tensile forces on the concrete. When this value exceeds the tensile strength of the concrete, it is likely that cracks will form. The stresses in the buffer are quite complex in nature. The thermal expansion of the steel is higher than that of the concrete[65], which creates a tensile force in the circumferential direction. However, the thermal gradient in the concrete counters this by limiting the expansion in the inner concrete layers, giving rise to an overall compressive stress tensor in the circumferential direction. When moving outwards in the buffer, the thermal expansion results in a tensile stress in the circumferential direction. This tensile stress is greatest at the outer surface of the buffer. The radial component of the stress tensor is only compressive. Since the temperature gradient is negative when moving away from the overpack, the thermal expansion of the concrete is smaller, further away from the overpack. This gives rise to the solely compressive forces. A visual representation of these forces is shown in figure 14.

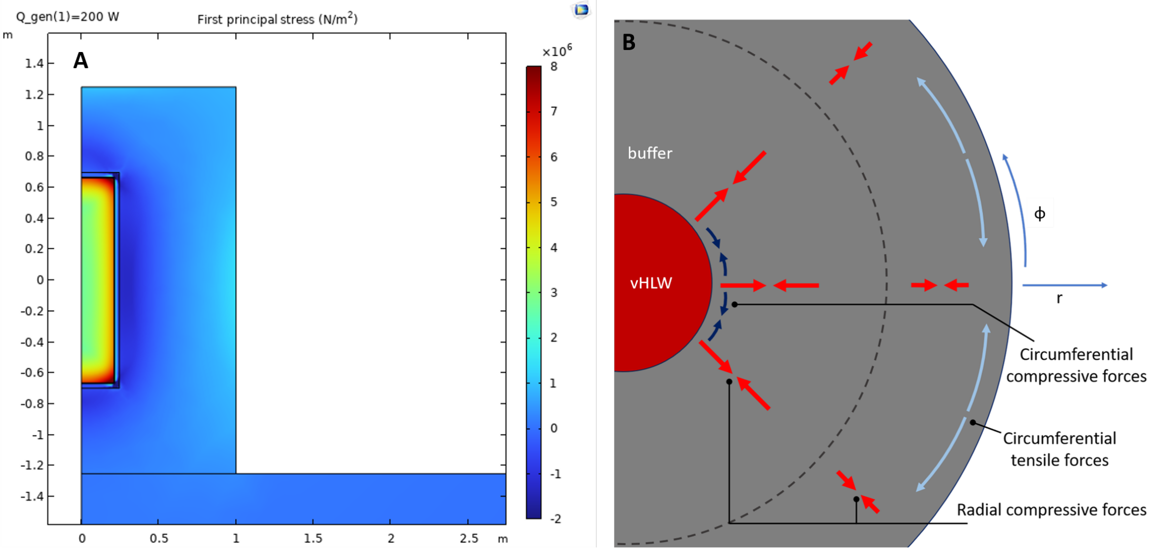

Figure 14: A) thermo-mechanical stress simulation for a storage time of 130 years (200 W), with buffer dimensions of 2 x 2.5 (h x d). B) stresses acting on the buffer due to thermal expansion.

For the magnetite concrete, no tensile strength is available from literature[14]. However, an estimate can be made using EN1992-1-1[64], which yields a mean tensile strength of 3.5 MPa. This means that the tensile stress caused by the thermal expansion exceeds the tensile strength of the concrete for storage times for 70 years or shorter (see table 7). These simulations were all performed using natural convection as heat dissipation, with an assumed outside temperature of 293.15 K. When placed in the tunnel, the temperature is likely higher due to geothermal heat. In this case, the temperature of the entire buffer will be slightly higher, which leads to a decrease in maximal tensile stress in the buffer. Therefore, the values calculated in the previous simulations are a worst-case scenario, and with higher external temperatures the tensile stresses will only decrease.

Table 7: COMSOL model temperature and stress results for vHLW in overpack and buffer with a buffer diameter of 2 m and a length of 2.5 m. For the $\sigma_{1,\max}$, the values marked in red are below the tensile strength of the concrete.

Storage time (years)		50	60	70	80	90	100	110	120	130
Thermal power (W)		680	550	470	400	350	300	260	220	200
vHLW in overpack	T_{top} (K)	359.34	348.53	341.77	335.78	331.47	327.13	323.63	320.11	318.34
	T_{side} (K)	362.23	350.74	343.56	337.22	332.66	328.06	324.36	320.65	318.80
	T_{vHLW} (K)	380	366	356	348	342	336	331	326	323
vHLW in buffer with open top	T_{top} (K)	319.71	314.95	311.86	309.22	307.30	305.43	303.93	302.33	301.53
vHLW sealed in buffer	$T_{\max}$ (K)	338.88	330.55	325.39	320.83	317.56	314.26	311.60	308.91	307.56
	$\sigma_{1,\max}$ (MPa)	5.52	4.46	3.81	3.24	2.84	2.43	2.11	1.78	1.62

Based on the thermo-mechanical modelling of the disposal package, it was found that the temperature of the overpack is an important factor when placing the vHLW into the buffer. At a storage time of less than 50 years, the temperature at the outer surface of the overpack would exceed the maximum allowable temperature of 90°C. From this point onwards, storage times of 50-130 years were evaluated. The temperature on top of the overpack has to be taken into consideration when casting the last part of concrete to seal in the vHLW. However, since the buffer acts as a heat sink, a time window of lower temperatures exists in which the casting is feasible. After sealing the buffer, the thermally induced tensile stress becomes the main issue. In steady state, the tensile stress was found to exceed the tensile strength of the concrete for storage times of 70 years and below. Above this temperature, the system does not exceed the tensile strength of the concrete, however, longer storage times might be needed to include a safety margin in the tensile strength.

4.2.2 Impact-induced stress

Apart from the thermally induced steady-state stress, stresses caused by impacts also play a role in the assessment of the structural stability of the system. These simulations proved difficult to set up and computationally extremely extensive. Therefore, only a limited number of simulations were performed. One possible impact that is of interest is a drop during emplacement. This was modelled as being a free-fall of a sideways cylinder impacting a hard surface from 20 cm. This was modelled as giving the disposal package an initial velocity and simulating the contact between it and the hard surface below. The influence of gravity was also included by imposing the gravitational force on the entire system. To determine the impact velocity, the following formula was used:

$$v = \sqrt{2gd_f} \tag{7}$$

Where v is the final velocity, g is the gravitational acceleration and d_f is the falling distance. This yields a final speed of 1.98 m/s. This was set as the initial condition for the disposal package. To simplify the simulation, the geometry of the disposal package was reduced to the buffer with a solid steel core with the dimensions of the overpack. Since there is no thin canister layer, the mesh sizes can be increased, which reduces the degrees of freedom that have to be solved during a simulation. Two simulations were performed on this setup, one for 0.003 s, with a time step of $1{\cdot}10^{-5}$ s. This simulation was performed to study the shock wave propagation through the buffer. Another study was performed over 0.02 s, with a step size of $1{\cdot}10^{-4}$ s. This study aims to investigate the stresses as the system settles from the impact.

For both simulations, initially a large compressive stress forms on the bottom of the buffer, this further propagates a pressure wave which travels through the buffer, reflecting on the top surface which causes a pressure spike in the centre and bottom of the buffer. After around 0.001 s, the system has stabilised from the initial shockwaves, with a non-homogeneous tensile stress field in the buffer. However, shortly after this stable period, a strong tensile force arises close to the contact patch, which far exceeds the tensile strength of the concrete (up to 80 MPa). This means that for a drop of 20 cm, the buffer would crack to such an extent that it would lose most of its containment function. Over the longer simulation, this stress concentration expands, which indicates further structural degradation of the contact surface. A frontal view of the stresses during different times is shown in figure 15.

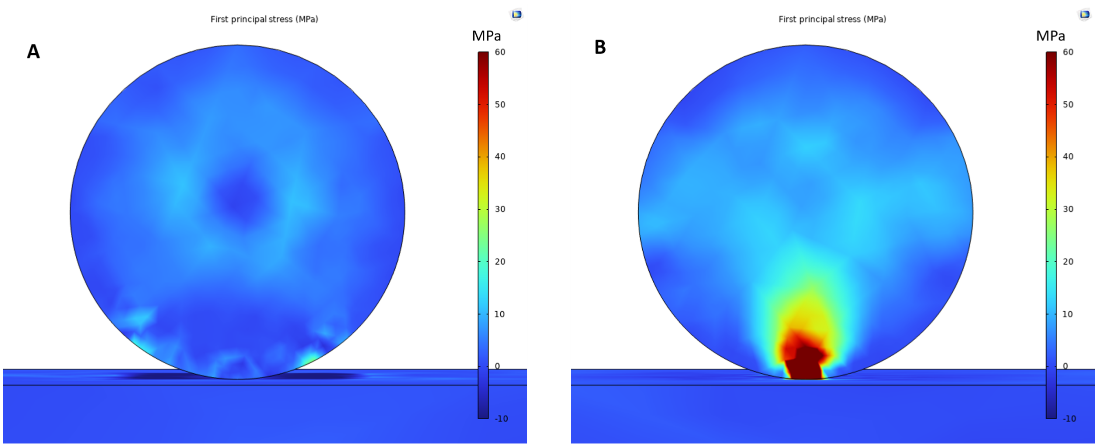

Figure 15: First principal stress present in the buffer after a drop of 20cm at 0.001 s (A) and 0.002 s (B).

A simulation with a length of 0.003 s and a time step of $1{\cdot}10^{-5}$ s was also performed for a drop of 2 cm, which would result in a speed of approximately 0.63 m/s at impact. This study shows similar results compared to the larger fall, albeit at lower stresses. After approximately 0.0015 s, the same large tensile stress forms around the contact patch, again exceeding the tensile strength of the concrete (up to 20 MPa). This means that even for a small drop, the buffer will likely fail. For more figures, see appendix B2.

Based on these impact-induced stress calculations, it was found that even for a small drop of 2 cm, the tensile stresses in the buffer exceed the tensile strength, which means that the buffer would lose its containment function. During emplacement, great effort should be taken in preventing the disposal package from being dropped.

4.3 Worker radiation exposure

The safety of workers with respect to the hazard posed by the ionizing radiation emitted by the vHLW, is a fundamental aspect to be evaluated in the design of waste disposal packages for underground disposal facilities. This aspect is partially explored in the HSE section of the report through a bow-tie diagram. Here instead, a quantitative estimation of exposure dose rates is carried out.

At its basis, radiation protection follows three tenets: maximize distance, maximize shielding, and minimize exposure time. The mechanism behind each is explored in table 8. In the context of worker protection in a vHLW geological disposal facility, shielding is offered by the disposal package, and time can be kept under control by monitoring shift lengths. Distance may be harder to increase due to the confined environment provided by the disposal tunnels.

Table 8: Principles of radioprotection and the mechanisms at their foundation.

Distance	**Shielding**	**Time**
Radiation flux from a point source decreases proportionally to distance squared due to three-dimensional geometric considerations.	By interposing matter between source and target, the interactions of radiation with this matter can be utilized to absorb or scatter parts of it.	Since radiation damage compounds with time, limiting the period of exposure can result in acceptable safety even in the presence of high active sources.

The presence of three design parameters with only one variable to optimize (radiation exposure), leads to an under-constrained problem, which therefore requires further assumptions. Since workers are expected to have to carry out some tasks in the disposal tunnels (e.g. emplacement, inspection), it is chosen to assess radiation exposure by selecting a fixed distance from the disposal packages and assessing the maximum acceptable exposure time as a function of cement buffer thickness and pre-emplacement storage time. This limit is expressed with respect to the maximum yearly allowable radiation exposure according to COVRA company policy: 6 mSv/year. The end result will therefore be an indication of the maximum amount of time per year for which a worker can be allowed to operate in a disposal tunnel. This time represents a necessary indication to evaluate the safety of working conditions within the disposal facility: too low a value will be sufficient reason to discard an otherwise viable design option.

A conservative approach is taken by utilizing the estimated activity properties of the vHLW at the time of insertion in the underground disposal facility, meaning the further decrease that will be observed in the subsequent 10 years before backfilling will not be accounted for.

A separate assessment is carried out for different types of ionizing radiation: beta particles, gamma photons, and neutrons. Recoil nuclei and alpha particles are immediately excluded as their penetration depth in matter can be neglected compared to the macroscopic scales of interest for this design.

The first step for this assessment is the determination of a radiation source term. To this end, the calculations carried out by *Aloy et al.*[66] will be used as foundation for all later estimates. All results will therefore depend on estimates carried out by the authors of the paper on reprocessed waste produced by Russian Vodo-Vodyanoi Enyergeticheskiy Reaktor ("water-water energetic reactor", VVER) type reactors. This is assumed to be an acceptable approximation, as VVERs operate in similar conditions to European Pressurized Water Reactors (PWR), and can therefore be expected to generate waste with similar radiological properties. In case of future deployment in the Netherlands of new reactors based on fourth generation technologies, a reassessment may be needed due to the possible alteration in waste composition.

4.3.1 Beta radiation

The major beta emitting nuclides in vHLW are ^{137}Cs and ^{90}Sr[66], both of which have half lives long enough to present non-negligible quantities even after above ground storage periods of ∼100 years (respectively 30.08 and 28.91 years[67]). Beta particle penetration depth in high-density materials is generally negligible. This can be shown using Feather's rule, an empirical relation expressing penetration depth (in cm) as a function of maximum beta particle energy (in MeV) and material density (in g/cm^3):

$$d = \frac{0.543E_{\beta,max} - 0.160}{\rho} \tag{8}$$

Considering a density of stainless steel of 7.7 g/cm^3, the estimated penetration depth is of ∼0.3 mm, and is therefore confirmed to be irrelevant for radiation exposure estimates.

Bremsstrahlung originated X-rays are then assessed. The energy emitted in the form of photons through this process can be estimated with the following empirical equation[68]:

$$E_X = \frac{E_{\beta,max}^2 Z}{3000} \tag{9}$$

where $E_{\beta,max}$ is the maximum energy of the beta decay spectrum and Z is the atomic number of the shielding material. Considering iron shielding, and a maximum possible beta energy of 1.176 MeV for beta decay of ^{137}Cs directly to the ground state of ^{137}Ba, yields an X-ray energy of 12 keV. Using the XCOM tool[69] provided by the National Institute of Standards and Technology, this energy is found to correspond to a mass attenuation coefficient of $\sim$120 cm^2/g, leading to a linear attenuation coefficient of $\sim$924 cm^{-1} and a half shielding thickness of 7.5 μm. All Bremsstrahlung can therefore be considered as stopped by the stainless steel canister alone.

4.3.2 Gamma radiation

The gamma emission spectrum of the vHLW presents a peak just under the 1 MeV energy range at short times after vitrification[66]. From this observation, ^{137}Cs is identified as being the most likely source of the vast majority of the observed gamma radiation[2]. This assessment is further validated by looking at the intensities of this peak[66] at 0, 50 and 500 years, and observing its decrease in intensity with time roughly fits with the 30.08[67] year half-life of ^{137}Cs.

It is from now on assumed that the gamma radiation emitted from the waste can be considered as purely generated by this radionuclide, and is therefore monochromatic (0.662 MeV) and decreases following the aforementioned half life. This assumption is considered valid because all other energy ranges are one or more orders of magnitude lower in volumetric specific activity[66]. For the higher energy ranges, which will have lower attenuation coefficients through the shielding layers, volumetric specific activity starts at two orders of magnitude under that of the ^{137}Cs peak, and drops rapidly with increasing energy[66].

Using an energy of $\sim$0.7 MeV, XCOM[69] is once more used to obtain mass attenuation coefficients for the material compositions indicated in appendix table B1. The results are collected in table 9. In the same table, the linear attenuation coefficients, obtained by multiplying the mass attenuation coefficients by the densities of the respective materials, are also listed.

Table 9: Mass attenuation coefficients (μ) and linear attenuation coefficients (μ^*) for all components of the waste package.

	vHLW	**Stainless steel**	**Carbon steel**	**Magnetite concrete**
$\boldsymbol{\mu}$ (cm^2/g)	$7.5\cdot10^{-2}$	$7.2\cdot10^{-2}$	$7.2\cdot10^{-2}$	$7.4\cdot10^{-2}$
$\boldsymbol{\mu}^*$ (cm^{-1})	0.207	0.554	0.562	0.274

Given these parameters and assumptions, the problem becomes largely one of geometric assessment: only part of the ionizing radiation emitted by the waste will be headed toward the target (worker), and as these rays move along their path, each one will be attenuated differently depending on what layers it passes through. Both tasks are carried out by creating a dedicated script based on a ray-tracing algorithm.

The first component of this assessment, the determination of the fraction of gamma rays directly hitting the target, is obtained by first subdividing the waste into finite volumes, for each of which the emission geometry will be evaluated individually. Likewise, the target, modelled here as a rectangle rotating along its vertical axis to always be facing toward the assessed source point in the waste, is subdivided in a grid of finite areas. Figure 16 offers a graphical representation of these steps. Each of these areas will occupy a solid angle fraction $d\Omega$ which can be expressed as

$$d\Omega = \frac{dA}{R^2}\cos\theta = dA\frac{D}{R^3} \tag{10}$$

where θ is the angle between the normal vector of dA and the vector pointing from dA to the source point, D is the distance from the source point to the central point in the target belonging to the same horizontal plane, and R is the distance between the source point and the evaluated point in the target. Since $d\Omega/4\pi$ expresses the fraction of solid angle occupied by the finite portion dA of the worker, each of these values corresponds to the fraction of direct radiation emitted from one point, hitting that region of the target.

---

[2] More accurately, the gamma emissions come from the decay of its short-lived daughter, ^{137m}Ba, down to its ground state

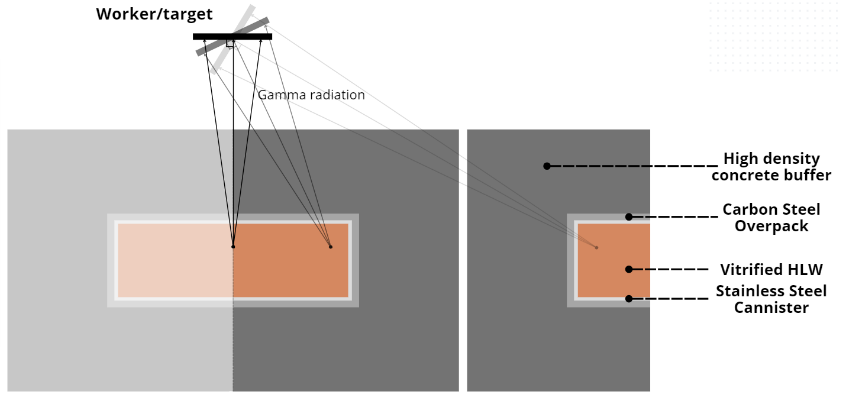

Figure 16: Visual representation of a 2D section of the system studied by numerical approximation to assess radiation exposure of a worker inside a vHLW disposal tunnel.

Subsequently, attenuation is assessed. To this end, a second function is called, which takes the ray-directions that have been found previously to be hitting the target, and starting from the source point, proceeds along these attenuating each ray depending on what material the step was carried out through. The attenuation over each step dl is calculated according to the Lambert-Beer law:

$$I_i = I_{i-1} e^{-\mu dl} \tag{11}$$

where I_i is the ray intensity after a thickness dl of shielding, and I_{i-1} is the intensity at the previous point. These steps are continued until either all the rays have exited the disposal package, therefore assuming the shielding effect of air to be negligible, or when the ones still proceeding through it have reached a sufficient attenuation ($\sim 10^{-18}$). Additionally, it is considered that a 2 meter long path, even if occurring entirely through the material with the lowest μ^* (vHLW), would bring the intensity of the beam down to undetectable levels ($\sim 10^{-18} \cdot I_0$). This observation is used for the estimation of a maximum length of waste disposal packages that will contribute any significant influence to the radiation dose of the worker: beyond this distance, evaluation becomes superfluous and is therefore avoided.

Multiplying each $d\Omega_j/4\pi$ by the corresponding attenuation fraction $e^{-dl\sum_i \mu_{ij}}$ and then adding all these elements, yields the total intensity attenuation fraction induced by the shielding layers as formulated in equation 12:

$$F_{hit} = \frac{1}{4\pi} \sum_j d\Omega_j e^{-dl\sum_i \mu_{ij}} \tag{12}$$

These values are then averaged over all source points in the waste form. Finally, a build up factor is introduced to take into account the broad beam geometry of the model. This value depends on the number of mean free paths covered by the radiation in the material, where $\lambda_{mfp} = \frac{1}{\mu^*}$. Since most of the radiation intensity will come from the least attenuated rays, meaning the ones travelling radially through the disposal package, the total distance chosen is equal to the radius of the container: 1 meter. This value could be updated when different package thicknesses are assessed, but the change in build up (roughly linear) will have a minor effect compared to that of shielding (exponential). The μ^* used is an average of those of each material, weighted over the respective thickness, and is equal to 0.271 cm^{-1}.

The end result is 27.1 mean free paths, which, for concrete, is found in literature[70] to correspond to a build up factor of roughly 120 for a gamma rays around 1MeV[3]. From the same paper, it is observed that build up for iron is not exceedingly different from that of concrete, indicating the aforementioned value should be applicable to magnetite concrete as well

The amount of energy deposited in the human target is calculated using a mass energy absorption coefficient for human tissue of 0.032 cm^2/g[68], a human tissue density of 0.985 g/cm^3, assuming a thickness of 20 cm, and applying once more a Lambert-Beer type exponential expression. Finally, after adequately converting energies from eV to Joules, the dose rate in Gy/s for a worker in a tunnel is calculated as:

---

[3] Here a value slightly higher than that identified from the paper is chosen since the energy of the gamma ray is slightly lower than 1MeV and build up increases at lower energies[71]

$$D_{rate} = A(t_{storage}) \cdot F_{hit} \cdot E_{dep} \cdot \frac{1}{m_{worker}} \tag{13}$$

Where $A(t_{storage})$ is the total gamma activity as a function of above ground storage time, F_{hit} is the fraction of emitted photons that are both aimed at the target and that don't get shielded by the disposal package, E_{dep} is the energy deposited by each gamma photon in the worker's body, and m_{worker} is the mass of the worker. Since gamma rays have a radiation weighting factor of 1, D_{rate} in Gy/s is equal to D_{rate} in Sv/s. Using the parameters listed in table 10, the results shown in table 11 are obtained.

Table 10: Properties for the estimation of radiation dose rates in underground disposal facility.

Initial[4] γ specific activity	$1{\cdot}10^{11}$ cm^{-3}s^{-1}[66]
Half life	30.08 years[67]
Height of disposal package	2.5 m
Height of waste form	1.325 m
Diameter of waste form	0.41 m
Canister thickness	0.01 m
Buffer thickness	0.03 m
Gap between disposal packages	0.04 m
Floor divot depth	0.4 m
Worker height	1.83 m
Worker width	0.5 m
Worker weight	85 kg
Worker thickness	0.2 m
Distance from centre of vHLW	1.5 m
vHLW volume mesh points	23, 23, 105 (x, y, z)
Worker surface mesh points	161, 55 (h, w)
Ray-step length (dl)	0.001 m

The estimated allowable working times, highlight the strong impact of shielding over dose rates. Indeed this dependence is expected to be exponential (see equation 11). Disposal package radii of 0.7 or 0.8 m, are shown here to be inadequate for proper gamma radiation shielding and are therefore discarded as potential design options. Additionally, for radii of 1 and 1.1 m, the radiation dose rate becomes either comparable to background radiation or effectively negligible.

To add a point of comparison, the same calculations were ran assuming a buffer made with regular concrete ($\rho \simeq 2.4$g/cm^3 and $\mu \simeq 7.3 \cdot 10^{-2}$ cm^2/g) instead of high-density magnetite concrete. For a disposal package radius of 1.1 m and a pre-emplacement storage time of 130 years, this resulted in dose rates closest to those obtained with magnetite concrete at a 0.8 m radius and 100 years of storage time ($\sim 3.9 \cdot 10^2$ h of maximum yearly exposure time). This indicates that the inclusion of magnetite aggregates in the concrete shielding has a major positive impact on its gamma-radiation shielding effectiveness.

It is also noted that discretization parameters like mesh sizes and ray-step length can significantly affect the final results, if the values chosen are too coarse. For this reason, a sensitivity analysis was carried out for such variables. Despite this effort, the high computational load of the tasks made it necessary to choose a compromise: it is estimated that each parameter may carry with it an error of roughly ~1%, meaning in the worst case scenario a total compounding error of ~6% could be present. It is therefore highly recommended to run the same calculations with a finer discretization if sufficient computational power is available.

4.3.3 Neutron radiation

The neutron flux emitted from the waste mostly originates from two processes: spontaneous fission and (α,n) reactions. The former, being dependent on minoritarian decay branches of minor actinides (^{244}Cm, ^{246}Cm), represents a lesser portion of the neutron flux observed in vHLW. The process of neutron shielding is more complex than that of gamma radiation. For this reason, a preliminary estimate is made to assess the potential radiation impact of neutrons before attempting an exact calculation.

This assessment is carried out by taking the specific neutron activity after 50 years of decay, provided by *Aloy et al.*[66], estimated to be $5{\cdot}10^4$ cm^{-3}s^{-1} considering the ~$5{\cdot}10^3$ cm^{-3}s^{-1} activity due to spontaneous fission alone, and increasing for safety margin to consider the comparatively much higher activity caused by (α, n) reactions

---

[4] At time of vitrification

as highlighted in the same paper. This is then multiplied by the waste volume of 0.18m^3 to obtain the total activity of one waste container, and then scaled by a factor described by equation 11, where dl is replaced by the macroscopic shielding thickness Δl. Here the linear attenuation coefficient used is that of iron, since this is the major component of all external shielding layers: $\mu = 1.19\ \text{cm}^{-1}$. This value is then divided by 10 to approximately reflect the length scale required to thermalize the neutrons prior to absorption. A characteristic length of 1 meter for attenuation is also assumed. Finally, the ∼3MeV[66, 72] average energy of the emitted neutrons is assumed to be fully deposited in the human tissue, and the percentage of radiation emitted from the waste aimed at the target is found by numerical assessment to be roughly 2.8%. Considering a human mass of 85 kg, a dose rate of 35 nGy/h is found, which corresponds roughly to 0.7 μSv/h considering the maximum dose weighting factor for neutrons of 20. The final result is several orders of magnitude lower than the one found for gamma radiation, suggesting this can be neglected.

Another aspect worth noticing is that neutrons have a much smaller rate of emission from the waste, and the potential significance of their effective dose rate can only arise from a lower effectiveness of the shielding compared to that of gamma rays. Therefore, consequences of neutron emission will become less relevant in the case of accident scenarios, where highly dangerous dose rates are caused by a decrease in shielding effectiveness due to cracking of the buffer. It is recognized though that a very strong and influential assumption has been made in the description of the attenuation process. To obtain a more confident result a numerical assessment would be needed.

One possibility is to simplify the problem into two key steps: thermalization and subsequent capture. This is due to the much lower capture cross-sections presented by fast neutrons compared to thermal ones. Therefore in estimations on neutron shielding it is often assumed that only thermal neutrons are absorbed. To apply this approach the following procedure could be executed:

- An average neutron scattering cross section for the material of interest is calculated at thermal energy range. It is assumed that scattering cross sections do not change going from ∼0.025eV to the most common emission energy of ∼3MeV[66, 72]. This leads to some imprecision, as scattering cross sections tend to decrease with neutron energies increasing over 1MeV.
- The fraction of energy lost per collision is calculated as $\varepsilon = \frac{6}{3A_{mix}+1}$[73], where A_{mix} is taken as the weighted average value of the atomic numbers of elements in the assessed material.
- The number of collisions required for thermalization of a neutron is expressed as $\bar{c} = \frac{\ln(E/k_bT)}{\varepsilon}$.
- An average "moderation length" L_m is estimated as $\lambda_{mfp} \cdot \bar{c} = \frac{\bar{c}}{\sigma_s N}$, where N is the number of atoms per unit volume).
- All values are computed for the different materials present in the waste form and disposal package and averaged.
- Shielding is calculated using thermal neutron absorption cross sections, but only once the path length covered by the neutron is greater than the estimated L_m.

For the steps described above, the cross sections provided by *Ashby et al.*[73] would be used. The resulting assessment, while still of a very approximate nature, could be considered able to provide a better estimation of neutron shielding efficacy.

4.4 Storage time optimisation

Another design goal was to optimise the storage time versus the disposal package dimensions. It was found that thermo-mechanical stresses in the buffer play a big role determining the storage time, so much so that the storage time must be at least 70 years given a diameter of 2 m and a length of 2.5 m. However, the radiation dose also plays a big role in determining allowable buffer diameters.

For the optimisation, it was chosen to take a storage time ranging from 50 years up to 130 years in steps of 10 years, and buffer radii of 1.1, 1.0, 0.9, 0.8 and 0.7 m. For each of these, a calculation was performed to check for the thermo-mechanical stress. The ones for which this stress is below 80% of the tensile strength were deemed acceptable, in accordance with the prevention barriers indicated in the bowtie shown in figure 26. A further selection can then be made on the basis of radiation shielding: the number of maximum allowable working hours in the disposal facility shall not be under 2000, roughly equivalent to the number of total yearly working hours. This assessment was only carried out for container sizes that did not already fail in the thermo-mechanical stress category. All of this has been documented in table 11.

Table 11: Principal stress and maximum allowable exposure hours for a dose of 6 mSv as a function of storage time, and buffer radius. In red the parameters outside the acceptable limits, in orange those within an 80% margin (only for tensile stresses). In white the combinations with fully acceptable properties.

Storage Time (years)	**Thermal Power** (W)	**Quantity**	**Radius** (m)				
			$r = 1.1$	$r = 1.0$	$r = 0.9$	$r = 0.8$	$r = 0.7$
130	200	σ_p (MPa)	1.38	1.47	1.54	1.55	1.52
		Max working hours	$3.5 \cdot 10^6$	$2.2 \cdot 10^5$	$1.4 \cdot 10^4$	$8.5 \cdot 10^2$	54
120	220	σ_p (MPa)	1.53	1.63	1.71	1.71	1.69
		Max working hours	$2.8 \cdot 10^6$	$1.8 \cdot 10^5$	$1.1 \cdot 10^4$	$6.7 \cdot 10^2$	43
110	260	σ_p (MPa)	1.83	1.95	2.04	2.05	2.01
		Max working hours	$2.2 \cdot 10^6$	$1.4 \cdot 10^5$	$8.6 \cdot 10^3$	$5.4 \cdot 10^2$	34
100	300	σ_p (MPa)	2.14	2.27	2.37	2.38	2.34
		Max working hours	$1.8 \cdot 10^6$	$1.1 \cdot 10^5$	$6.9 \cdot 10^3$	$4.3 \cdot 10^2$	27
90	350	σ_p (MPa)	2.52	2.67	2.80	2.80	2.75
		Max working hours	$1.4 \cdot 10^6$	$8.8 \cdot 10^4$	$5.4 \cdot 10^3$	$3.4 \cdot 10^2$	21
80	400	σ_p (MPa)	2.90	3.08	3.21	3.22	3.17
		Max working hours	$1.1 \cdot 10^6$	$7.0 \cdot 10^4$	$4.3 \cdot 10^3$	$2.7 \cdot 10^2$	17
70	470	σ_p (MPa)	3.44	3.64	3.80	3.81	3.75
		Max working hours	$8.8 \cdot 10^5$	$5.5 \cdot 10^4$	$3.4 \cdot 10^3$	$2.1 \cdot 10^2$	13
60	550	σ_p (MPa)	4.05	4.29	4.47	4.48	4.42
		Max working hours	$7.0 \cdot 10^5$	$4.4 \cdot 10^4$	$2.7 \cdot 10^3$	$1.7 \cdot 10^2$	11
50	680	σ_p (MPa)	5.06	5.35	5.57	5.59	5.51
		Max working hours	$5.6 \cdot 10^5$	$3.5 \cdot 10^4$	$2.2 \cdot 10^3$	$1.3 \cdot 10^2$	8.5

Based on thermo-mechanical calculations alone, storage times of 80 years and shorter can be discarded. These storage times give rise to a first principal stress on the buffer which is too high, being above 80% of the tensile stress of the concrete. For buffer radii of 0.8 and 0.7 m, the maximum allowable working hours are below 600 hours, which would equal 15 weeks of full-time work. This is deemed to be insufficient for employees, since a full-time employee of the disposal facility would not be able to work continuously through the year. This yields a buffer radius of 0.9 m, with a storage time of 90 years as optimum. As the tensile forces are significantly below the tensile strength, and the maximum working hours are more than that of a full-time employee in a year.

4.5 Evaluation of accident scenarios

In radiation safety, it is of great importance to assess not only the exposure rates at design conditions, but also to have a measure of how different potential unexpected scenarios may affect dose rates and consequent safety margins. To this end, three failure modes of the magnetite concrete shielding layer were studied (see figure 17):

- **Surface chip**: breaking off of a shallow but wide section of the buffer (7cm×7cm×2cm), considered as possible consequence of an impact with a piece of machinery or other heavy item.
- **Thin crack**: formation of a thin crack (2mm×10cm×30cm) along the length of the buffer as a consequence of thermally induced stresses. Direction and depth of the crack are chosen as representative of principal stress direction and radial profile found in the previously shown thermo-mechanical calculations.
- **Catastrophic failure**: loss of a major section of shielding (50cm×50cm×50cm). This case is included to highlight the severe consequences of such an extreme scenario. Calculations are therefore only carried out for the most conservative case, with a disposal package radius of 1.1 m.

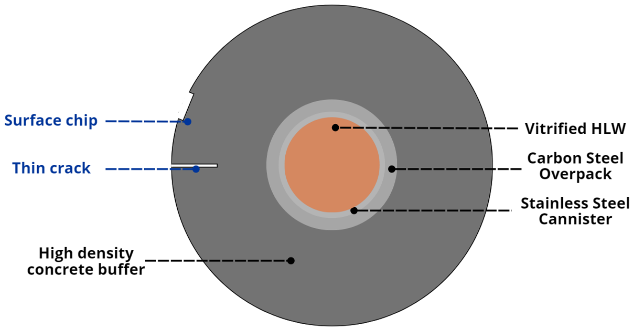

Figure 17: Visual representation of the first two accident scenarios assessed: surface chipping and deep thermally-induced cracking.

The estimations are completed using the same algorithm described above, with the introduction of logic conditions eliminating buffer attenuation in correspondence with the coordinates of the damaged section. For adequate assessment of the effects of a thin crack, a shorter step size of 0.5 mm was used to allow for proper resolution of the smaller geometric features. The results for the first two scenarios are summarised in table 12.

Table 12: Radiation dose estimations in the event of possible accidental events, for container sizes and storage times found to be applicable in normal conditions. Decreases compared to the table 11 are highlighted in yellow.

	Dimensions	**Storage time**	**Max working hours** (h)		
		(years)	($r = 1.1$ m)	($r = 1.0$ m)	($r = 0.9$ m)
Surface chip	height: 7 cm width: 7 cm depth: 2 cm	130	$3.5 \cdot 10^6$	$2.2 \cdot 10^5$	$1.4 \cdot 10^4$
		120	$2.8 \cdot 10^6$	$1.8 \cdot 10^5$	$1.1 \cdot 10^4$
		110	$2.2 \cdot 10^6$	$1.4 \cdot 10^5$	$8.6 \cdot 10^3$
		100	$1.8 \cdot 10^6$	$1.1 \cdot 10^5$	$6.8 \cdot 10^3$
		90	$1.4 \cdot 10^6$	$8.8 \cdot 10^4$	$5.4 \cdot 10^3$
Thin crack	height: 2 mm width: 10 cm depth: 30 cm	130	$3.5 \cdot 10^6$	$2.2 \cdot 10^5$	$1.4 \cdot 10^5$
		120	$2.8 \cdot 10^6$	$1.7 \cdot 10^5$	$1.1 \cdot 10^4$
		110	$2.2 \cdot 10^6$	$1.4 \cdot 10^5$	$8.5 \cdot 10^3$
		100	$1.7 \cdot 10^6$	$1.1 \cdot 10^5$	$6.8 \cdot 10^3$
		90	$1.4 \cdot 10^6$	$8.7 \cdot 10^4$	$5.4 \cdot 10^3$

The assessment of a surface chip leads to the conclusion that minor surface damage is effectively irrelevant to radiation exposure rates. The only minor difference, appearing in the case of 100 years of storage time and disposal package radius of 0.9 meters, is born out of the rounding of slightly different output values. Therefore the disposal packages as designed can be considered resilient to this form of surface damage.

The calculations in presence of the aforementioned thin crack, lead to slightly more visible results, but still mostly within the margin of error of the estimate. Indeed, all visible decreases appearing compared to the values in table 11, are once more a consequence of rounding. An overall trend indicating slightly higher dose rates, especially for lower disposal package diameters, can anyway be spotted. This indicates that while a small crack will not lead to severe safety consequences, if left unchecked and allowed to extend, it may result in dangerous exposure rates at a later time.

Finally, in case of the previously described catastrophic failure of the disposal package, the amount of time needed for a worker to receive a dose over 6 mSv ranges from 4 hours to just over 9, for a pre-backfilling storage time respectively of 90 and 130 years. This indicates that imperative emergency procedures might still be carried out in the tunnels while maintaining acceptable safety levels, especially if suitable personal shielding equipment is supplied to the workers. Despite this, it is evident that extreme time regimentation would be needed in such instances to ensure compliance with worker safety and company policy regarding radiation exposure.

5 Product manufacturing

This section is subdivided into two main parts. The manufacturing of concrete is outlined, including the production of cement. As well as the production and emplacement of the disposal package. This second part will also include the backfilling process.

5.1 Material production

In this section, the manufacturing of the concrete required for both the buffer and the backfilling process is covered. In addition, the design of a cement manufacturing plant, including a detailed Process Flow Diagram (PFD) and Piping and Instrumentation Diagram (P&ID), was investigated.

5.1.1 Cement manufacturing plant

As presented in the concept selection and opportunity assessment, concrete was found to be a crucial material for the construction of the buffer and the backfill. In spite of the difference in characteristics that each product required, both cases demanded a base of cement, which is further mixed with sand, water and additives in specific ratios to yield the final high- and low-density concretes. Although COVRA does not manufacture cement itself, cement-based materials were an important part of the proposed disposal system. For this reason, a general overview of the cement production process was included. Additionally, this overview allows for the cost analysis of a cement production plant to assess its practical viability.

5.1.1.1 Process block diagram

Firstly, the general procedure for the preparation of concrete is depicted in figure 18, where cement is previously prepared from clinker and gypsum. The process begins with the preparation of raw materials, which are crushed and mixed to obtain a homogeneous feed composition. The main components are limestone and clay, which provide most of the calcium, silica, alumina and iron required for clinker formation. Small amounts of corrective materials can be also added to adjust the final composition.

In the final concrete production stage, cement is mixed with water, sand and additional materials to obtain concrete with the required mechanical and chemical properties. Depending on the application, additives can be incorporated to improve durability, permeability and thermal resistance. In the context of this project, these properties are especially important because the concrete used in the disposal package must remain stable for very long periods of time under thermal, chemical and mechanical stress conditions. In addition, the selected materials should contribute to reducing water ingress and improving the overall containment performance of the disposal system.

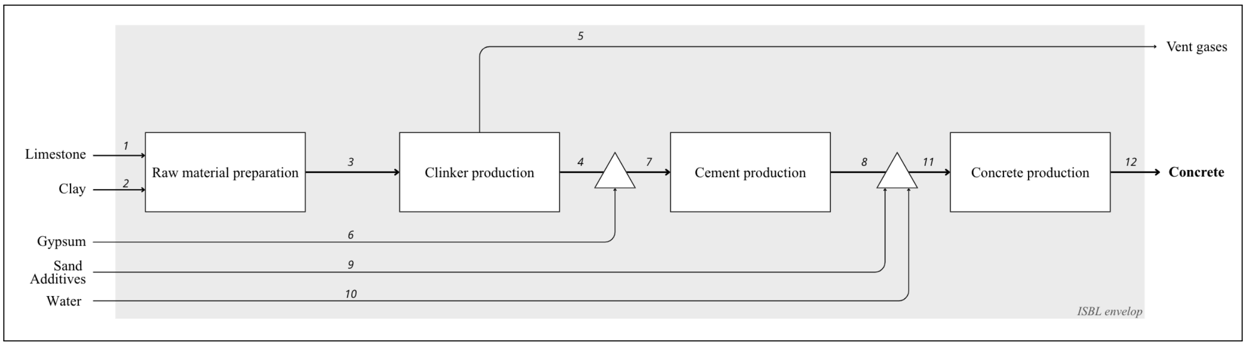

Figure 18: General block diagram for concrete manufacture.

Moreover, in table 13 the mass balance for the previously presented block diagram was listed. It is worth mentioning that in the concrete production block both high and low density composites were manufactured (see specific compositions in tables C1 and C4, respectively). For additional information on the transformations required for each material, figure 20 provides the different steps for each scenario.

Table 13: Stream table based on block diagram for high and low density concrete production. The incoming streams are marked with a light blue color, and the outgoing streams are marked with a dark blue color.

Components	Stream table (tonnes)											
	1	2	3	4	5	6	7	8	9	10	11	12
Limestone	130765	0	130765	0	0	0	0	0	0	0	0	0
Shale	0	13685	13685	0	0	0	0	0	0	0	0	0
Sand	0	6082	6082	0	0	0	0	0	0	0	0	0
Iron ore	0	1522	1522	0	0	0	0	0	0	0	0	0
Gypsum	0	0	0	0	0	5109	5109	0	0	0	0	0
Clinker	0	0	0	97062	0	0	97062	0	0	0	0	0
Cement	0	0	0	0	0	0	0	102170	0	0	102170	0
CO2	0	0	0	0	54992	0	0	0	0	0	0	0
Water	0	0	0	0	0	0	0	0	0	62283	62283	0
River Sand	0	0	0	0	0	0	0	0	132309	0	132309	0
Magnetite	0	0	0	0	0	0	0	0	168336	0	168336	0
Foam	0	0	0	0	0	0	0	0	6913	0	6913	0
Superplasticizer	0	0	0	0	0	0	0	0	64	0	64	0
High density concrete	0	0	0	0	0	0	0	0	0	0	0	227852
Low density concrete	0	0	0	0	0	0	0	0	0	0	0	244223
Total	**130765**	**21289**	**152053**	**97062**	**54992**	**5109**	**102170**	**102170**	**307622**	**62283**	**472075**	**472075**

Since it was chosen to develop a cement manufacturing plant, a second block diagram (see figure 19) was constructed to give an overview of the main tasks performed in the plant. The process in question mainly handles solids, which are crushed, milled and homogenised by a series of units (raw material preparation) before entering the pyrolysis process. The transformation of limestone and clay into clinker is achieved by heating the raw materials to high temperatures, producing CO_2 as the main side product. Preheating and calcination were highly relevant parts of the process, as they accounted for 20-30% $CaCO_3$ decomposition into the mentioned gas, preventing build-up in the following equipment. Gas and solids produced had to be cooled down and further milled with gypsum in the later case to yield the final cement product.

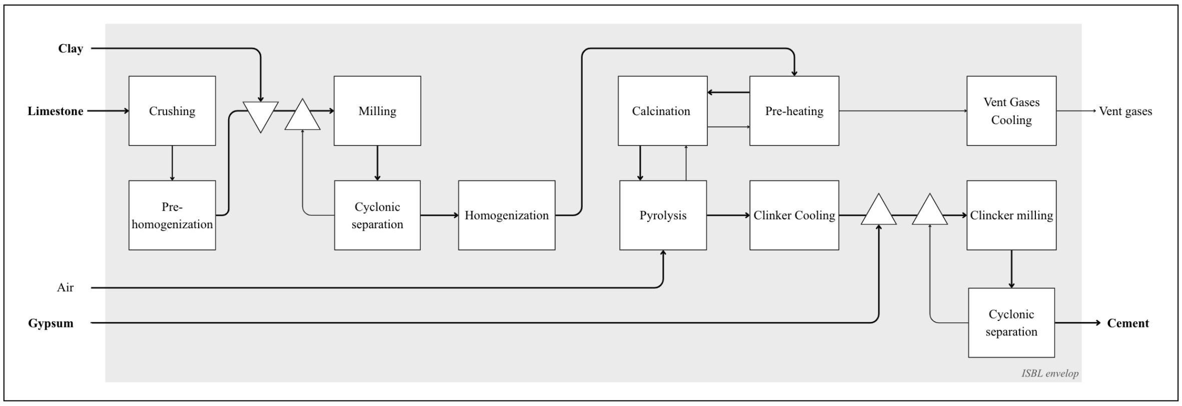

Figure 19: Block diagram for cement manufacture.

5.1.1.2 Process Flow Diagram

A Process Flow Diagram (PFD) was developed as shown in figure C1, where the principal inlet, outlet and process streams, as well as relevant equipment (all operating at atmospheric pressure) were depicted and labelled. As previously mentioned, the raw materials, namely limestone ($CaCO_3$, SiO_2), are crushed (*CR-101*) and pre-homogenized (*T-101*), further milled (*A-101*) with clay (Al_2O_3, Fe_2O_3, SiO_2) and finally homogenized and stored in a stacked silo (*T-102, T-103*) to maximum sizes ranging from 50 to 125 μm approximately, depending on the material[74]. It is relevant to highlight that several cyclones (*S-101/102/103*) are placed after milling stages to ensure a correct particle size, recycling otherwise the material that did not meet the requirements for an additional step. Similarly, blowers (*K-101/107*) are placed in all grinders/mills to provide an efficient gas outlet to prevent temperature changes and dust accumulation. These outlets are equipped with dust catchers, collecting bags and filters to minimize the release of undesired particles to the environment[75].

Prepared raw materials are introduced into the rotary kiln (*D-102*), after passing through a preheating tower (*E-101*) and precalciner (*E-102*). Solids were heated to temperatures reaching 1400°C using this set-up. Vent gases, namely CO_2, are formed and flow in a countercurrent fashion from the rotary kiln to the top of the preheating tower, from where conditioning before their release to the atmosphere was performed in a cooling tower (*E-104*). In addition, the process by which the system is fed with fuel (coal in this case) was also designed, in which milling (*A-102*) was conducted before entering the calciner and rotary kiln. Chemical reactions undergone were formulated in reactions R12-R16 (see appendix C), each of them being predominant in a specific temperature range[76].

The formation of the different clinker phases strongly depends on the temperature inside the kiln. At temperatures between 700–900°C, the decomposition of calcium carbonate takes place, leading to the formation of CaO and the release of CO_2. As the temperature increases to approximately 900–1300°C, silicates, aluminium and iron compounds begin to form. At temperatures above 1300°C, liquid phase appears, promoting the formation of (Ca_3SiO_5, C_3S in short), which is the main compound responsible for the mechanical strength of Portland cement[77].

Once the clinker leaves the kiln it is rapidly air-cooled (*E-103*), which was also used as secondary and tertiary air sources[78], and further transported to the clinker mill (*A-103*) where the final grinding and blending operations with inlet gypsum ($CaSO_4$) and other additives produced the cement powder.

5.1.2 Concrete preparation

Different concrete formulations are required for the buffer and the backfill due to the different functional requirements of each component. The buffer requires high density and mechanical resistance for radiation shielding, while the backfill requires lower density and good flow properties to ensure proper filling of the disposal tunnels.

Figure 20 shows the processes required for the production of low- and high-density concrete. In the first case foam was generated by mixing compressed air with water and the foaming agent of choice, after which mortar (cement, sand and other minor additives) was amalgamated with the foam, leading to the desired material that was emplaced as described in section 5.2.4. For the concrete buffer, mixing was performed in two steps in series, namely a dry followed by a wet stage. Afterwards, the buffer was cast as explained in section 5.2.2.

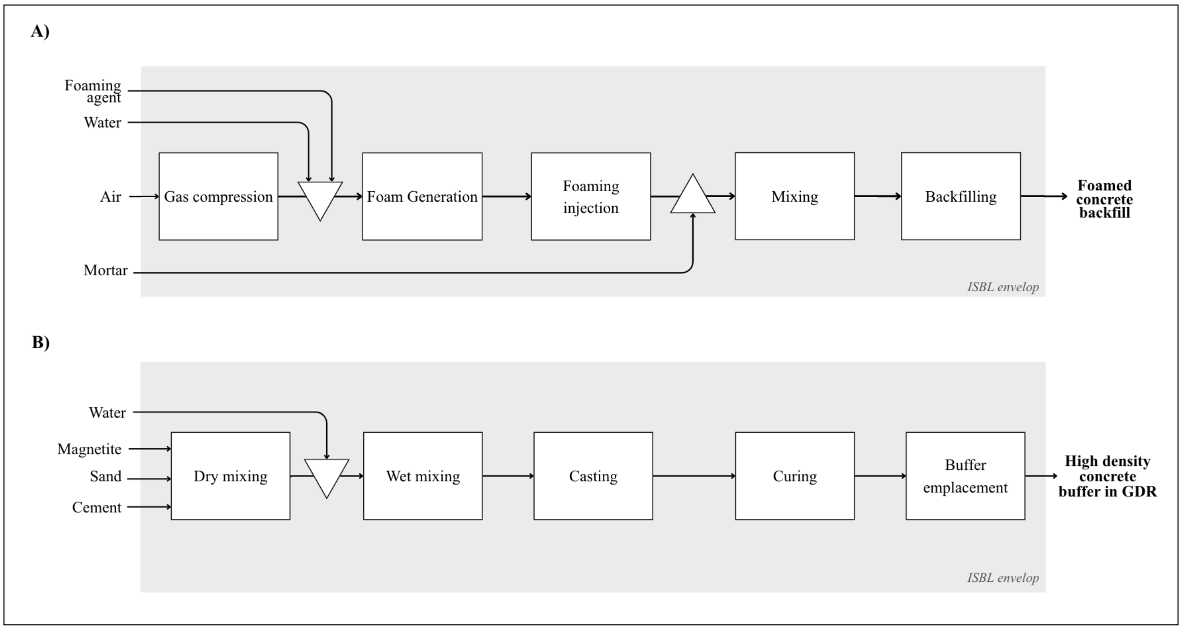

Figure 20: Concretes block diagrams: low density-foamed backfill (A) and high density buffer (B).

5.2 Disposal process

5.2.1 Manufacturing of carbon steel overpack

The steel overpack will be made from 4 components, namely a welded cylinder, a bottom cap, a flange, and a lid to cap off the top of the cylinder. Both the bottom cap (1) and flange (3) will be welded on each side of the cylinder. To be able to move the cylinder, a steel mushroom will be welded to the top of the lid after placing the vHLW inside (4). Finally, the bolts will be capped (5), this form can be further processed into the final disposal package by placing it into the buffer. The process steps to form the complete overpack are depicted in figure 21.

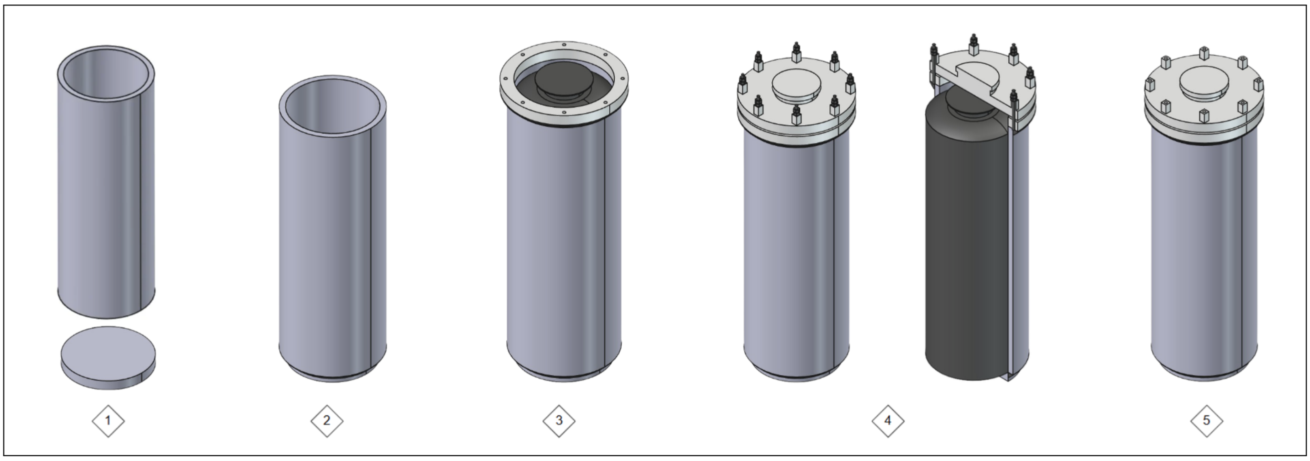

Figure 21: Manufacturing process of overpack.

5.2.2 Manufacturing of buffer

To obtain a stable and homogeneous buffer while minimising radiation exposure to workers, a remote concrete casting system will be used. Steel moulds were chosen because they can withstand the pressure exerted outwards by the concrete during curing. European standards such as EN-206[79] and EN-13670[80] should be followed for this process.

The casting process consists of six main steps that were outlined in figure 22. Firstly, an empty mould, which is placed upside down to ensure that the cast retains the objective qualities, is filled with concrete (1), followed by vibrating the whole cast to compact the concrete once the mould is completely loaded (2). Next, before the cement is totally cured, the inside walls are brushed to ensure adhesion of the concrete that will poured when placing the vHLW inside (3). Afterwards, the carbon overpack containing the vHLW is placed using remote control (4) after which concrete is cast over the canister to cap off the buffer and fill in any voids (5). Finally, the concrete is left to cure (6), allowing the disposal package to be moved into the GDF when hardening is completed.

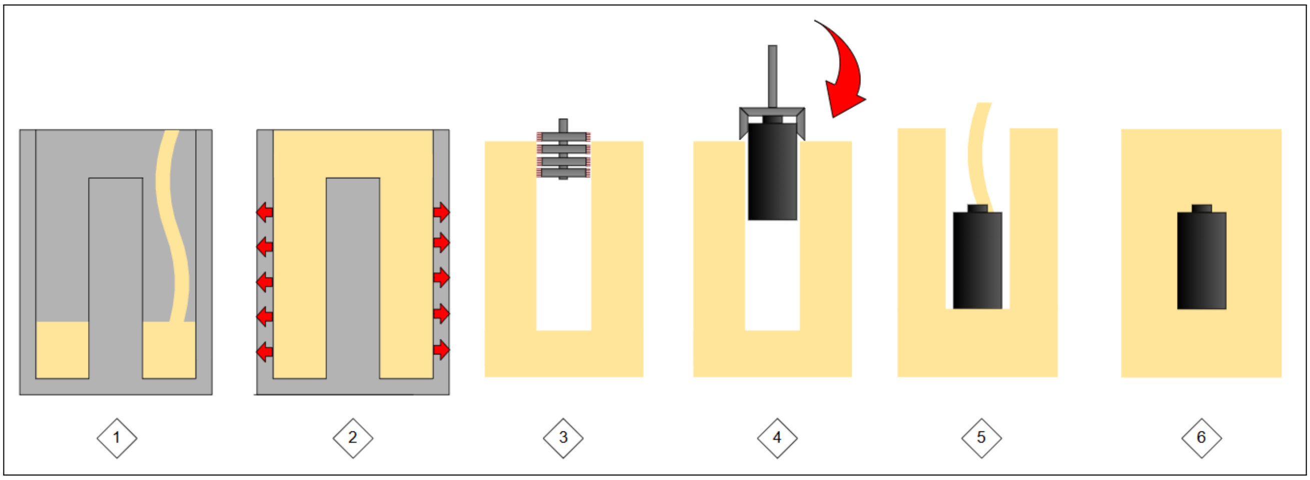

Figure 22: Casting of the buffer inside the mould.

5.2.3 Emplacement process

Before emplacement, part of the tunnels is already filled with foamed concrete and coated with epoxy to facilitate the use of the air-cushion vehicles. In the disposal tunnels, divots have been casted in the floor to act as a holding mechanism for the disposal package. Once the pre-filled foamed concrete and the epoxy are settled, the vehicle is lowered carrying a disposal package and advances through the main tunnel (transport tunnel) until it reaches a disposal tunnel, where the disposal packages are placed from the end of the tunnel to the beginning of the tunnel. This is visualised in figure 23.

When the emplacement vehicle reaches the designated location for the disposal package (1), the vehicle gently lowers it by slowly separating its loading arms (2) until the disposal package is settled in the divot (3). The vehicle then retracts and leaves through the transport tunnel to the shaft to get the next load.

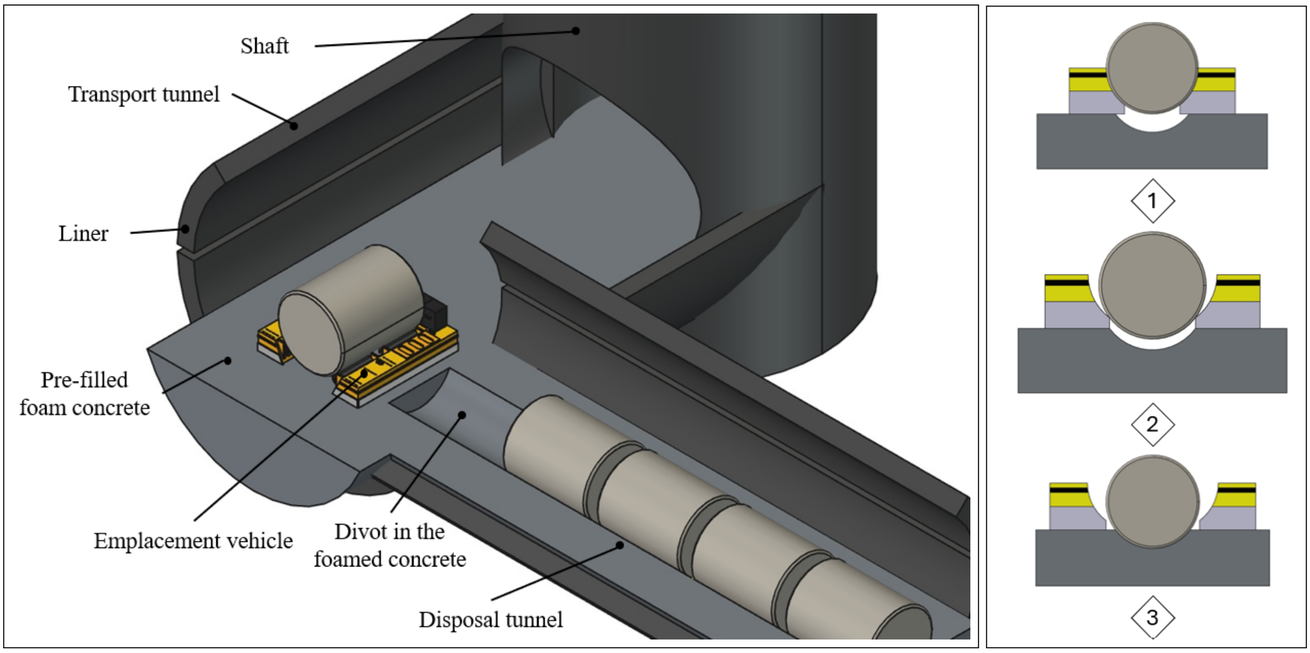

Figure 23: Emplacement of the super-containers inside the disposal tunnels (A) and into the divot (B).

5.2.4 Backfilling process

The backfilling is intended to take place 10 years after placing the last disposal package in the disposal tunnel. After this waiting period, raw materials for the foamed concrete are transported into the main gallery. A mixing and pumping machine is placed close to the disposal tunnel. First, the ventilation duct is removed from the disposal tunnel, after which a concrete pumping pipe is put back in the place where the duct used to be. When the pipe has reached the end of the tunnel, the raw materials are mixed into the foaming concrete. This is subsequently pumped into the back of the tunnel. During filling, the pumping pipe is slowly pulled back from the tunnel to continuously pour the full tunnel in one go.

6 Process control

6.1 Piping and Instrumentation Diagram

With regards to the cement manufacturing plant, a control system was designed to ensure that factors such as safety, efficiency and product quality were met. Ideal operational conditions can be attained by making use of this tool, which generally includes the control of parameters like temperature, pressure, levels and costs.

The Piping and Instrumentation Diagram (P&ID) can be visualised in figure C2, which includes a total of nine Pressure Indicating Controllers (PIC), two Temperature Indicating Controllers (TIC) and two Pressure Differential Controllers (PDC). The controllers were displayed in such a way to enhance visualisation; however, in practice a complete control loop would be installed, although only the main controller symbols are shown in the simplified P&ID. They would also be equipped with alarms and automatic shutdown systems.

In general, proportional–integral–derivative controllers (PIDs) were installed in all grinding (*CR-101*, *A-101/103*) and solid separation steps (*S-101/103*) in which a fine dust or air outlet was present. The controller will measure the corresponding variable at the mounted unit, and deviations from the set point (1 atm) will lead to an increase in gas flow rate, preventing pressure build-up. This strategy also minimises dust leakage, protects the equipment from overpressure, and maintains stable operating conditions. Issues associated with accumulation of solids are not easily addressed by this type of controller and therefore require periodic inspection and maintenance. Hence, it would commonly entail a design adjustment of the equipment in which steeper internal walls, a larger diameter discharge outlet or a higher conveyor belt speed should be considered. Similarly, hoppers (*V-101/102*) displayed PIDs to prevent damage to the system. Nonetheless, with this approach only an indication of pressure changes would be given, after which manual operations to clear the unit should be performed. Finally, the rotary kiln (*D-101*) and cooling tower (*E-104*) had TICs incorporated to adjust temperature by modulating the inflow of utilities, namely air and water, respectively. In case of gas build-up in the rotary kiln, specifically in the preheating tower and burner inlet, two PID systems were installed to regulate the outflow of gases to the cooling tower or atmosphere. Overall, the proposed control system maintains stable operating conditions while improving process safety and product quality.

6.2 Quality control

6.2.1 Carbon steel overpack welding

As previously described, the carbon steel overpack is manufactured by welding the individual components into a single final structure that surrounds the vHLW in its canister. During the process of welding, defects that weaken the joint and affect the structural integrity of the assembly can occur. Generally, weld flaws can be subdivided into five categories, namely lack of penetration, cracks, slag inclusions, porosity, and harmful surface defects[81]. In table 14 some of these internal and external flaws were listed.

Table 14: Common types of welding defects[82].

Type	**Characteristics**	**Prevention**	**Corrective action**
Cracks	Tear or fissure in the weld or base material, which can be longitudinal or transversal	Not allow base material to cool quickly and clean joint before welding	Grind and weld repair
Porosity	Trapped gas in the weld once cooled	Remove rust, grease and moisture from joint	Grind until pores are eliminated and weld repair
Undercut	Groove present in the weld	Maintain appropriate arc length and decrease travel speed	Grind until undercut blends with base material and repair if needed
Under fill	Weld is below the external surface	Slow down welding and adjust electrical power output	Apply additional weld beads until it is completely filled
Incomplete fusion	No proper bonding between welding and base material	Increase electrical power output	Grind weld to original metal and repair the affected area
Incomplete penetration	Weld beads do not reach the bottom of the joint	Decrease travel speed and adjust torch position	Grind weld to original metal and repair the affected area

In order to prevent these defects, several inspection methods can be employed, among which destructive, proof and non-destructive tests can be applied[81]. Destructive tests would preferably be used during the welding process design phase, where a series of tests are conducted to determine the operating conditions and the procedure that will be followed. On the other hand, non-destructive tests are commonly preferred, as they preserve the integrity of the structure and allow their use after ensuring the proper function of the weld. Below, several methodologies were outlined depending on the type of weld flaws.

- **Visual inspection** includes those inspections that are only performed without auxiliary equipment[81].It is cost-effective for surface defects but has a high dependency on the experience and judgement of the inspector and weld type. Other factors that may affect the process are width of defect, light reflection, and degree of surface smoothness[81]. Hence, coupling this investigation with other approaches should be conducted to attain a proper and sound evaluation.
- **Radiography** is a method that uses an X-ray or gamma ray source to produce an image by passing the radiation through the welded material. The presence of voids will lead to a more exposed area due to radiation passing these features with ease. It is relevant to highlight that this methodology is highly sensitive to fine flaws and materials that absorb the entire incident ray energy[83].
- **Ultrasonic inspection** employs sound waves (high frequency) that propagate along the material. In the presence of internal defects, such as cracks or voids, the wave will be reflected and the corresponding signal measured, showing that discontinuities exist. However, application in surface flaws is also possible. In addition, due to the excellent wave penetration deep defects can be detected. Weld flaws profiling can be performed by conducting tests from several locations, which would indicate the angle and depth of the potential crack[83].

Nevertheless, it is relevant to highlight that several basic inspection approaches are needed to completely fulfil the requirements for evaluating the quality of the weld.

6.2.2 Buffer casting

The quality of the concrete buffer must be checked during the casting process, as it affects the shielding performance, mechanical strength and long-term durability of the disposal package. The main defects that may occur during buffer casting are void formation, cracking, improper density and displacement of the overpack inside the mould.

Before casting, the composition and density of the concrete should be verified to ensure that the mixture meets the design specifications. In addition, the water-to-cement ratio and the amount of magnetite aggregate should receive more attention, as these parameters directly affect the final properties of the buffer. These checks should be performed following established concrete testing procedures.

Another important issue is the formation of voids inside the concrete. To minimise this risk, the amount of concrete introduced into the mould should be monitored and compared with the expected volume. Visual inspections during casting can also be used to identify filling problems.

Since the disposal package contains an overpack surrounded by concrete, the position of the overpack should be verified before casting to ensure a uniform thickness. Any displacement during the operation may reduce the protection provided by the concrete barrier.

After casting, the curing process should be monitored to ensure proper concrete hardening. Since heat is generated during this stage, the concrete temperature should be monitored throughout the curing period. High temperatures may affect the final properties of the buffer. Also, visual inspections should be carried out to identify cracks or other visible defects. The dimensions of the disposal package should then be checked to ensure that the required specifications are met. Finally, the results of these inspections should be recorded to verify that the disposal package meets the design requirements.

6.2.3 Emplacement process

The emplacement operation is responsible for transporting and positioning the disposal package inside the tunnels. Since the package contains vHLW, any damage during transport or incorrect positioning could affect facility operations. Potential issues during emplacement include incorrect positioning, misalignment of the package, excessive transport speed, loss of stability of the transport system and failures in the remote-control equipment.

To minimise these risks, several inspections and operational checks should be carried out before and during the emplacement process. Before the operation starts, the transport vehicle, air-cushion system and remote-control equipment should be tested to verify that all systems are functioning correctly.

During transport, parameters such as transport speed and air-cushion pressure should be monitored continuously. Excessive speed can increase the risk of impacts and mechanical damage, while insufficient air-cushion pressure could affect the stability of the vehicle and the disposal package. Position and alignment measurements should also be performed to ensure that the package remains correctly oriented and follows the planned emplacement path.

Once the disposal package reaches its final location, its position should be verified compared with the predetermined layout and the required spacing between neighbouring packages. Finally, a visual inspection of the package and transport equipment should be performed whenever possible to identify any visible signs of damage that may have occurred during the operation.

6.2.4 Backfilling process

This quality control is crucial to ensure the complete and safe closure of the tunnels, as well as the time that the backfilling takes. So, in general, some qualities of the foamed concrete have to be checked, especially its flowability and curing time. Apart from that, calibration and testing has to be done to the equipment used for mixing, the pipelines used for pumping the concrete and the pumps to displace the concrete.

Firstly, to ensure that the concrete has the needed properties, the concrete has to be tested to see if the particles used are fine enough to guarantee optimal curing time and good flowability of the concrete. Moreover, the water/cement ratio must be checked before mixing to aerate the concrete so it can be pumped with ease, but not more than the optimal amount to avoid large curing times[84]. These can be tested by measuring correctly the amount of ingredients of the concrete.

The curing process can be tested by using test samples of the foamed concrete to check how much time the concrete needs to cure to verify that the concrete will settle correctly inside the disposal tunnels[34].

Lastly, the mixing has to be monitored and checked beforehand to assure that the concrete is well mixed and to make the concrete as isotropic as possible. Moreover, the pumps and the pipes need to be cleaned and monitored to avoid fouling in those equipment, which can be avoided by using different retractable pipelines for each tunnel and back-up pumps to ensure a correct backfilling process.

7 Balances and utility requirements

vHLW disposal packages continue to generate heat during and after emplacement, therefore, in order to maintain operability of the GDF, cooling and ventilation are required. The geological disposal facility was designed to accommodate around 8000 canisters with a maximum of 39 disposal packages per tunnel. Hence, ventilation requirements per tunnel will be calculated.

7.1 Heat balance

Three different heat fluxes were considered: 200 W, 400 W and 600 W (case A, B and C, respectively) corresponding to above ground storage times of 130, 80 and 55 years. In the presence of such heat loads, air cooling has to be provided. To this end the disposal tunnel is modelled as a plug-flow system (PFS) following the reasoning presented in Appendix D1.

Since only the disposal tunnels are thermally active, the transport tunnels and shafts can be treated as adiabatic, with no change in air temperature along these sections. As a result, the ventilation circuit has three different sections. The air temperature profile around the full circuit presents the following conditions:

$$T = \begin{cases} T_{\text{in}} & \text{shaft in, transport in (adiabatic)} \\ T(z) & \text{disposal tunnels, } 0 \le z \le L_d \\ T_{\text{max}} & \text{transport out, shaft out (adiabatic)} \end{cases}$$

By applying the PFS model, the steady-state energy balance over a differential slice dz (where z is the coordinate along the length of the tunnel) of the disposal tunnel can be derived as shown in equation 14, see further detail in Appendix D2. Here it is assumed that the cooling air enters the tunnel from the cooling duct uniformly along its length.

$$\frac{dT}{dz} = \frac{T_{in} - T}{z} + \frac{\dot{Q}_{lin}}{cp_{air}\, \dot{m}_{air}\, z}, \qquad 0 \le z \le L_d \tag{14}$$

Where $\dot{Q}_{lin}$ is the linear heat generation from the waste in [W/m], $\dot{m}_{air}$ is the mass flow of cooling air entering the tunnel, per unit length. The solution of this differential equation, once again detailed in appendix D2, leads to the following expression of $T(z)$:

$$T(z) = T_{in} + \frac{\dot{Q}_{tot}}{cp_{air}\, \dot{m}_{air}} \tag{15}$$

which indicates a constant temperature profile across the length of the tunnel. This equation will be employed in section 7.1.1 to calculate the minimum ventilation duct diameters as a function of $v_{\text{duct}} \le v_{\text{max}} = 8$ m/s, which is the maximum allowable velocity in mine airways[85].

7.1.1 Ventilation ducts

Inside each disposal tunnel a ventilation duct of an inner diameter d_v runs above the disposal package (outer diameter D), the minimum ventilation duct diameter can be calculated with the following formula while maintaining the safety constraint:

$$v_{\text{duct}} = \frac{4\, m_t}{\pi\, \rho_u\, d_v^2} \le v_{\text{max}} \qquad d_{v,\text{min}} = \sqrt{\frac{4\, m_t}{\pi\, \rho_u\, v_{\text{max}}}} \tag{16}$$

Where $\dot{m}_t$ is the total mass flow inputted in the inlet of the ventilation duct and is equal to $\dot{m}_{air} \cdot L_d$. However, due to the depth of the tunnels, there could be a significant pressure drop inside the ducts, so to account for this, the pressure difference was calculated with the Darcy-Weisbach formula assuming a length $L_t = 110$ m and friction factor $f = 0.02$. Equation 17 showcased the example calculation for the scenario with the highest heat flux (case C with $d_v = 0.20$ m), namely 600 W, giving a negligible pressure drop of 457 Pa with which inline ventilation was found applicable without needing extra infrastructure[85].

$$\Delta P = f\, \frac{L_t}{d_v}\, \frac{\rho_u\, v_{\text{duct}}^2}{2} = 0.02 \cdot \frac{110}{0.20} \cdot \frac{1.30 \times 8^2}{2} \approx 457 \text{ Pa} \tag{17}$$

7.1.2 Temperature constraint and working safety

The Dutch health and safety laws *Arbeidsomstandighedenbesluit* article 6.1[86], does not explicitly give a maximum working temperature, thus, to ensure the safety of the workforce an assumed target temperature of the tunnels was chosen, at 28°C, as a binding constraint. For cooling it is assumed that the cooling air temperature T_{air} is kept at 15°C. This would require active cooling of inlet air during the summer months. Inputting these values in equation (15) yields the values for $\dot{m}_t$ reported in table 15. Additionally, duct sizing is carried out on the basis of Equation D21 and reported in the same table. The results align with previous estimation of 0.4m[87].

Table 15: PFS results per disposal tunnel ($n = 39$, $L_t = 110$ m, $T_{\text{in}} = 15$ °C, $T_{\text{max}} = 28$ °C, $\Delta T = 13$ K, $v_{\text{max}} = 8$ m s^{-1}, $\rho_u = 1.30$ kg m^{-3}, $f = 0.02$).

Parameter	**Case A (200 W)**	**Case B (400 W)**	**Case C (600 W)**
Per-tunnel heat load Q_t (kW)	7.8	15.6	23.4
Linear heat density q (W m^{-1})	70.9	141.8	212.7
Required mass flow m_t (kg s^{-1})	0.60	1.19	1.79
Temperature gradient dT/dz (K m^{-1})	0.118	0.118	0.118
T at all z (°C)	28.0	28.0	28.0
Min. duct diameter $d_{v,\text{min}}$ (m)	0.27	0.38	0.47
Duct velocity v_{duct} (m s^{-1})	8.0	8.0	8.0
Pressure drop ΔP (Pa)	457	457	457

The PFS analysis per disposal tunnel shows that the required mass flow $\dot{m}_t$ scales linearly with emitted thermal power. Consequently the duct size also changes to accommodate the larger flow rate while remaining under the set maximum velocity of 8 m/s.

7.2 Cooling utility

The total volumetric air flow rate supplied to each tunnel at underground conditions, with $\rho_{air} = 1.30$ kg m^{-3} was found to be 94, 188 and 282 m^3/s for each scenario, respectively (see equation D22). During most of the year an inlet temperature of 15°C can be achieved just by pumping air from the outside. However in the warmer months, pre-cooling will be needed. Here the return air stream exiting the tunnel is used for the specific purpose of cooling, so independently of air recycle which will have to be carried out separately. Thus the required cooling capacity can be calculated as:

$$Q_{\text{cool,tot}} = \dot{m}_{\text{fac}}\, c_p\, (T_{\text{return}} - T_{\text{in}}) \tag{18}$$

Assuming a vapor-compression chiller with coefficient of performance of around 4 (COP)[85], this gives a power as seen in equation 19, which results in the corresponding values for each of the studied cases, namely 400, 800 and 1200 kW, respectively (equation D23).

$$W_{\text{cool}} = \frac{Q_{\text{chiller}}}{\text{COP}} \tag{19}$$

The system commonly employed to cool air consists of an evaporator-compressor-condenser closed-loop in which a refrigerant is circulated and a blower (fan) pushes air across the coils or tubes of the evaporator, producing the desired utility. The cost of such equipment utility was computed using equation C29 (a=24000, b=3500, n=0.9[88]), where the size S corresponds to the power (evaporation duty) found in equation D23 for each case. Hence, the purchase price was found to be 0.69, 1.27 and 1.83 M€, respectively. Accounting for material of construction (f_m=1.3[88]), location (f_l=1.19[88]) and installation factor (f_i=2.5[88]) the cost would rise to a total of 2.66, 4.91 and 7.04 M€ for each case.

8 Equipment list and unit design

The equipment list was created as a function of the several tasks that must be conducted within COVRA premises to ensure a proper functioning of the disposal facility, namely, from the completion of the casting processes after positioning the vHLW in the provided prefabricated concrete container to the closure of the disposal tunnels. Therefore, in table 16 the required equipment for each stage, namely buffer manufacturing, overpack manufacturing, drilling process, emplacement process and backfilling process, were listed. Whenever possible, commercially available equipment was selected. The equipment was chosen based on the requirements of each step, such as load capacity and dimensions.

Table 16: Equipment list.

Equipment	Characteristics	Model
Twin shaft concrete mixer[89]	Load=1-8 m^3 Production = 40-360 m^3/h Power = 110 kW	MAO 4500/3000
Concrete hopper[90]	Dimensions = 2.3x2.1x1.78 m	Model 4T-3/16-EL-1620
Welding kit[91]		Tungsten inert gas arc welding
Concrete pump[92]	Horizontal conveying=50-150 m Pipe diameter=80-125 mm Weight=1500-2000 kg Power=37kW	YG-30
Air cushion transport[87, 93]	Air pressure=0.6-0.8 MPa Air capacity=25 m^3/min Loading capacity=5-60 tons Air cushion area=1.2 m^2 Length=3 m Width=3 m Power=30kW	FADA CRT
Ventilation duct (disposal tunnel)[87, 94]	Diameter=0.4 m Total length=17650 m	Flexible duct, Triple Lock Aluminium Flex Duct
Ventilation duct (transport tunnel)[87]	Diameter=1 m Total length=6250 m	Flexible duct, Triple Lock Aluminium Flex Duct
Fans for ventilation[95]	Power=0.55 kW Weight=65 kg Speed=2860 rpm Flow rate= 4260 m^3/h	SODECA HCT/IMP-C-UNI-35-2/4T
Shaft hoisting system[87, 96]	Diameter=6 m Depth=500 m Load=50-100 tons	Saxon
Open face tunnel boring machine[87, 97]	Diameter=5 m	WM960II

The air-cushion transport was the main equipment examined in detail due to its important role in the emplacement of the disposal package, as its dimensions should remain within the limits of the tunnel diameter, while still allowing to transport the desired weight. Based on the technical information provided by the manufacturer a loading capacity up to 60 tons, with an air power source between 0.6 and 0.8 MPa, was possible. Therefore, by taking a 10% safety margin in both variables the area required was computed based on equation 20 as a function of the vehicle capacity (m), gravity (g) and pressure displayed by the transporter (P).

$$A = \frac{m \cdot g}{P} = \frac{66 \cdot 10^3 \cdot 9.81}{0.54 \cdot 10^6} = 1.2\, m^2 \tag{20}$$

As a result, it was found that a minimum area of 1.2 m^2 was required, assuming this to be only 50% of the total bottom surface area based on the provided sketch[93]. Moreover, the actual dimensions of the vehicle were calculated using the geometry given in figure 7 as basis, where the side arms (length analogous to disposal package) and back width were assumed to be equal. Nevertheless, it was approximated that the side arms would be the features to lift the totality of the weight, leading to them having a surface area of 2.4m^2.

Hence, the dimensions of the vehicle to transport a disposal package with a diameter and length of 2 and 2.5 m, respectively, were 3x3 m (width x length). This remained within the limits of the equipment, which had a maximum cargo size of 3x5 m. However, this was accounting for a higher total weight, meaning that with an alike air power, a smaller transporter could be attained as far as its production remained feasible. Due to this fact, production viability was found to be the main constraint, as the technology's capability would allow a relatively small vehicle to be built, while transportation of the 22 tons would be still possible.

In addition, the complementary equipment was sized based on available literature values, as such machinery will be directly purchased from a supplier and used for the corresponding process stage. Nevertheless, several modifications were performed to adapt the found equipment to the actual conditions, which are outlined below:

- **Boring machine head for clay**: in order to drill through the clay, a special head for the boring machine is necessary. This head is manufactured by the same company as the boring machine, and it is compatible with the model referenced and used for this type of host rocks[97].
- **Tungsten inert gas arc welding**: was selected owing to its major use in alike surfaces without known problems, especially for pieces that are subjected to stresses[82].
- **Two different ventilation duct geometries** were used according to literature references[87], where for cost reduction purposes smaller diameters were employed in the disposal tunnels.
- **The hoisting system** purchase was required to be done by parts (crown blocks, deadline anchors, drawworks, drilling lines, swivels, travelling blocks). Moreover, this equipment can be customized by the client, so the dimensions can be changed and arranged.

9 Health, Safety, Environment & Sustainability

This section covers the Health, Safety, Environment (HSE) and sustainability aspects of the disposal process of vHLW. A Life Cycle Assessment (LCA) is conducted to determine the environmental impact of the disposal. For the health and safety aspects, a Hazard and Operability (HAZOP) study was performed, which was then applied to look at inherently safe design options and formulate a bow-tie diagram.

9.1 Life Cycle Assessment

To assess the environmental impact of the vHLW disposal, an LCA was performed. Since the product is inherently related to the disposal of a waste stream, a *cradle-to-grave* approach was chosen. The functional unit (FU) was defined as 1 disposal package of vHLW emplaced in the geological disposal facility. Figure 24 summarises the product life cycle, from the extraction of the raw materials and the generation of HLW in nuclear reactors to the final disposal of the waste package. The diagram also depicts the transport modes considered. Freighters were assumed to supply magnetite from Norway to the concrete manufacturing facility (Romein Beton) and for the delivery of canisters to the disposal site. Road transport by trucks was assumed for materials such as sand or cement that can be purchased from suppliers within the region. Cargo trains were chosen for the movement of the waste from the nuclear reactors to the reprocessing facilities (France) and back to COVRA. Similarly, energy-intensive steps that were considered relevant for this analysis were marked accordingly.

Several assumptions were made to simplify the LCA. For instance, the upstream processes related to the production of the HLW from nuclear reactors were neglected. Nevertheless, the materials for the construction of the overpack and canister were included in the analysis. In addition, all concrete production was assumed to be one step, after which it was allocated to the buffer casting or the backfill process. In reality, the backfill material should be made on site in a batch process, after which it is pumped into the disposal tunnels. Similarly, concrete buffers are not cast in one step, as a large part of the buffer is cast before placing in the vHLW, and the final casting takes place at a different location. This was neglected as energy requirements should not deviate significantly. Furthermore, excavated tunnel calculations were used to estimate the corresponding volume per container. The excavated volume includes disposal tunnels, transport tunnels and vertical shafts.

Finally, energy consumption of the machinery required, namely the backfilling pump[98], concrete mixer[89], emplacement machine[93] and excavation driller[99] were assumed to be powered by electricity from natural gas generated in the Netherlands.

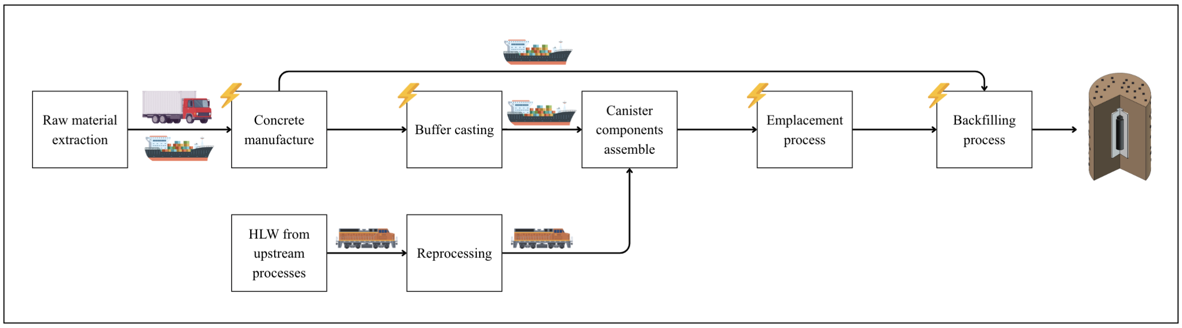

Figure 24: LCA *cradle-to-grave* diagram.

All the components and processes expected to have an impact on the environment were listed, and the corresponding amount needed per functional unit was calculated, as shown in table 17. Corresponding values of the carbon footprint were obtained from the *Ecoinvent*[100] and *Idemat*[101] databases, yielding a total of approximately 34 t $CO_{2,eq}$ per functional unit. A similar approach was followed to calculate the environmental impact score (*points*) by summing the contribution of the different categories that account for factors like climate change, ozone depletion, human health effect, landfill hazards and land use. This approach is especially relevant for the comparison of two competing scenarios where not only the CO_2 emissions are considered but also other hazardous effects.

Table 17: Life Cycle Assessment results per FU.

	Amount	**$CO_{2,eq}$/FU**	**Pt/FU**
Carbon steel overpack (kg)	550	906.68	0.29
Cement Portland (kg)	11610	9984.60	0.46
Concrete backfill pump (kWh)	65	25.38	0.00
Concrete mixer (kWh)	300	117.72	0.00
Deionized water (kg)	7078	6.37	0.00
Emplacement machine (kWh)	2	0.82	0.00
Excavation machine (kWh)	798	313.27	0.01
Magnetite (kg)	18788	18412.24	1.87
Plasticiser for concrete (kg)	7	9.97	0.00
Polymer foaming (kg)	786	157.20	0.06
Silica sand (kg)	15035	601.40	0.07
Stainless steel 316L canister (kg)	113	610.25	0.25
Transport-Freighter (tkm)	50929	1018.57	0.08
Transport-Lorry (tkm)	7994	719.42	0.03
Transport-Train (tkm)	30800	1232.00	0.13
TOTAL		34115.87	3.26

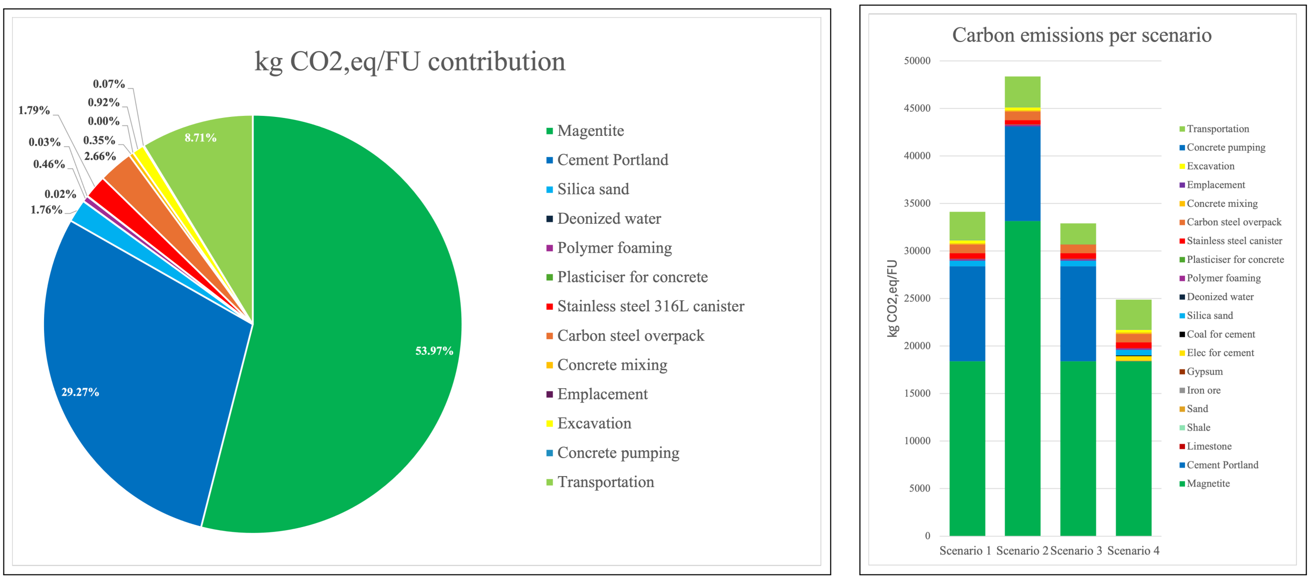

Figure 25: LCA results: CO_2 emissions per disposed canister of vHLW (A) and comparison of base with alternative scenarios (B).

The primary contributor to carbon emissions was found to be the extraction of magnetite (54%), followed by the production of Portland cement (29.2%), while other materials were proven to be a minor addition to the total carbon equivalences (2.4%). Finally, transportation accounted for approximately 8.7%, which entailed the delivery of all materials from the primary supplier to the final location, whereas the remaining 5.8% originates from on-site activities such as mixing and pumping concrete, the excavation of the tunnels and emplacement of the disposal package.

Moreover, several scenarios (see figure 25B and table E1 for further details) were assessed in order to identify potential optimisations that could be implemented in the life cycle of the product to reduce the carbon emissions and other related hazards.

- Scenario 1 was the base case that aimed to describe the current production of the disposal package and its associated activities.
- Scenario 2 evaluated the substitution of other coarse aggregates in the concrete, namely silica sand, by magnetite to improve the shielding properties of the buffer, while the stainless steel 316L canister was replaced by ss304, which exhibited a lower environmental impact with still similar mechanical properties.
- Scenario 3 considered the use of a more eco-friendly energy source, such as wind-power, which was found to be the second largest energy production sector in the Netherlands, as well as selecting a German company (Cofermin Group) as the supplier for magnetite, reducing transportation-related emissions.
- Scenario 4 investigated the potential improvement of employing the designed cement manufacturing plant, for which the impact of the product itself was substituted by the sum of the associated emissions of raw materials (limestone, shale, sand, iron ore, gypsum), which were assumed to be available within a 300 km radius from the site, and energy inputs (electricity from natural gas and coal).

Based on the described scenarios the corresponding calculations were made to estimate the amount of CO_2 and the associated *points* per functional unit. It was found that full substitution with magnetite would increase the environmental impact up to approximately 48 t $CO_{2,eq}$ per functional unit (+42%), while with the on-site cement production, around 9 t of $CO_{2,eq}$ could be prevented (-27%). On the other hand, the substitution of the energy source had a minor impact (-4%), showcasing that the processes involved in the disposal of vHLW are not energy-intensive. With regard to the total *points* score, a similar trend was observed. The main difference being Scenario 4, where the decrease in CO_2 emissions was not proportional to the decrease in *points*. This can be explained by the fact that cement production has a large carbon emission, which can be reduced. Whereas the other factors accounted for in the *points* score are not influenced as much.

From a sustainability perspective, on-site production of cement appears to improve the environmental performance of the system, which should be considered as a potential benefit given that the economic cost remains comparable to the direct purchase of materials. In addition, optimisations such as a transition towards local suppliers or making use of green energy sources are measures that could reduce the CO_2 emissions. Magnetite remains the most significant contributor to emissions and should therefore be the main target for improvements.

9.2 Hazard and Operability Study

A HAZOP analysis was performed to identify potential hazards and operational issues associated with the proposed disposal system. The analysis focused on the overpack manufacturing, concrete mixing, buffer casting, and waste package emplacement. For each node, important process parameters, possible deviations, causes, consequences and mitigation measures were identified, as shown in table 18.

- **Node 1 - Overpack manufacturing**. Focus on identifying potential deviations that could affect the quality and integrity of the carbon steel overpack.
- **Node 2 - Magnetite concrete mixing**. Deviations during mixing may affect the composition, homogeneity and overall performance of the final material, therefore potential failures that could compromise the quality of the engineered barriers were analyzed.
- **Node 3 - Buffer casting**. This stage was investigated to identify potential deviations that could affect the quality and performance of the disposal package.
- **Node 4 - Emplacement**. The emplacement stage involves the transport and positioning of the disposal package inside the tunnel, for which potential failures and their impact on safety and operability were assessed.

Table 18: HAZOP analysis.

Parameter	**Deviation**	**Cause**	**Consequence**	**Safeguards / Recommended actions**
Node 1 - Overpack manufacturing				
Wall thickness	Lower	Contractor error	Reduced mechanical strength, lower corrosion resistance, reduced lifetime of the overpack	Dimensional inspection at delivery from manufacturers
	Higher	Contractor error	Improper fit with canister, higher production cost, difficulties during handling	Dimensional inspection at delivery from manufacturers
Steel carbon content	Lower	Contractor error	Lower corrosion resistance, higher deformability	XRF composition testing at delivery from manufacturers
	Higher	Contractor error	Fragile behaviour, lower weldability due to decrease in melting point	XRF composition testing at delivery from manufacturers
Welding current	Lower	Operator error, inadequate power source	Poor adhesion, eased water ingress	Welding temperature control, visual assessment of welds, operator training
	Higher	Operator error	Heat altering of the steel, spatter, high weld porosity	Welding temperature control, non destructive testing of welds, operator training
Node 2 - Magnetite concrete mixing				
Mixing speed	None	Mixer failure, loss of power supply	Concrete hardening inside mixer, production interruption, high levels of dust exposures for workers during the cleaning	Equipment maintenance, emergency power supply, mixer monitoring, duplicate drive motor
	Lower	Motor malfunction, incorrect speed setting	Poor dispersion of components, reduced homogeneity, inconsistent concrete properties	Routine inspection and maintenance of the motors, monitoring mixer performance
Mixing time	Lower	Unexpected shutdown, operator error, timer malfunction	Incomplete mixing, non-uniform material properties	Operating procedures, mixing time verification
	Higher	Operator error, timer malfunction	Setting of concrete inside the mixer, high levels of dust exposures for workers during the cleaning	Operating procedures, mixing time verification
Magnetite aggregate fraction	Lower	Incorrect measuring of components	Reduced shielding performance, lower mechanical strength, increased permeability	Density measurements
Node 3 - Buffer casting				
Casting rate	None	Pump failure, blockage, loss of power supply	Production interruption, concrete hardening before placement, disposal package delays	Equipment maintenance, backup power supply, equipment monitoring
	Lower	Partial blockage, pump malfunction, operator error	Uneven concrete placement, longer production time, lower product quality	Equipment inspection, flow monitoring
Concrete filling	Lower	Insufficient concrete availability, early interruption of casting, leakage from the mould	Voids in the buffer, reduced shielding performance, lower mechanical strength	Raw material availability verification, mould inspection
Curing time	Lower	Early removal from mould, inadequate curing conditions	Reduced mechanical strength, cracking, lower durability	Curing procedures, curing time verification, quality control testing

Curing temperature	Higher (>40°C)	Unexpectedly high heat generation from the HLW, high ambient air temperature	Reduced mechanical strength, cracking leading loss shielding or/and facilitated water ingress	Use cold utilities for temperature control
Node 4 - Emplacement				
Speed	None	Loss of power supply, air-cushion failure, drive system malfunction	Delay in emplacement operations	Preventive maintenance, emergency power supply
	Higher	Control system failure, incorrect speed setting, sensor malfunction	Collision with tunnel wall, damage to disposal package, possible worker exposure during recovery operations	Speed control system, remote operation, emergency stop button
Position in tunnel	Incorrect positioning	Position sensor failure, operator error, vehicle failure, obstruction in tunnel, air-cushion malfunction	Package placed outside intended location, disposal operation interrupted	Position monitoring system, inspection of transport route, establish a recovery procedure for vehicle failure, verification of final position using more sensors
Position on vehicle	off-centre	Uneven surface, inaccurate unloading operation, lifting equipment failure	Uneven load distribution, difficulties during backfilling	Guide system in tunnel floor, operator supervision, alignment verification before final emplacement
Load weight	Higher	Underestimation of package weight, loading error, equipment error	Reduced vehicle stability, mechanical failure, package drop risk	Equipment design with safety factor, load specifications, verify package weight before transport, overload alarm

9.3 Inherently Safer Design

To ensure safety of the system, during all stages of operation, inherently safer design (ISrD) was applied. ISrD is an approach that could reduce the risk and likelihood of undesired events by means of minimising, substituting, moderating and simplifying parts of the system where the hazard could be released. These methods focus on reducing the hazardous materials or equipment, replacing them with intrinsically safer options and resolving design challenges by modifying the existing model rather than employing additional features.

An additional motivation to include these factors, is their greater ease of implementation during the design phase. Changes to the process will present a decreased economic viability with time, making the inclusion of safety principles less applicable the further the process is developed[102].

The aforementioned principles were applied to some of the scenarios discussed within the safety chapter (HAZOP) and in other relevant process steps required for the production of the final product. Hence, in table 19 potential measures that could be taken were listed as a function of each method to achieve an inherently safer design.

Table 19: Inherently Safer Design principles and corresponding applications.

Principle	Issue	Solution	Potential drawbacks
Minimize	High pump pressure for backfilling	Lower pumping distance	Personnel closer to radioactive waste, increased underground infrastructure
	Toxic additives in cement/concrete formulation	Use only essential additives	Hinder mechanical properties
	Neutron activation in the disposal package	Select materials lacking isotopes prone to neutron activation	Materials may not be optimal for the application in terms of mechanical properties
	Failure of emplacement equipment due to disposal package weight	Minimize package weight where possible	Reduced shielding, smaller safety margins
Substitute	Personnel accidents when handling equipment	When possible replace equipment with smaller/lighter equivalents	Increased difficulty in reaching production requirements
Moderate	Spills during concrete production	Reduce batch size	More batch cycles required to reach production requirement
	High radiotoxicity and heat generation of the waste	Increase above ground storage	Higher cost
	Potential package damage due to excessive speed	Limit transport operating speed	Long emplacement times
	Reduced overpack lifetime due to local defects	Increase overpack wall thickness	Higher material consumption and cost
Simplify	Incorrect concrete composition	Limit on-site processing and purchase directly from supplier	Higher cost
	Incorrect pipe positioning during backfilling	Use fixed pumping locations and procedures	Less flexibility to adapt to unexpected conditions
	Incorrect overpack dimensions	Standardize overpack geometry and manufacturing procedures	Reduced design flexibility

9.4 Vent gas emissions from cement production

With regard to the emissions produced from the industrial plant for cement manufacturing, several compounds were considered due to the relative environmental hazard that they present. These compounds are listed in table 20 (for additional information, see appendix E)[103]. It is relevant to highlight that these emissions are heavily dependent on the composition of raw materials and fuel, operational conditions, and equipment used. Optimisation of the industrial plant and potential equipment that could be included to minimise these emissions were also presented[75, 104].

Hence, management of the flue gas arose as a highly challenging task owing to its composition, presenting several compounds in a continuously varying ratio. This makes its sale to downstream industries difficult, as well as the implementation of established processes that are used in industry for the treatment of gas streams with a higher purity of a specific component. As a result, the application of optimisation and preventive measurements has been proved to be a more suitable approach[104].

Table 20: Principal vent gas emissions in kg/ton clinker[103, 104].

Compound	**Emission rate (kg/-ton)**	**Origin**	**Optimization measures**	**Mitigation equipment**
NO_x	0.4–6	Combustion of nitrogen in air or fuel with oxygen	Improved firing technique, optimized cooler connections, fuel selection	Selective catalytic reduction
SO_2	0.02–7	Sulphur content in raw materials	Addition of absorbents (slaked lime, quicklime, activated fly ash)	Wet or dry scrubber
CO_2	800–1040	Calcination process and fuel combustion	Reduce fuel energy use; use low-organic raw materials	Carbon capture or gas scrubbing system
CO	1–4	Incomplete combustion: organic matter in raw materials	Improve combustion efficiency; control raw material quality	Post-combustion oxidation system
Dust	0.01–0.4	Grinding and milling processes	Optimize plant layout; reduce fugitive dust sources	Electrostatic precipitators or fabric filters

Specifically, based on the mass balance calculated for this process, a total CO_2 emission of 54992 tonnes, which corresponded to 538 kg of CO_2/tonne of cement, was found. Comparison with literature values (800-1040 kg CO_2/tonne clinker[104]) pointed towards lower carbon emissions, which may be attributed to the fact that the composition of the fuel, namely coal, was not accounted as a reagent that led to the formation of carbon gases. For instance, the tax related to the Effective Carbon Rates (ECR) was found to be approximately 0.09€/CO_{2eq}[105], which would result in a total cost due to carbon gases of approximately 4949€. In comparison with other processes, this was relatively small, being around 1 tonne of carbon dioxide per tonne of clinker produced, which could be due to the employed assumptions.

Overall, the emissions of Greenhouse Gases (GHGs) and aerosols are projected to have a major impact on climate change over the upcoming decades. Therefore, the CO_2 produced in any plant has to be reduced as much as possible, either by capturing it or by using valorisation processes to reduce any emissions. Specifically, industrial processes are responsible for around 8% of the total carbon emissions, of which the cement sector accounts for half[106].

9.5 Bow-tie diagram

Radioactive waste poses a great danger to humans and to the environment. In order to systematically look at a portion of the risk posed by radioactive waste, a bow-tie diagram was made (see figure 26) where ionizing radioactivity of the vHLW was selected as the main hazard. Since the disposal facility is designed with a multi-barrier system, no single event should lead to the loss of containment of this radiotoxicity. However, failures affecting the integrity or shielding performance of the disposal package could increase the likelihood of radiation exposure before the radioactivity reaches acceptable radiation levels . Therefore, the top event was defined as the exposure of workers or equipment to ionizing radiation above allowable limits.

As a result, the main threats identified were related to events that could reduce the integrity or shielding performance of the disposal package, namely during the emplacement period or in the early stages of the disposal where the buffer is subjected to higher stresses, for which the corresponding control barriers were defined and presented. Similarly, the main consequences associated with the top event were identified to occur at the time of the incident or shortly thereafter when the hazard is being controlled. Hence, mitigation barriers were also defined in order to reduce the impact of radiation on workers and critical safety equipment.

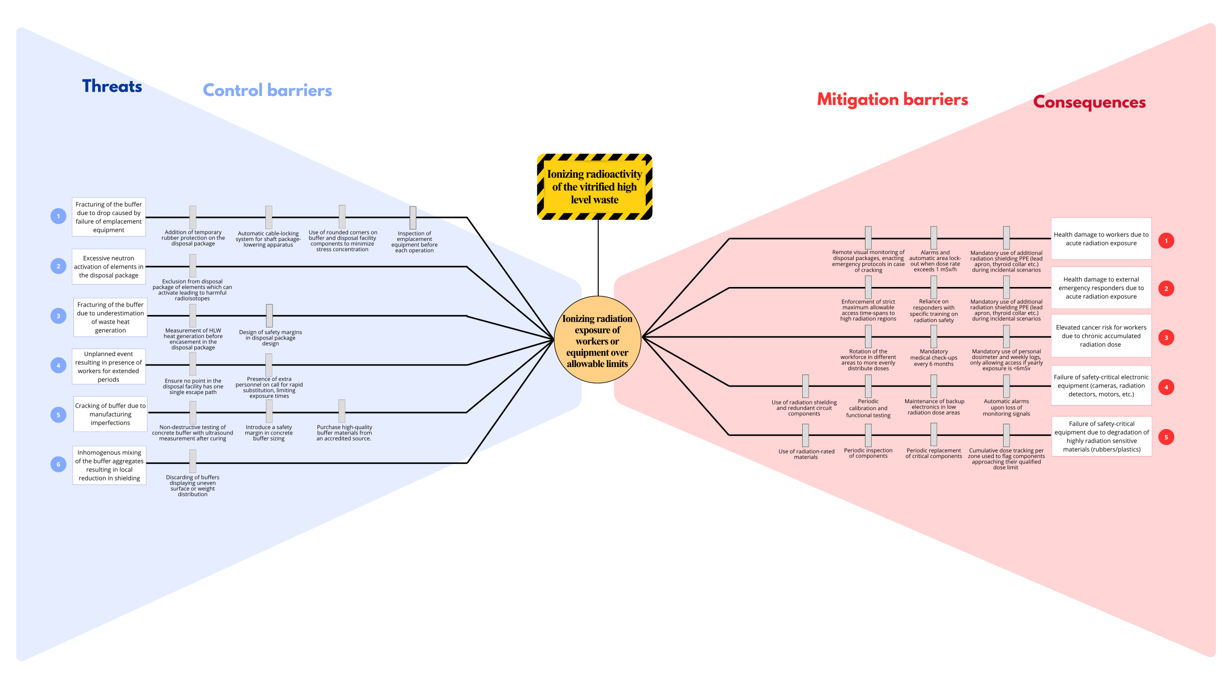

Figure 26: Bow-tie diagram.

10 Economic analysis

10.1 Financial margin assessment

As described in section 2.1 of this report, COVRA operates as a monopoly in the waste disposal market within the Netherlands. Additionally, producers of radioactive waste are legally obliged to bear the cost of proper disposal[107]. Since definitive disposal of waste is generally only allowed within the borders of the country in which it was generated[107], there is a legal obligation for radioactive waste producers to utilise COVRA's services, no matter the cost. Therefore, conventional market competition dynamics cannot be directly applied to estimate the financial margin of the proposed design, since the maximum disposal cost is not limited by market interest.

However, an estimate can be obtained using the profitability of the waste producers (nuclear power plants in the case of this project) as the limiting factor for product sale price. Since companies that produce HLW have to stay profitable in order to keep operating, a maximum allowable cost of the HLW disposal is calculated based on the profits achieved by these companies. The consequence of this is that COVRA will have an incentive to maintain prices below a certain limit, namely the following:

$$P/tVW < (I/tU - E/tU) \cdot R \tag{21}$$

Where P/tVW is the allowable price in euros per ton of vitrified waste, I/tU is the income and E/tU are the expenses incurred by the energy plant per ton of uranium, and R is the mass ratio between reactor HLW and processed vHLW. It must be noted that this calculation is only used to get an approximate value for the pricing, as it is difficult to use regular pricing calculations in this industry.

In this case, the income term is calculated on the basis of electricity costs and a fuel burn-up value of 50 GWd/tU, while expenses are derived indirectly from an estimated value of the levelised cost of electricity for nuclear power in the Netherlands, corresponding to 85.7 €/MWh[108] adjusted for inflation from 2020 to 2026. The value of R is 3.79 for a standard PUREX reprocessing procedure[109]. The end results are an income of 104.9 M€/tU and expenses of 102.8 M€/tU, leading to a maximum cost of 8 M€ per ton of waste (see appendix C for more detailed steps).

Given the average density of vHLW of 3.33 g/cm^3[109], and the storage volume per canister of 0.18 m^3, the stored mass per container is 599.4 kg, meaning the maximum cost for the disposal for one container is 4.8 M€. This figure will be taken as an approximate reference for the maximum allowable cost of the design.

It must be mentioned that even if the design cost were to be higher than this high-end limit, making it economically unviable, the Dutch government would still be legally compelled to subsidise the added disposal expenses[107]. The assumption being made here is that additional public expense in the nuclear programme would lead to stronger political pressure against it, which is considered to be an undesirable condition for COVRA's business model.

10.2 Disposal of vHLW

In the following steps, the costs of disposal for the proposed design are estimated. The aim is to express the overall cost of disposal for one container of vHLW as a function of its diameter. The impact of this design parameter on the mechanical and radiological properties of the disposal package was already assessed in chapter 4, on top of which its economic impact is additionally taken into consideration.

Tunnelling represents the most significant part of the costs, with width, depth, length and design (reinforcements and crossings) mainly dictating the pricing. COVRA's facility design is similar to the ANDRA-Cigéo project, which is placed 500 m underground in Callovo-Oxfordian claystone in France. Therefore, cost estimates from this project are used to estimate a price per m^3 of excavation. Specifically, the tunnel construction costs amounted to a value of approximately 5370 M€[110, 111], taking into account excavation, tunnel support, concrete lining, spoil management and temporary underground structural works. In this project the average excavated tunnel diameter corresponded to 5.5 m, a figure in line with what is expected for the COVRA operated facility, and a total tunnel length of 250 km[110]. Thus, the excavated volume is $\sim$5.9 Mm^3, and consequently, the total tunnelling cost per unit volume was found to be roughly equal to 904 €/m^3.

However, the ANDRA cost estimation does not take into account HVAC (Heating, Ventilation and Air Conditioning) systems, electrical infrastructure, fire safety systems, instrumentation and monitoring, reinforcement of the structure and connection reinforcements. Furthermore, Callovo-Oxfordian claystone is different from Paleogene clay, which the latter being more malleable, as well as the ANDRA site presenting slightly different conditions and parameters compared to COVRA's project. For this reason the estimated value was increased by a 20% safety margin, yielding a final estimate of 1085€/m^3.

At a depth of approximately 500 m[5], the facility must be able to accommodate a minimum of 8000 disposal packages, meaning that a single tunnel structure is not feasible. Instead, a multi-tunnel approach must be chosen with a central transportation tunnel and perpendicular disposal tunnels on its sides. For ease of cooling, ventilation, and later backfilling with foamed concrete, it is assumed that the tunnel length may not exceed 110 m, meaning that 39 containers, each with a length of 2.5 m, will be present, leaving a small space in between (roughly 3-4 cm) to allow for inspection, improved heat dissipation and added regions at the extremities of the tunnel for ease of manoeuvring (roughly 1 m with 39.5 extra at the back, 30 cm mid-way fill after 19 vHWL disposal packages, and 39.5 cm to seal the end of the tunnel).

This gives a maximum of approximately 22.6 km of disposal tunnel for 8034 vHWL disposal packages. Assuming a distance between tunnels of 50 m, the transport tunnel, with an additional extra 10% of space for operational manoeuvring and shaft connections, will be around 6.25 km in length. It is then assumed that disposal tunnels, transport tunnels and shafts will have a radius increase in diameter with respect to the disposal package as listed in table 21.

Table 21: Different tunnel type sizes as a function of disposal package diameter.

Buffer diameter (m)	**Disposal tunnel (m)**	**Transport tunnel (m)**	**Shaft tunnel (m)**
D	D+3	D+5	D+4

Total excavation volumes will therefore be expressed as a function of the disposal package diameter on the basis of the margins shown above. For clarity purposes, only results for a disposal package diameter of 2 metres will be shown here, however, the generalised expressions can be found in the appendix F.

The total tunnelling volume for 8034 containers with a buffer diameter of 2 metres is calculated to be 1.01 Mm^3. This is then converted into an expression of cost per container, multiplying by the tunnelling cost per unit volume and dividing by the number of containers, resulting on an estimate of 136 k€ per container.

Next, the production cost of each buffer container is estimated. Starting from the component costs summarised in table 22 a cost of $\sim$236€ per ton is found. To this estimate, the following margins are added: 12.5% for labour, 3.5% for maintenance and 2% for insurance and overhead costs. Additionally, a 5% increase in cost is assumed to take into account concrete additives such as plasticisers. The resulting cost is $\sim$290€ per ton.

Table 22: Raw material costs and mass fractions for magnetite based concrete (water is neglected).

Component	**Cost (€/ton)**	**Mass fraction**
Cement[112]	150	0.0704
Sand[113]	21.5	0.1554
Magnetite[114]	300	0.739

The volume of one disposal package can be expressed as a function of buffer outside diameter and converted into a cost per container using the previously calculated cost and a density of 3410 kg/m^3[14]. The resulting cost is approximately 6000 € per cast buffer.

The emplacement cost should also be proportional to the mass, but this dependence is for now neglected. The cost of an air cushion transport platform capable of holding the ∼60 ton weight of an emplacement container (under 3m in diameter) is assumed to be around 20k€. Considering a more specialised piece of equipment with adequate radiation shielding and container supports, this quote is increased by 50%, leading to a cost of 30k€. Assuming the use of ∼4 of these pieces of equipment during the total operating life of the disposal site, a total cost of 120 k€ is found.

Finally, backfill cost is related to the total tunnel volume and to a cost of foamed concrete of 59 €/m^3. This estimate includes margins for labour, maintenance and insurance (+18% in total +10% for pumping costs). The expression for total volume to be filled is obtained by subtracting the volume occupied by the containers from the equation for that of the tunnels. This results for D = 2 m in a backfilling cost of 7600 € per container.

In conclusion, the total cost of tunnelling, casting, emplacement and backfilling for a 2 m diameter buffer results in ∼150 k€ per HLW container. Considering the initially determined economic margin of 4.8 million € per vHLW container, it is possible to determine that enough financial margin exists to fully finance the project with payment from waste producers. Considering the potential volatility in the costs utilised during the above estimations, the application of a significant financing margin over the assessed total cost is suggested. This becomes especially important considering the large time interval occurring between acquisition of the waste by COVRA and completion of construction, emplacement and closure procedures.

10.2.1 Maximum allowable investment

Assuming a discount cash flow rate of return of 10%, the maximum allowable investment is found as the initial investment $I_{initial}$ that will lead to a net present value (NPV) of zero over the lifetime of the facility. Due to the monopolistic nature of COVRA's business model, an approximation is needed. One possible approach is to select a maximum profit margin of 50%, which fits comfortably in the margin estimated in part 10.1, then derive a yearly cash flow (CF), and from this estimate $I_{initial}$ as shown in equation 22, where $r_i = 0.1$ and $CF_n = \frac{150k€\cdot 8034}{144} \cdot 0.5 = 4.18$ million €. The end result is a maximum allowable initial investment of 46 M€.

$$I_{initial} = \sum_{1\to 144}^{n} \frac{CF_n}{(1+r_i)^{n-1}} \tag{22}$$

This investment is quite low, especially compared to the 3 billion EUR estimated in the COPERA CLAY report[5]. This can be attributed to the fact that COVRA does not operate like most companies do, having a much longer operating time. This leads to a much smaller cash flow, which in turn makes the maximum allowable investment smaller than it should be. Since the disposal of vHLW is not intended as a means to make profit, the calculated value should not be taken as a reasonable estimate.

10.3 Cement manufacturing plant

The economic assessment of the cement manufacturing plant is based on energy and materials inputs, as well as several pieces of process equipment. It is noteworthy that it was estimated that the total volume of cement required should be able to be produced within 9 days of continuous operation, showcasing that the plant has a capacity between 10 and 40 times lower than average sites (see Appendix C4)[74, 104]. The small amount of cement-based products required led to an unrealistic sizing of the plant. For this reason, literature magnitudes were used as reference in order to be able to employ equipment estimation equations.

The energy inputs required for the process were found to be approximately 3000 MJ/tonne of clinker[104], for which bituminous coal with a calorific value of 28472 MJ/tonne is commonly used in these operations[115]; and 110 kWh/tonne of cement of electricity[104]. In addition, the price of raw materials was approximately 5.03

€/tonne[116] and cement has currently attained a value of 150 €/tonne[112]. Finally, sizing of the equipment listed in table 23 was obtained from literature[75, 116] and purchase cost was calculated using Towler-Sinnott[88], Matche[117] for the cyclones, and the empirical equation C30 for the rotary kiln[116]. Computed values were updated from 2010, 2014, and 2023 to June 2024 by applying the corresponding correction factor[118], due to the lack of a recent Chemical Engineering Plant Cost Index.

Table 23: Principal plant's cost for manufacturing the total cement quantity.

		Purchase cost (M€)
Energy	Price	
Coal (€/tonne)	65.55[116]	0.67
Electricity (€/kWh)	0.0713	0.79
Materials	Price (€/tonne)	
Raw materials mix[116]	5.03	0.79
Cement[112]	150	15.33
Equipment	Size[75, 116]	
A-101 (tonne/h)	640	0.58
A-102 (tonne/h)	20	0.96
A-103 (tonne/h)	167.5	0.23
CR-101 (tonne/h)	500	1.70
D-101 (tonne/h)	2500	59.82
S-101 (m^3/h)	340000	0.31
S-102 (m^3/h)	244800	0.06
S-103 (m^3/h)	240000	0.24

As a result, the estimated capital expenditures (CAPEX) amounted to 63.9 M€, excluding alternative materials of construction, installation, and location. The operational expenditures (OPEX), based solely on raw materials and energy required to produce the total volume of cement, were estimated at 2.25 M€. Given the projected market value of the produced cement (15.33 M€), investing 63.9 M€ exclusively in equipment is not economically feasible; it would be more advantageous to procure the required materials from upstream suppliers. However, if the number of vHLW canisters to be disposed of were increased fivefold, on-site cement production could become relatively viable.

In addition to these calculations, the Bridgewater and Hill methods were employed to estimate the total capital investment required for the industrial plant (see appendix C.5). Results were found to be 332.30 M€ and 64.27 M€, showcasing a significant variation between the methodologies, which may be due to the different assumptions that each method is based on. Nonetheless, the former was indicated to be more consistent with the machinery estimates, as only the principal equipment purchase cost already add up to approximately 63.9 M€, without considering other factors such as land, contingency or Outside Battery Limits (OSBL) costs and material of construction, among others. This further supports the statement that construction of a cement manufacturing plant is unlikely to be economically feasible, since direct purchase of the cement is more cost-effective.

11 Creativity and Group Process Tools

In this section, a general overview of the creativity and group process tools is presented, with additional information provided in appendix G, as well as the planning followed during the project.

11.1 Creativity

As requested by the principal, this project exclusively uses demonstrated and well-studied technologies when elaborating the conceptual product. Furthermore, clay host repositories are less well developed than rock host repositories, and fewer demonstrated solutions are available. Creativity tools played a significant role in generating improvements upon these technological boundaries.

The main creativity method was brainstorming in specific scheduled meetings that were held throughout the concept stage to form and discuss new ideas for the project. In these meetings, the TRIZ method was also used to foment creativity. After that, the main concepts obtained were evaluated with methods explained in class (HoQ and Pugh matrix), and finally, they were presented to the supervisors to ensure that the group was going in the right direction.

Apart from the creativity method listed above, a different aspect also played a role in the project. The project as a whole did not align much with what was taught in previous courses (mainly product and process design), therefore, thinking outside the box was required to apply the knowledge that we did have to this project. The thermo-mechanical modelling was especially difficult, since no courses in the chemical engineering curriculum cover this type of work. This part of the project required a lot of work in forming a basic understanding of mechanical modelling, and further extend it into building a set of COMSOL models that describe the system.

11.2 Group tools

Multiple tools were used to facilitate communication, task distribution, and working efficiency, aspects the team identified as critical given prior challenges in group work. The main tool was the use of meetings throughout the duration of the project with members of the group, as well as sessions with the group coach, the supervisor and the technical advisor. These meetings improved task distribution and working efficiency, as well as an overall better understanding of COVRA's objectives.

12 Conclusion and recommendations

The use of radionuclides is essential in power generation, healthcare and research, however, this use inherently results in the formation of a waste stream. A small part of this waste is highly radioactive and long-lived and, therefore, requires specialised disposal facilities to shield future generations from the radiotoxicity of the waste. In this report, the disposal of vitrified high-level waste in underground facilities located in Paleogene clay layers was explored. This case was provided by COVRA, the Dutch central organisation for radioactive waste. The design considerations for such disposal facilities were explored, including a market and value chain analysis. A set of technical requirements was formed based on the customer needs. Designs for the disposal package are explored as the main deliverable. Additionally, the emplacement system and backfill were also supported to better assess the system as a whole. Based on the technical requirements, a number of concepts for each of the aforementioned aspects were chosen and investigated further. These designs were subsequently judged based on a set of criteria acquired using a house of quality. From this, a final concept for each was selected.

This yielded the following concepts: A disposal package comprised of a carbon steel overpack containing the waste canister, with a magnetite aggregate concrete for the buffer, which was chosen for its high radiation shielding. The emplacement vehicle chosen was an air-cushion drum loader, which is compact and has adequate loading capacity. Foamed concrete was chosen as backfill for its high flowability.

The disposal package has a number of requirements it should adhere to: It has to be able to withstand water ingress over a period of 1200 years. To assess this properly, the backfill material also has to be selected. It should be able to withstand thermo-mechanical stress caused by the heat generation of the waste. Lastly, it should provide adequate shielding for nearby workers in order not to exceed an additional dose rate of 6 mSv per year.

The first aspect was explored by investigating diffusion and corrosion behaviour in the disposal package. Here, carbonation and chloride induced corrosion was studied, as well as passive state corrosion. On the one hand, during the first ten years after emplacement, contact with CO_2 from air (430 ppm) was found to only reach a depth of maximum 3 mm, which is negligible based on the rebar location at a distance of 35 mm from the outer surface. On the other hand, chloride diffusion from clay pore water was investigated in three different salinity scenarios (134, 541 and 2270 mmol/kg). Nevertheless, in neither of them concentrations were determined to be higher than 1 wt% at the rebar depth, this being a commonly considered threshold under anoxic conditions. It was found that none of these play a significant role in the corrosion of the overpack or rebar, ensuring that no pore water will contact the waste form within the 1200 years. These findings could indicate that the use of rebar is feasible in the disposal package, however, the limited set of corrosion mechanisms explored, together with the lack of literature covering rebar reinforced concrete in underground conditions for a long time span, led to the decision of excluding the reinforcements.

The mechanical stability of the disposal package was investigated using multiple models in COMSOL. Both thermo-mechanical and impact-induced stresses were explored, using a combination of transient and steady-state simulations. Initially, a buffer radius of 1 m, and a length of 2.5 m was assumed for these simulations. It was found that the external temperature of the vHLW canister was the limiting factor for storage times, as high temperatures will lead to degradation of the concrete buffer due to the evaporation of water. This resulted in a minimal storage time of 50 years. The temperature evolution of the overpack surfaces was further investigated, to judge whether this could be a problem when casting the last part of the buffer. After placing the vHLW into the buffer, the temperatures decrease significantly since the buffer acts as a heat sink. This results in a time window during which the top surface of the overpack is cool enough to allow for curing. This does further limit the storage time to a minimum of 80 years.

The thermo-mechanical stresses were analysed for the disposal package standing upright with different thermal powers, corresponding to different storage times. Here, it was found that storage times of 70 years and less will result in a circumferential tensile stress on the outer part of the buffer that is higher than the tensile strength of the concrete, which would result in the failure of the buffer. This means that also for the thermo-mechanical aspect, a minimum storage time of 80 years is required.

For the impact stresses, a drop of both 20 and 2 cm was simulated, using a transient model. Here, it was found that the tensile forces caused by the drop far exceed the tensile strength of the concrete and would cause significant cracking within the buffer. From this it can be concluded that impacts should be prevented at all cost. It is important to note, however, that the buffer is not the sole containment barrier, as the carbon-steel overpack could still remain intact under such an impact. Nonetheless, buffer cracking compromises a safety barrier and reduces shielding against radiation. This is one of the major weaknesses in the design, and this aspect could be investigated further to see if a change in design could lead to a more impact-resistant disposal package.

Since ensuring the safety of workers during the active phase of the disposal facility is one of the core functions of the disposal package, its radiation shielding properties were assessed. High-energy gamma radiation, mostly emitted by the decay of ^{137}Cs, was identified as the only type of ionising radiation presenting sufficient activity and penetration depth to induce significant exposure rates. The high complexity of neutron shielding assessment was recognised, and a more detailed estimation in this respect is recommended for future developments.

The shielding properties of the disposal package were estimated numerically with a ray-tracing-like algorithm. This allowed for the simultaneous evaluation of the effects of both distance and shielding for all portions of the HLW. The results indicate that a disposal package radius of 0.9 m or higher will provide adequate shielding, considering the maximum yearly radiation dose of 6 mSv set by COVRA company policy. Longer pre-emplacement storage times were found to lower dose rates less sharply than this design variable. The inclusion of magnetite aggregates in the concrete buffer, was also found to improve shielding effectiveness by several orders of magnitude compared to common concrete mixes used in construction, supporting the choice of its implementation in this design. Through sensitivity analysis, limitations in available computational power were determined to have induced non-negligible uncertainties in the results presented. For this reason it is suggested to repeat the presented estimations with finer discretisation grids for better accuracy.

The potential impact of accidents leading to a weakening of the containment function of the disposal package with respect to ionising radiation was also assessed. This step is to be considered as paired with the bow-tie analysis carried out in the HSE chapter. The obtained results indicate that the disposal package is resilient to minor damage (surface chipping, thin cracking), suggesting it represents a very reliable safety layer for workers from radiation exposure. In contrast, a more severe rupture of the buffer was found to cause severe radiation exposure rates for nearby personnel. This highlights the necessity of careful inspection, maintenance and handling of the containers during and after emplacement.

An optimisation of buffer size versus storage time was performed, in which both the thermo-mechanical stress and radiation doses to workers were evaluated to judge the feasibility of the design. Buffer radii of 1.1, 1.0, 0.9, 0.8 and 0.7 m were investigated for storage times ranging from 50 to 130 years in steps of 10 years. For storage times of 80 years and less, the thermo-mechanical stress was found to be too large. This, combined with the aforementioned limitations imposed by radiation exposure rates, points to an optimal storage time and radius of 90 years and 0.9 m, respectively.

Moreover, the production of the disposal package was assessed starting from the manufacturing of cement as principal raw material to the final assembly of the product in question. On the one hand, a cement plant was designed to yield the desired amount of material, including the corresponding block diagrams, PFD and P&ID, that would be further used in the formulation of the buffer (high density concrete with magnetite aggregates) and backfill (low density foamed concrete). Estimations of the plant's cost were performed via the Bridgewater and Hill method, resulting in a total permanent investment of 332.30 and 64.27 M€, respectively, showcasing that direct purchase of cement (15.33 M€) would be far more logical. In addition, the carbon steel overpack welding, buffer casting, emplacement and backfilling processes were also investigated. Applicable process control and quality control methodologies were studied to attain a standards-compliant product. An equipment list with the principal process-relevant machinery was made with their respective dimensions.

With regard to the underground heat utility requirements, a plug-flow model was applied to identify the cooling needed in the disposal tunnels to moderate heat generation from the disposal packages, having set a maximum tunnel-air temperature of 28°C. Ventilation ducts with diameters of 0.27, 0.38 and 0.47 m for heat fluxes of 200, 400 and 600 W, respectively, were found to be needed. As a result, the power needed for active air cooling when the external air reaches temperatures over 15°C, was found to be between 400 and 1200 kW depending on the scenario, which yielded an equipment cost for cooling in the range of 2.66-7.04 M€. However, this is only considering the disposal tunnels and not the transport tunnel, which would also require additional cooling.

The HSE and sustainability of several critical processes were assessed via an LCA, HAZOP, and bow-tie methodology. On the one hand, by employing a *cradle-to-grave* approach, the environmental footprint per FU (1 disposal package of vHLW emplaced in the geological disposal facility) was found to be approximately 34 tons of CO_2 equivalences. Several alternative scenarios were explored to identify the key contributors to the total emission of carbon gases, which led to the conclusion that optimisation of the magnetite content in the buffer material would improve the environmental impact if satisfactory shielding can be attained with a reduced amount of magnetite. Moreover, the HAZOP analysed several nodes related to the overpack manufacturing, concrete mixing, buffer casting and emplacement process, where consequences due to deviations from critical parameters were studied. Finally, the hazard of ionising radiation emitted by the vHLW was explored using a bow-tie diagram, with a focus on the exposure of workers and equipment over the allowable limit. Several threats were identified, for which a number of control barriers were suggested. Several consequences were also explored, for which a set of mitigation barriers was identified.

A preliminary economic assessment was carried out to express total disposal costs per container as a function of disposal package radius. The results indicate that the main source of costs will be digging and construction of the disposal facility tunnels. The total cost was estimated to be $\sim$ 140 k€ per HLW container, for a radius of 0.9 m. This finding, although approximate, indicates a significant margin is present to invest in research and development with the aim of optimising the containment properties of the multi-barrier disposal system.

Although several aspects of the disposal package were explored in detail, there are limitations to this work. For the corrosion analysis, a limited set of possible corrosion mechanisms was explored. Carbonation, chloride, and passive state corrosion were each found not to play a significant role over the 1200 year period, which suggested that a rebar reinforced buffer could be feasible. This was not considered sufficient to apply it to the concept, as the data and literature rest on a limited set of studied mechanisms and no long-term experimental validation of reinforced concrete corrosion under these conditions, which does not meet the standard of demonstrated reliability required for a safety critical, irreversible disposal package. Reinforcement was therefore excluded in favour of the less corrosion exposed carbon steel overpack.

To obtain a more holistic view of the corrosion, more mechanisms should be assessed, including the effect of water consumption caused by the corrosion reactions, and real-life experiments would have to be conducted to validate the calculations. The effect of including rebar is consequently recommended as a priority for future work, as it could mean that the overpack can be excluded from the disposal package. The use of different types of reinforcement, such as basalt fibres in combination with a high density aggregate such as magnetite, could also be investigated, as suggested earlier in the report. This would combine the mechanical stability of basalt-fibre-reinforced concrete with the shielding properties of magnetite.

Further mechanical studies could also prove valuable. In this study, no coupled thermo-mechanical and impact studies were performed, as these models are very complex. However, these will give a more accurate approximation of the stresses in the disposal package. Additionally, more impact scenarios could be investigated, as the drop simulations represent an extreme case. This could include two disposal packages colliding during emplacement or having another vehicle hit a disposal package.

References

[1] Ewoud Verhoef Elise Burggraaff Jeroen Welbergen. *Nationale Radioactief Afval Inventarisatie.* COVRA, 2022.

[2] R. Parrish and A. Aitkaliyeva. “A review of microstructural features in fast reactor mixed oxide fuels”. In: *Journal of Nuclear Materials* 510 (Nov. 2018), pp. 644–660.

[3] A. Goel et al. “Challenges with vitrification of Hanford High-Level Waste (HLW) to borosilicate glass – An overview”. In: *Journal of Non-Crystalline Solids: X* 4 (2019), p. 100033.

[4] Bernard Grambow. *Vitrified High-Level Waste (HLW).* Domain Insight 3.1.2. European Joint Programme on Radioactive Waste Management (EURAD), July 2023.

[5] COVRA. *COPERA Clay 2024 Summary.* Report. COVRA (Central Organisation for Radioactive Waste), 2025.

[6] OECD, NEA. *Nuclear Legislation in OECD and NEA Countries: Regulatory and Institutional Framework for Nuclear Activities, Netherlands.* Report. OECD (Organisation for Economic Co-operation and Development), 2025.

[7] Patrik Sellin and Olivier X. Leupin. “The Use of Clay as an Engineered Barrier in Radioactive-Waste Management a Review”. In: *Clays and Clay Minerals 2013 61:6* 61 (6 Dec. 2013), pp. 477–498. ISSN: 1552-8367.

[8] Lyesse Laloui, Alessio Ferrari, and Jose A. Bosch. “Bentonite clay barriers in nuclear waste repositories”. In: *E3S Web of Conferences* 205 (Nov. 2020). ISSN: 22671242.

[9] Dong Hwa Noh et al. “Bentonite as an engineered barrier material for nuclear waste repository - Geotechnical perspectives, key properties, knowledge gaps, and opportunities”. In: *Nuclear Engineering and Technology* 57 (10 Oct. 2025), p. 103700. ISSN: 1738-5733.

[10] Ebru Gedik and Adem Atmaca. “An experimental study investigating the effects of bentonite clay on mechanical and thermal properties of concrete”. In: *Construction and Building Materials* 383 (2023), p. 131279. ISSN: 0950-0618.

[11] “Investigating the performance of magnetite powder-bentonite mixtures for radiation shielding and gas permeability in wet-dry cycles”. In: *Results in Engineering* 28 (Dec. 2025), p. 107573. ISSN: 2590-1230.

[12] “Progress in bentonite clay modification and enhancing properties to industrial applications: A review”. In: *Materials Chemistry and Physics* 337 (June 2025), p. 130486. ISSN: 0254-0584.

[13] “Radiation shielding properties of concrete containing magnetite”. In: *Progress in Nuclear Energy* 137 (July 2021), p. 103776. ISSN: 0149-1970.

[14] Roman Jaskulski, Krzysztof Liszka, and Daria Jóźwiak-Niedźwiedzka. “Multifaceted Analysis of the Thermal Properties of Shielding Cement-Based Composites with Magnetite Aggregate”. In: *Materials* 17 (12 June 2024), p. 2936. ISSN: 19961944.

[15] Farhad Aslani, D. M. Lesslie, and F. Hamidi. “Development and analysis of highly workable high-strength heavyweight concrete using magnetite aggregates”. In: *Structural Concrete* 22.S1 (2021), E169–E182.

[16] Baoming Ding, Lei Zhang, and Jiaqi Liu. “Study on Shielding and Radiation Resistance of Basalt Fiber to Gamma Ray”. In: *Materials* 15 (7 Apr. 2022), p. 2522. ISSN: 19961944.

[17] Great S. Anunike, Mohamad Tarabin, and Ousmane A. Hisseine. “Ultra-high-performance concrete for nuclear applications: A review of raw materials and mix design approaches”. In: *Construction and Building Materials* 438 (Aug. 2024), p. 136938. ISSN: 0950-0618.

[18] Abdullah M. Zeyad et al. “Effect of aggregate and fibre types on ultra-high-performance concrete designed for radiation shielding”. In: *Journal of Building Engineering* 58 (Oct. 2022), p. 104960. ISSN: 2352-7102.

[19] Maryna Holiuk et al. “Basalt-boron fiber reinforced concrete: A sustainable solution for neutron radiation shielding”. In: *Nuclear Engineering and Design* 440 (Aug. 2025), p. 114150. ISSN: 0029-5493.

[20] Iryna Romanenko et al. “New composite material based on heavy concrete reinforced by basalt-boron fiber for radioactive waste management”. In: *EPJ Nuclear Sciences & Technologies* 5 (2019), p. 22. ISSN: 2491-9292.

[21] Hamza Jamshaid and Rupesh Mishra. “A green material from rock: basalt fibre – a review”. In: *The Journal of The Textile Institute* 107.7 (2016), pp. 923–937.

[22] Arun Singh Chahar and Priyaranjan Pal. “Study on various properties of reinforced concrete – A review”. In: *Materials Today: Proceedings* 65 (2022). International Conference on Advances in Construction Materials and Structures, pp. 597–602. ISSN: 2214-7853.

[23] G.S. Duffó et al. “Durability of a reinforced concrete designed for the construction of an intermediate-level radioactive waste disposal facility”. In: *Journal of Nuclear Materials* 420.1 (2012), pp. 382–387. ISSN: 0022-3115.

[24] HUBTEX. *Handling solutions for drums, spools, bobbins — HUBTEX.*

[25] Nagra. *Kristallin I: Safety Assessment Report.* Nagra Technical Report NTB 93-22E. Wettingen, Switzerland: National Cooperative for the Disposal of Radioactive Waste (Nagra), 1994.

[26] M. Laviña et al. “Long-term Evolution of Bentonite-Based Seals for Closure of a Radioactive Waste Repository in Claystone: A Hydro-Chemo-Mechanical Modelling Assessment”. In: *Transport in Porous Media* 151 (2024), pp. 287–317.

[27] Rohini C. Kale, Bhanwariwal Kapil, and K. Ravi. “Response of compacted bentonite to hyperalkalinity and thermal history”. In: *Scientific Reports* 11 (2021), p. 15483.

[28] P. Sellin et al. *Initial State-of-the-Art on Hydraulic Mechanical Chemical Evolution of Bentonite for Barriers Optimisation.* Deliverable D10.1. Final version as of 31.03.2025, EC Grant Agreement No. 101166718. European Partnership on Radioactive Waste Management-2 (EURAD-2), Mar. 2025.

[29] C. L. Zhang et al. *Geotechnical Properties and Barrier Performance of Claystone/Bentonite Mixtures for Radioactive Waste Repositories.* GRS-703. GRS, 2023.

[30] *OPERA-PG-COV020.* Tech. rep. Technical report on moisture transport and concrete properties in radioactive waste management systems. COVRA / OPERA Programme, unknown.

[31] Hongyuan Zhou et al. “Improving energy absorption capacity of foam concrete with gradient and layered architecture”. In: *Construction and Building Materials* 319 (2022), p. 126140.

[32] Agboola Shamsudeen Abdulazeez and Adamu Abubakar Sani. “Properties of foam concrete: A review”. In: *Discover Concrete and Cement* 2.1 (2026), p. 4.

[33] A. M. Sycheva et al. “Refractory Foam Concrete for Nuclear Power Engineering”. In: *Refractories and Industrial Ceramics* 64.1 (2023), pp. 38–45.

[34] Y.H. Mugahed Amran, Nima Farzadnia, and A.A. Abang Ali. “Properties and applications of foamed concrete; a review”. In: *Construction and Building Materials* 101 (2015), pp. 990–1005. ISSN: 0950-0618.

[35] A. Dauzères, O. Helson, S. Churakov, et al. *Initial State of the Art on the Chemo-Mechanical Evolution of Cementitious Materials in Disposal Conditions.* Deliverable D16.1. EURAD, 2022.

[36] Y. Zhao and W. Jin. “Steel Corrosion in Concrete”. In: *Steel Corrosion-Induced Concrete Cracking.* 2016, pp. 19–29.

[37] S. Ahmad. “Reinforcement corrosion in concrete structures, its monitoring and service life prediction–a review”. In: *Cement and Concrete Composites* 25.4–5 (May 2003), pp. 459–471.

[38] Y. Li and W. Ye. “Advances in Gas Breakthrough of Buffer/Backfill Materials in High-Level Radioactive Waste Geological Repository”. In: *Proceedings of ACEER 2024*. Vol. 575. Lecture Notes in Civil Engineering. Review of gas breakthrough mechanisms in bentonite buffer/backfill materials and hydrogen generation from metallic corrosion in deep geological repositories. Springer, 2025, pp. 409–421.

[39] N. R. Smart et al. *ConCorD Synthesis Report.* Deliverable D15.14 D15.14. Reports long-term anaerobic steel corrosion behaviour, corrosion-product evolution, and hydrogen generation under disposal conditions. EURAD – European Joint Programme on Radioactive Waste Management, May 2024.

[40] R. E. Melchers. “Microbiological and abiotic processes in modelling longer-term marine corrosion of steel”. In: *Bioelectrochemistry* 97 (June 2014), pp. 89–96.

[41] Milton Ohring and Lucian Kasprzak. “Environmental Damage to Electronic Products”. In: *Reliability and Failure of Electronic Materials and Devices.* 1998, pp. 359–410.

[42] Baowei Ma, John L. Provis, Di Wang, et al. “The Essential Role of Cement-Based Materials in a Radioactive Waste Repository”. In: *npj Materials Sustainability* 2 (2024), p. 21.

[43] Wenyao Li et al. “The Role of Hydrogen in the Corrosion and Cracking of Steels - A Review”. In: *Corrosion Communications* 4 (2022), pp. 23–32.

[44] G. S. Duffó et al. “Durability of a Reinforced Concrete Designed for the Construction of an Intermediate-Level Radioactive Waste Disposal Facility”. In: *Journal of Nuclear Materials* 420.1–3 (2012), pp. 382–387.

[45] Santiago Guzmán, Jaime C. Gálvez, and José M. Sancho. “Cover Cracking of Reinforced Concrete Due to Rebar Corrosion Induced by Chloride Penetration”. In: *Proceedings of the 8th International Conference on Fracture Mechanics of Concrete and Concrete Structures (FraMCoS-8).* 2013.

[46] V. L’Hostis, F. Foct, and P. Dillmann. “Characterization of the Corrosion of Reinforcing Steel and Consequences for Concrete Cracking in Long-Term Nuclear Waste Applications”. In: *Journal of Nuclear Materials* 379.1–3 (2008), pp. 124–132.

[47] X. Wang et al. “A Review of Concrete Carbonation Depth Evaluation Models”. In: *Coatings* 14.4 (Apr. 2024), p. 386.

[48] P. Saura Gómez et al. “Carbonation-Induced Corrosion of Reinforced Concrete Elements according to Their Positions in the Buildings”. In: *Corrosion and Materials Degradation* 4.3 (Sept. 2023), pp. 345–363.

[49] Jessica Forsdyke and Janet Lees. “Carbonation behaviour of concrete exposed to natural and accelerated carbonation conditions”. In: *unpublished* (2022).

[50] Wei-bin Yuan et al. “Comparative analysis of time-dependent CO2 uptake in cement and geopolymer concretes via diffusion-induced carbonation”. In: *Case Studies in Construction Materials* 22 (2025), e04573.

[51] J. Griffioen, H. Verweij, and R. Stuurman. “The Composition of Groundwater in Palaeogene and Older Formations in the Netherlands: A Synthesis”. In: *Netherlands Journal of Geosciences* 95.3 (June 2016), pp. 349–372.

[52] K. Y. Ann, J. H. Ahn, and J. S. Ryou. “The importance of chloride content at the concrete surface in assessing the time to corrosion of steel in concrete structures”. In: *Construction and Building Materials* 23.1 (Jan. 2009), pp. 239–245.

[53] J. M. Aldred, B. V. Rangan, and N. R. Buenfeld. “Effect of initial moisture content on wick action through concrete”. In: *Cement and Concrete Research* 34.6 (June 2004), pp. 907–912.

[54] G. K. Glass and N. R. Buenfeld. “The influence of chloride binding on the chloride induced corrosion risk in reinforced concrete”. In: *Corrosion Science* 42.2 (Feb. 2000), pp. 329–344.

[55] R. K. Dhir, M. A. K. El-Mohr, and T. D. Dyer. “Developing chloride resisting concrete using PFA”. In: *Cement and Concrete Research* 27.11 (May 1998), pp. 1633–1639.

[56] John P. Broomfield. *Corrosion of Steel in Concrete: Understanding, Investigation and Repair.* 2nd ed. London: Taylor & Francis, 2006, p. 296. ISBN: 9780415334044.

[57] F. Khoshnaw and R. Gubner. “Part I: General Aspects of Corrosion, Corrosion Control, and Corrosion Prevention”. In: *Corrosion Atlas Case Studies.* Elsevier, Jan. 2020, pp. xxv–xli.

[58] Mesfer Mohammad Khaled et al. “Chloride diffusion models for plain and blended cement concretes exposed to laboratory and atmospheric marine conditions”. In: *Journal of Materials Research and Technology* 17 (Mar. 2022), pp. 125–138.

[59] Yong Zhang, Mingzhong Zhang, and Guang Ye. “Influence of moisture condition on chloride diffusion in partially saturated ordinary Portland cement mortar”. In: *Materials and Structures* 51.2 (2018), p. 36.

[60] C. Coll et al. “Characterizing in the laboratory permeability changes induced by deviatoric stress in clayey rocks”. In: *Geo-Engineering Book Series.* Elsevier, 2004, pp. 547–552.

[61] M. Stefanoni, U. M. Angst, and B. Elsener. “Corrosion rate of carbon steel in carbonated concrete – A critical review”. In: *Cement and Concrete Research* 103 (2018), pp. 35–48.

[62] M. Kaneko et al. *Evaluation of Gas Generation Rate by Metal Corrosion in the Reducing Environment.* Tech. rep. RWMC-TRE-03003. Tokyo, Japan: Radioactive Waste Management Funding and Research Center (RWMC), 2004.

[63] J. Mibus et al. *Chemical Evolution of ILW and HLW Disposal Cells.* Tech. rep. D2.18. EURAD Work Package 2: Chemical Evolution of Radioactive Waste Disposal. EURAD, 2018.

[64] European Committee for Standardization. *Eurocode 2: Design of Concrete Structures – Part 1-1: General Rules and Rules for Buildings.* Brussels, Belgium: CEN, 2004.

[65] Engineering ToolBox. *Linear Thermal Expansion Coefficients of Materials.* Available at: https://www.engineeringtoolbox
expansion-coefficients-d$_9 5.html(accessed 2026 - 06 - 17)$. n.d.

[66] A. Aloy et al. “Radiation Characteristics of Borosilicate Glass Containing High-Level Waste”. In: *Radioactive Waste* 12 (Jan. 2020), pp. 93–100.

[67] International Atomic Energy Agency. *Live Chart of Nuclides.* `https://nds.iaea.org/relnsd/vcharthtml/VChartHTML.html`. 2026.

[68] James E. Turner. *Atoms, Radiation, and Radiation Protection.* 3rd ed. Weinheim, Germany: Wiley-VCH Verlag GmbH & Co. KGaA, 2007. ISBN: 9783527406067.

[69] M. J. Berger et al. *XCOM: Photon Cross Sections Database.* NIST Standard Reference Database 8 (XGAM). Accessed: 2026-06-17. Gaithersburg, MD, USA, 2010.

[70] Pew Basu, R. Sarangapani, and B. Venkatraman. “Gamma ray buildup factors for conventional shielding materials and buildup factors computed for tungsten with a thickness beyond 40 mean free paths”. In: *Applied Radiation and Isotopes* 154 (2019), p. 108864. ISSN: 0969-8043.

[71] D. K. Trubey. “Gamma-Ray Buildup Factor Coefficients for Concrete and other Materials”. In: *Nuclear Applications and Technology* 9.3 (1970), pp. 439–441.

[72] Naoto Aizawa et al. “Development of radiation characteristics analysis code system for geological disposal and application to vitrified waste disposal with various LWR burnup conditions”. In: *Annals of Nuclear Energy* 167 (2022), p. 108761. ISSN: 0306-4549.

[73] b M. F. Ashby a and Michael Smidman. *Materials for Nuclear Power Systems - Granta Design.* Engineering Department, Cambridge University, UK, 2010.

[74] Anjan Kumar Chatterjee. *Cement Production Technology: Principles and Practice.* CRC Press, 2020.

[75] T. Gao et al. “Analysis of material flow and consumption in cement production process”. In: *Journal of Cleaner Production* 112 (Jan. 2016), pp. 553–565.

[76] J.-L. Galvez-Martos and H. Schoenberger. “An analysis of the use of life cycle assessment for waste co-incineration in cement kilns”. In: *Resources, Conservation and Recycling* 86 (May 2014), pp. 118–131.

[77] P. del Strother. “Manufacture of Portland Cement”. In: *Lea’s Chemistry of Cement and Concrete.* Ed. by Peter C. Hewlett and Martin Liska. Butterworth-Heinemann, 2019, pp. 31–56.

[78] H. I. Khafajah, M. M. Abdelsamie, and M. I. H. Ali. “Thermoeconomic assessment of a cement-plant waste-heat-driven trigeneration system for power, cooling, and desalination”. In: *Energy Nexus* 21 (Mar. 2026), p. 100631.

[79] *EN 206: Concrete — Specification, performance, production and conformity.* European Standard. Brussels: CEN.

[80] *EN 13670: Execution of concrete structures.* European Standard. Brussels: CEN.

[81] Jr. Sanders W. W. and W. H. Munse. “Study of Inspection Methods and Quality Control for Welded Highway Structures”. In: *Highway Research Record.* 110. Highway Research Board, 1966, pp. 22–35.

[82] American Welding Society. *Welding Inspection Handbook (WIH).* 4th. American Welding Society, 2015. ISBN: 978-0-87171-855-6.

[83] P. Kah et al. “Real Time Non-Destructive Testing Methods of Welding”. In: *Advanced Materials Research* 933 (2014), pp. 109–116.

[84] A. N. Shankar et al. “Physical and mechanical properties of foamed concrete, a literature review”. In: *Materials Today: Proceedings* (2023).

[85] Malcolm J. McPherson. *Subsurface Ventilation and Environmental Engineering.* London: Chapman & Hall, 1993. ISBN: 9780412353000.

[86] PurpleAir. *PurpleAir Real-Time Air Quality Map: Netherlands Estimated Absolute Humidity.* 2026. URL: `https://map.purpleair.com/environment-estimated-absolute-humidity/netherlands?opt=%2F1%2Flp%2Fa10%2Fp604800%2FcC0&select=21947#6.46/52.027/5.672` (visited on 06/08/2026).

[87] *Cost estimate for disposal of waste in clay host rock in the Netherlands.* Tech. rep. Price level 2022. COVRA, 2022.

[88] Gavin P. Towler and Ray K. Sinnott. *Chemical Engineering Design: Principles, Practice and Economics of Plant and Process Design.* Amsterdam; Boston: Elsevier/Butterworth-Heinemann, 2008.

[89] PROTEM Group. *Twin Shaft Concrete Mixers.* n.d. URL: `https://www.protemgroup.com/en/solutions/ready-mix-precast/plant-equipment-and-spare-parts/twin-shaft-concrete-mixers.html` (visited on 06/03/2026).

[90] A. Author. *Concrete hopper.* Accessed: June 15, 2026. 2023.

[91] Grainger. *Welding Equipment and Supplies.* Accessed: June 15, 2026. 2026.

[92] YG Machinery. *Concrete Pump.* Accessed: June 15, 2026. 2024.

[93] FADA Engineering. *Cable Drum & Reel Transporter (CRT).* 2024. URL: `https://www.fadaglobal.com/category/cable-drum-and-reel-transporter/` (visited on 06/03/2026).

[94] Supply House. *Z-FLEX 12 x 10 Ft Triple-Lock Aluminum Flex Duct.* Accessed: June 15, 2026. 2024.

[95] SODECA. *Extraction Ventilation Systems: HCT IMP C.* Accessed: June 15, 2026. 2024.

[96] Saxon Drilling. *Rig Equipment: Hoisting Equipment.* Accessed: June 15, 2026. 2024.

[97] Akkerman. *Tunnel Boring Machines.* Accessed: June 15, 2026. 2024.

[98] YG Machinery. *Concrete Pump.* n.d. URL: `https://www.ygmachinerycn.com/ConcretePump.html` (visited on 06/03/2026).

[99] D. Aydın and M. Ayhan. "Impact of TBM operational parameters on specific energy across geological formations in the Silvan tunnel project". In: *Results in Engineering* 30 (June 2026), p. 110498.

[100] ecoinvent Association. *Home.* `https://ecoinvent.org/`. Accessed: 2026-06-10. 2026.

[101] Sustainability Impact Metrics. *Data, Tools, Books.* `https://www.ecocostsvalue.com/data-tools-books/`. Accessed: 2023-05-03. 2023.

[102] David Edwards et al. "Inherent Safety: It's Common Sense, Now for Common Practice". In: *IChemE Symposium Series No. 25 (Hazards 25).* Institution of Chemical Engineers (IChemE). Edinburgh, UK, May 2015.

[103] E.-D. Mostafa. "Cement Industry - Optimization, Characterization and Sustainable Application". In: *Cement Industry - Optimization, Characterization and Sustainable Application.* IntechOpen, 2020.

[104] European Commission. *Integrated Pollution Prevention and Control (IPPC): Reference Document on Best Available Techniques in the Cement and Lime Manufacturing Industries.* Tech. rep. Seville, Spain: European IPPC Bureau, Dec. 2001.

[105] A. Mengden and Andrea M. Nieder. "Carbon Taxes in Europe". In: *Tax Foundation* (July 2025). Accessed: 2026-05-12.

[106] Mikalai Filonchyk et al. "Greenhouse gases emissions and global climate change: Examining the influence of CO2, CH4, and N2O". In: *Science of The Total Environment* 935 (2024), p. 173359.

[107] EURATOM. *COUNCIL DIRECTIVE 2011/70/EURATOM: establishing a Community framework for the responsible and safe management of spent fuel and radioactive waste.* Report. 19 July 2011.

[108] ENCO. *Possible role of nuclear in the Dutch energy mix in the future.* Ministry of Economic Affairs and Climate Policy, 2020.

[109] Alistair F. Holdsworth, Edmund Ireland, and Harry Eccles. "Spent Nuclear Fuel—Waste to Resource, Part 1: Effects of Post-Reactor Cooling Time and Novel Partitioning Strategies in Advanced Reprocessing on Highly Active Waste Volumes in Gen III(+) UOx Fuel Systems". In: *Journal of Nuclear Engineering* 6.3 (2025). ISSN: 2673-4362.

[110] ANDRA. *Pièce 7 : Chiffrage des coûts d'investissement des liaisons surface-fond et des ouvrages souterrains (SS4).* Consulté en 2026. Agence nationale pour la gestion des déchets radioactifs, 2025.

[111] Y. Wileveau and F. Bernier. "Similarities in the hydromechanical response of Callovo-Oxfordian clay and Boom Clay during gallery excavation". In: *Physics and Chemistry of the Earth, Parts A/B/C* 33 (2008), S343–S349.

[112] *Market Research Report: Cement; Portland, Other Than White, Whether or Not Artificially Coloured – Netherlands.* Tech. rep. HS Code 252329. GTAIC, Feb. 2026.

[113] Constructly Tools. *Sand Calculator (Tons, Yards & Cost) – Free & Accurate Tool.* Accessed: 2026-05-18. Feb. 2026.

[114] Ehab A. I.Amar Ahmed S. Soliman Adel M. El-Gohary Shady H. El-Nadoury Wegdan W. Kholief. "Magnetite sand as a low-cost material for electromagnetic shielding and mechanical enhancement of concrete". In: *Scientific Reports* 16 (2026).

[115] R. Syivarulli et al. "Upgrading the Quality of Solid Fuel Made from Nyamplung (Calophyllum inophyllum) Wastes Using Hydrothermal Carbonization Treatment". In: *Energy Engineering* 118.1 (2021), pp. 189–197.

[116] W. Wu et al. "Process Design and Techno-Economic Evaluation of a Decarbonized Cement Production Process Using Carbon Capture and Utilization". In: *Processes* 11.7 (July 2023), p. 2043.

[117] MATCHE. *Matches' Engineering to Chemical, Energy, Manufacturing, and Metallurgical Industries.* Accessed: 2026-03-27. n.d. URL: `https://www.matche.com/default.html`.

[118] C. Maxwell. *Cost Indices – Towering Skills.* Accessed: 2026-05-13. Mar. 2025. URL: `https://toweringskills.com/financial-analysis/cost-indices/`.

[119] Mauricio Mancio. "Electrochemical and in-situ Surface-Enhanced Raman Spectroscopic (SERS) study of passive films formed on low-carbon steel in highly alkaline environments". PhD dissertation. Berkeley, CA, USA: University of California, Berkeley, 2008.

[120] S.-H. Shim et al. "Calculation of Cement Composition Using a New Model Compared to the Bogue Model". In: *Materials* 14.16 (Aug. 2021), p. 4663.

[121] Ernst Worrell et al. "Carbon Dioxide Emissions from the Global Cement Industry". In: *Annual Review of Energy and the Environment* 26.1 (Nov. 2001), pp. 303–329.

[122] A. Prajapati et al. "Impact of Foaming Agent: Water Ratio on Foam Stability of Lightweight Concrete". In: *Applied Engineering and Technology* 3.2 (Aug. 2024), pp. 115–124.

[123] Jan Harmsen, André B. de Haan, and Pieter L. J. Swinkels. *Product and Process Design: Driving Innovation.* Berlin/Boston: Walter de Gruyter GmbH, 2018. ISBN: 978-3-11-046772-7.

[124] *Marktprijzen Energie, 2000-2025.* 2026. URL: `https://www.cbs.nl/nl-nl/maatwerk/2026/14/marktprijzen-energie-2000-2025`.

Appendix A

In this appendix the HoQ employed to translate the technical to customer requirements for the buffer, backfill and emplacement can be found, as well as a summary of relevant dimensions of the buffer and tunnel geometries.

A.1 House of Quality

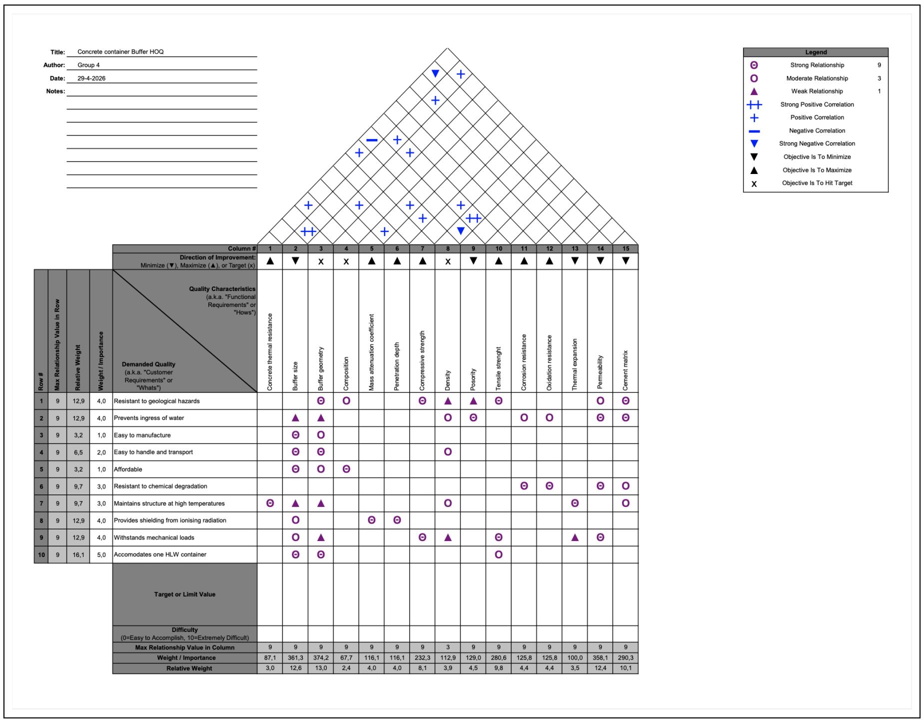

				Column #	1	2	3	4	5	6	7	8	9	10	11	12	13	14	15
				Direction of Improvement: Minimize (▼), Maximize (▲), or Target (x)	▲	▼	x	x	▲	▲	▲	x	▼	▲	▲	▲	▼	▼	▼
Row #	Max Relationship Value in Row	Relative Weight	Weight / Importance	Quality Characteristics (a.k.a. "Functional Requirements" or "Hows") Demanded Quality (a.k.a. "Customer Requirements" or "Whats")	Concrete thermal resistance	Buffer size	Buffer geometry	Composition	Mass attenuation coefficient	Penetration depth	Compressive strength	Density	Posority	Tensile strenght	Corrosion resistance	Oxidation resistance	Thermal expansion	Permeability	Cement matrix
1	9	12,9	4,0	Resistant to geological hazards			Θ	O			Θ	▲	▲	Θ				O	Θ
2	9	12,9	4,0	Prevents ingress of water		▲	▲					O	Θ		O	O		Θ	Θ
3	9	3,2	1,0	Easy to manufacture		Θ	O												
4	9	6,5	2,0	Easy to handle and transport		Θ	Θ					O							
5	9	3,2	1,0	Affordable		Θ	O	Θ											
6	9	9,7	3,0	Resistant to chemical degradation											Θ	Θ		Θ	O
7	9	9,7	3,0	Maintains structure at high temperatures	Θ	▲	▲					O					Θ		O
8	9	12,9	4,0	Provides shielding from ionising radiation		O			Θ	Θ									
9	9	12,9	4,0	Withstands mechanical loads		O	▲				Θ	▲		Θ			▲	Θ	
10	9	16,1	5,0	Accomodates one HLW container		Θ	Θ							O					
				Target or Limit Value															
				Difficulty (0=Easy to Accomplish, 10=Extremely Difficult)															
				Max Relationship Value in Column	9	9	9	9	9	9	9	3	9	9	9	9	9	9	9
				Weight / Importance	87,1	361,3	374,2	67,7	116,1	116,1	232,3	112,9	129,0	280,6	125,8	125,8	100,0	358,1	290,3
				Relative Weight	3,0	12,6	13,0	2,4	4,0	4,0	8,1	3,9	4,5	9,8	4,4	4,4	3,5	12,4	10,1

Figure A1: House of Quality of the concrete buffer.

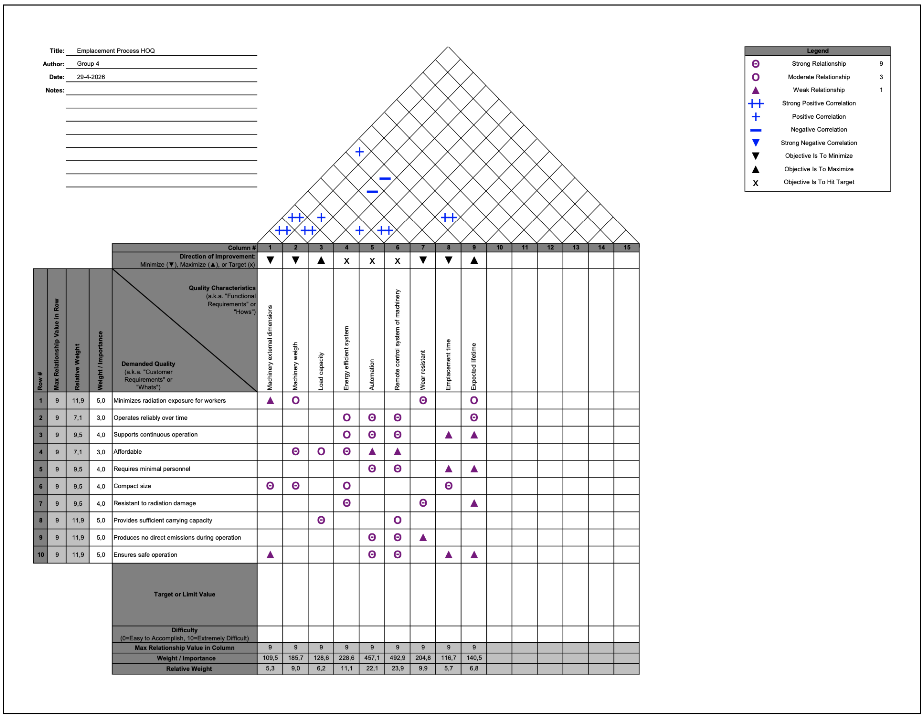

				Column #	1	2	3	4	5	6	7	8	9	10	11	12	13	14	15
				Direction of Improvement: Minimize (▼), Maximize (▲), or Target (x)	▼	▼	▲	x	x	x	▼	▼	▲						
Row #	Max Relationship Value in Row	Relative Weight	Weight / Importance	Quality Characteristics (a.k.a. "Functional Requirements" or "Hows") Demanded Quality (a.k.a. "Customer Requirements" or "Whats")	Machinery external dimensions	Machinery weigth	Load capacity	Energy efficient system	Automation	Remote control system of machinery	Wear resistant	Emplacement time	Expected lifetime						
1	9	11,9	5,0	Minimizes radiation exposure for workers	▲	O					Θ		O						
2	9	7,1	3,0	Operates reliably over time				O	Θ	Θ			Θ						
3	9	9,5	4,0	Supports continuous operation				O	Θ	Θ		▲	▲						
4	9	7,1	3,0	Affordable		Θ	O	Θ	▲	▲									
5	9	9,5	4,0	Requires minimal personnel					Θ	Θ		▲	▲						
6	9	9,5	4,0	Compact size	Θ	Θ		O				Θ							
7	9	9,5	4,0	Resistant to radiation damage				Θ			Θ		▲						
8	9	11,9	5,0	Provides sufficient carrying capacity			Θ			O									
9	9	11,9	5,0	Produces no direct emissions during operation					Θ	Θ	▲								
10	9	11,9	5,0	Ensures safe operation	▲				Θ	Θ		▲	▲						
				Target or Limit Value															
				Difficulty (0=Easy to Accomplish, 10=Extremely Difficult)															
				Max Relationship Value in Column	9	9	9	9	9	9	9	9	9						
				Weight / Importance	109,5	185,7	128,6	228,6	457,1	492,9	204,8	116,7	140,5						
				Relative Weight	5,3	9,0	6,2	11,1	22,1	23,9	9,9	5,7	6,8						

Figure A2: House of Quality of the emplacement process.

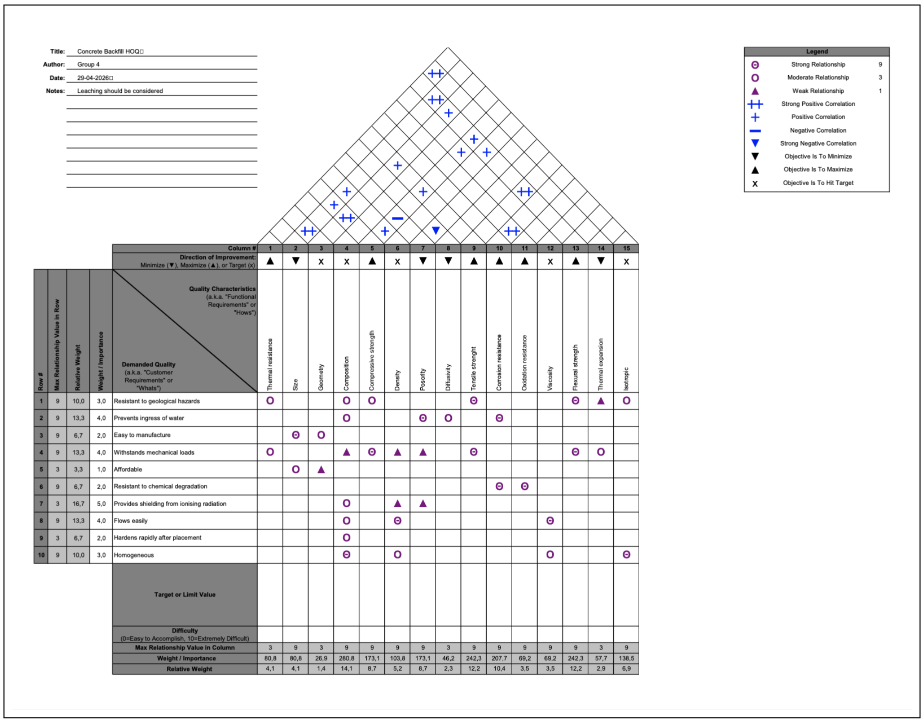

Title: Concrete Backfill HOQ□
Author: Group 4
Date: 29-04-2026□
Notes: Leaching should be considered

Row #	Max Relationship Value in Row	Relative Weight	Weight / Importance	Quality Characteristics (a.k.a. "Functional Requirements" or "Hows") / Demanded Quality (a.k.a. "Customer Requirements" or "Whats")	1 Thermal resistance	2 Size	3 Geometry	4 Composition	5 Compressive strength	6 Density	7 Posority	8 Diffusivity	9 Tensile strenght	10 Corrosion resistance	11 Oxidation resistance	12 Viscosity	13 Flexural strength	14 Thermal expansion	15 Isotropic
				Direction of Improvement: Minimize (▼), Maximize (▲), or Target (x)	▲	▼	x	x	▲	x	▼	▼	▲	▲	▲	x	▲	▼	x
1	9	10,0	3,0	Resistant to geological hazards	O			O	O				Θ				Θ	▲	O
2	9	13,3	4,0	Prevents ingress of water				O			Θ	O		Θ					
3	9	6,7	2,0	Easy to manufacture		Θ	O												
4	9	13,3	4,0	Withstands mechanical loads	O			▲	Θ	▲	▲		Θ				Θ	O	
5	3	3,3	1,0	Affordable		O	▲												
6	9	6,7	2,0	Resistant to chemical degradation										Θ	Θ				
7	3	16,7	5,0	Provides shielding from ionising radiation				O		▲	▲								
8	9	13,3	4,0	Flows easily				O		Θ						Θ			
9	3	6,7	2,0	Hardens rapidly after placement				O											
10	9	10,0	3,0	Homogeneous				Θ		O						O			Θ
				Target or Limit Value															
				Difficulty (0=Easy to Accomplish, 10=Extremely Difficult)															
				Max Relationship Value in Column	3	9	3	9	9	9	9	3	9	9	9	9	9	3	9
				Weight / Importance	80,8	80,8	26,9	280,8	173,1	103,8	173,1	46,2	242,3	207,7	69,2	69,2	242,3	57,7	138,5
				Relative Weight	4,1	4,1	1,4	14,1	8,7	5,2	8,7	2,3	12,2	10,4	3,5	3,5	12,2	2,9	6,9

Legend		
Θ	Strong Relationship	9
O	Moderate Relationship	3
▲	Weak Relationship	1
++	Strong Positive Correlation	
+	Positive Correlation	
−	Negative Correlation	
▼	Strong Negative Correlation	
▼	Objective Is To Minimize	
▲	Objective Is To Maximize	
x	Objective Is To Hit Target	

Figure A3: House of Quality of the concrete backfill.

A.2 Relevant dimensions

Table A1: Relevant dimensions of disposal package and facility.

	Number	**Diameter (m)**	**Length (m)**
SS canister	8000	0.43	1.335
CS overpack	8000	0.49	1.395
Concrete buffer	8000	2	2.5
Disposal tunnels	201	4	100

A.3 Material database

Table A2: Material property database.

Material		**Physical Properties**					**Exposure Limits**		
Name	**Formula**	**MW** (g/mol)	**BP** (°C)	**MP** (°C)	ρ (g/cm^3)	λ (W/mK)	**PEL** (mg/m^3)	**REL** (mg/m^3)	**IDLH** (mg/m^3)
Aluminium oxide	Al_2O_3	101.96	2977	2072	3.987	30	5	0	N/A
Calcium oxide	CaO	56.08	2850	2613	3.34	–	5	2	25
Iron oxide	Fe_2O_3	159.69	–	1539	5.25	–	10	5	2500
Silicon oxide	SiO_2	60.08	2950	1713	2.196	12	80	6	3000
Water	H_2O	18.02	99.98	0	1	0.6065	–	–	–
Magnetite	Fe_3O_4	231.53	–	1597	5.17	5	10	5	N/A
Gypsum	$CaSO_4 \cdot 2\,H_2O$	172.17	–	1450	2.32	0.17	10	5	N/A
Portland cement	Mainly $CaO-SiO_2-Al_2O_3$	–	–	–	3.15	0.29	10	5	5000
Sand	Mainly SiO_2	60.08	2950	1713	2.65	0.27	80	6	3000
Coal	Mainly C	12.01	–	3550	1.1	0.24	10	1	N/A
Carbon dioxide	CO_2	44.01	-78.5	-56.6	0.00198	0.0166	9000	9000	40000

Appendix B

In this appendix additional information with regards to the phenomena of corrosion, thermo-mechanical and impact calculations and radiation exposure were presented.

B.1 Corrosion analysis

$$a_{\mathrm{CO_2}} = 240 \frac{kg_{cement}}{m^3_{concrete}} \cdot \frac{0.67\, kg_{CaO}}{1\, kg_{cement}} \cdot \frac{1000\, g}{1\, kg} \cdot \frac{1\, mol_{CaO}}{56.08\, g_{CaO}} \cdot \frac{1\, mol_{Ca(OH)_2}}{1\, mol_{CaO}} = 2867.33\, mol_{Ca(OH)_2}/m^3 \tag{B1}$$

$$c = \frac{430\, mol_{CO_2}}{10^6\, mol_{air}} \cdot \frac{1\, mol_{air}}{0.0244\, m^3_{T=298K}} = 0.0176\, mol_{CO_2}/m^3 \tag{B2}$$

$$C_s = 1400 \frac{kg_{clay}}{m^3_{clay}} \cdot \frac{55\, kg_{\mathrm{H_2O}}}{100\, kg_{clay}} \cdot \frac{134.4\, mmol_{\mathrm{Cl}}}{1\, kg_{\mathrm{H_2O}}} \cdot \frac{1\, kmol}{10^6\, mmol} \cdot \frac{35.5\, kg_{\mathrm{Cl}}}{1\, kmol} = 3.67\, kg_{\mathrm{Cl}}/m^3_{clay} \tag{B3}$$

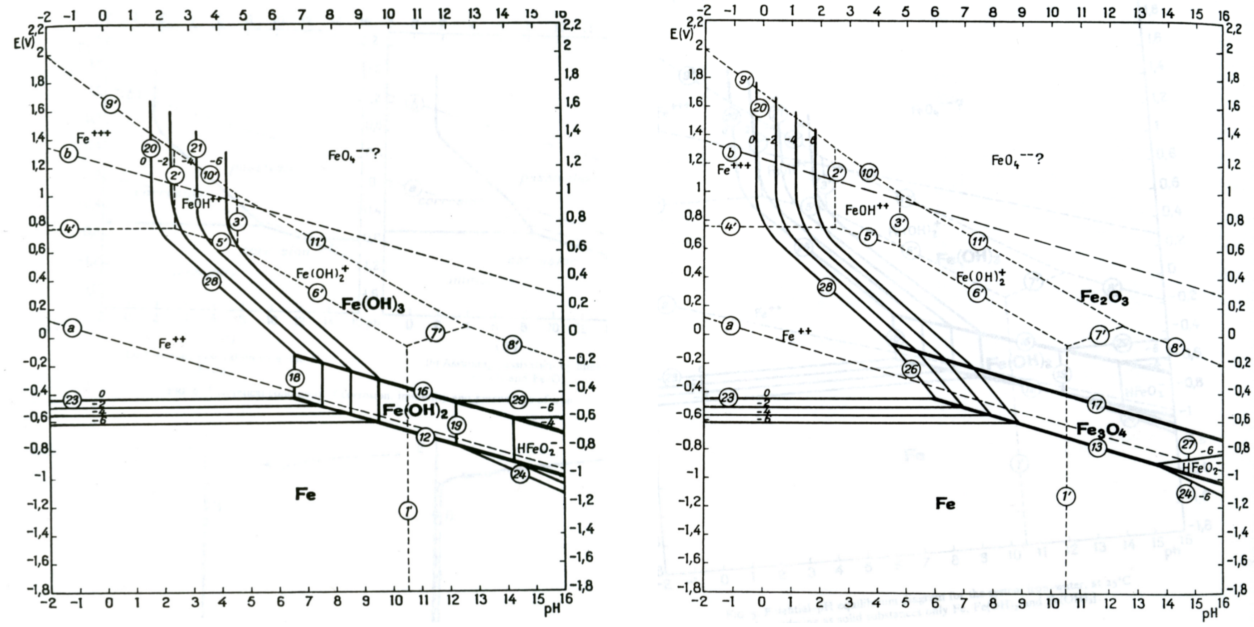

Figure B1: Pourbaix-pH diagrams for iron under nonaqueous (left) and aqueous environment (right)[119].

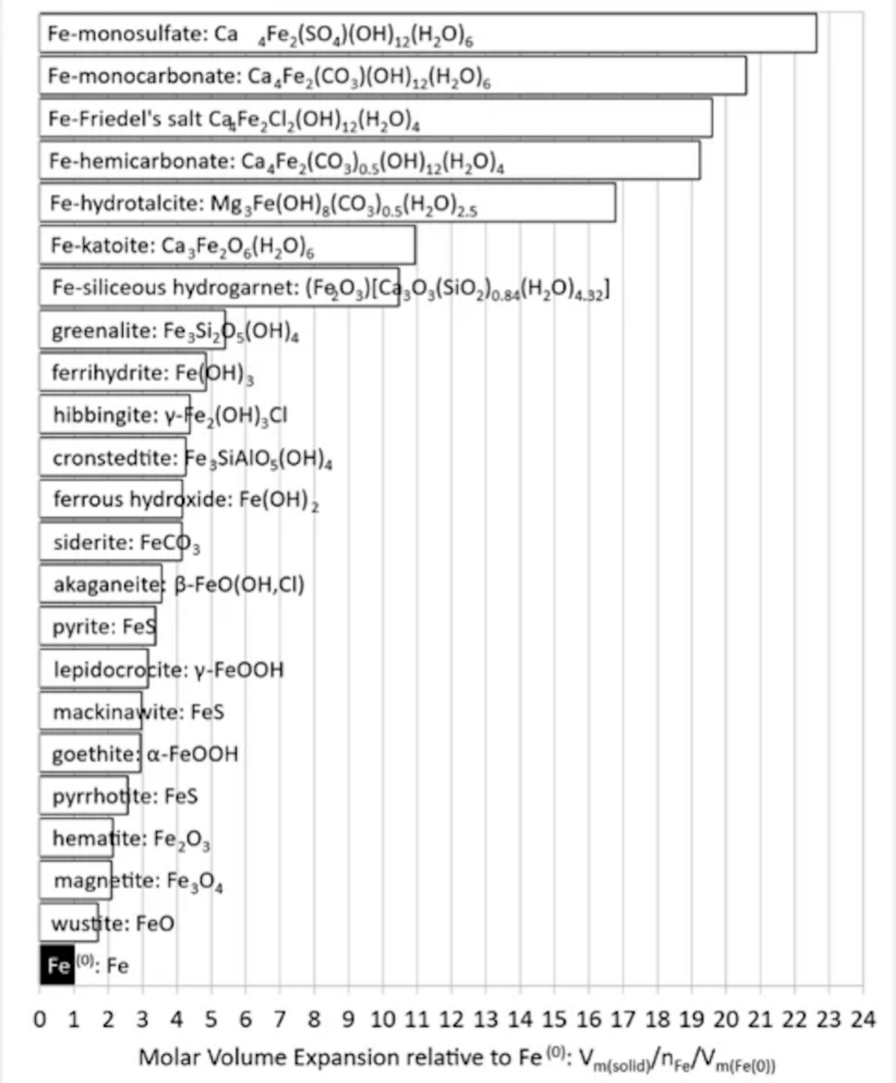

Figure B2: Relative volumes of potential corrosion products[42].

B.2 Thermo-mechanical and impact calculations

This section contain more figures covering thermo-mechanical- and impact stress calculations.

B.2.1 Thermo-mechanical

A large number of thermo-mechanical simulations were performed. In figures B3, B4 and B5, the results of a steady state thermo-mechanical stress study are shown for different storage times of the vHLW (ranging from 50-130 years). The figure with 200 W represents the longest storage time, while the figure with 680 W represents the shortest storage time. The base geometries of the models are shown in figure B8.

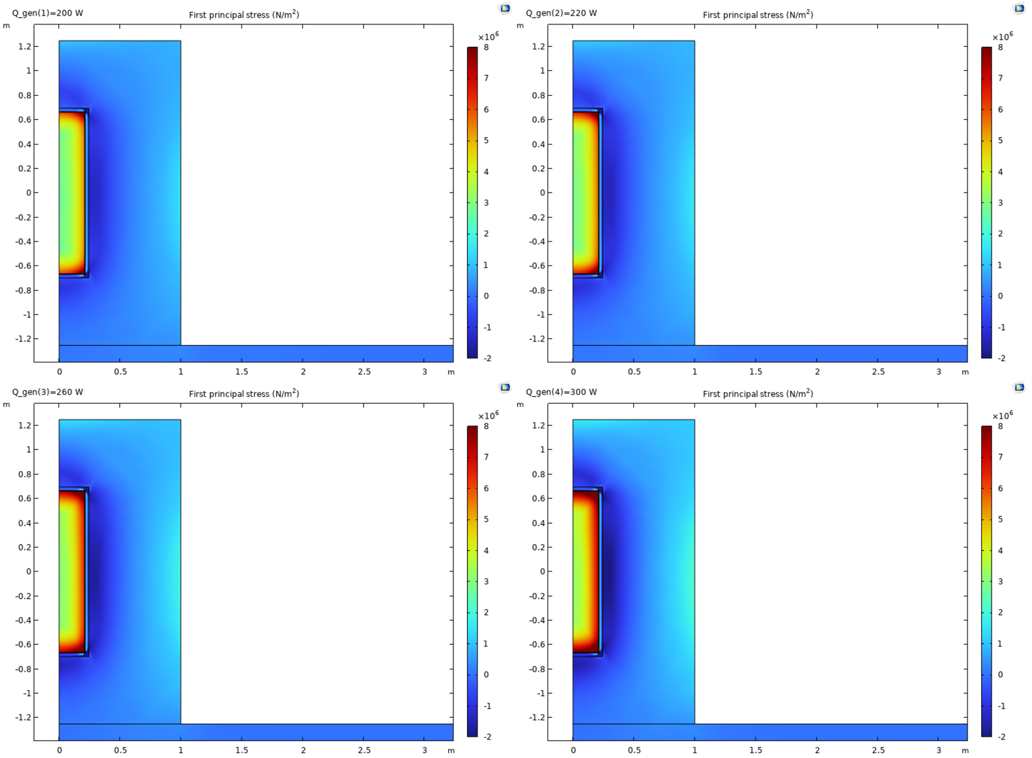

Figure B3: Thermo-mechanical stress on the disposal package for storage times of 100, 110, 120 and 130 years, corresponding to a thermal power of 300, 260, 220 and 200 W, respectively.

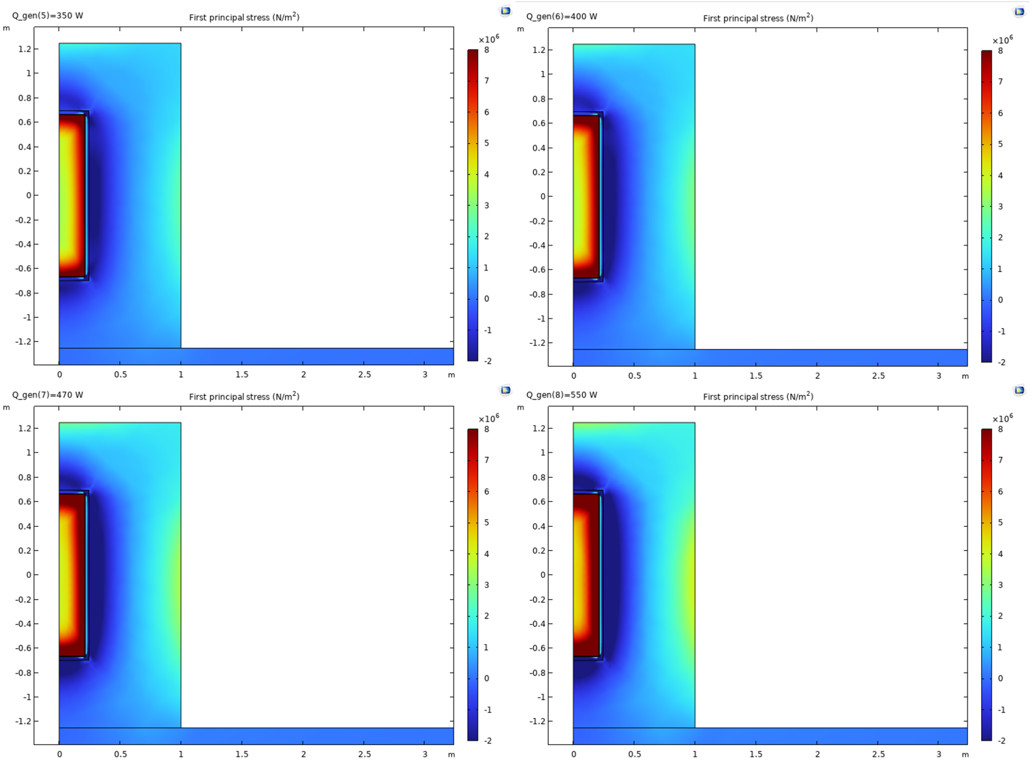

Figure B4: Thermo-mechanical stress on the disposal package for storage times of 60, 70, 80 and 90 years, corresponding to a thermal power of 550, 470, 400 and 350 W, respectively.

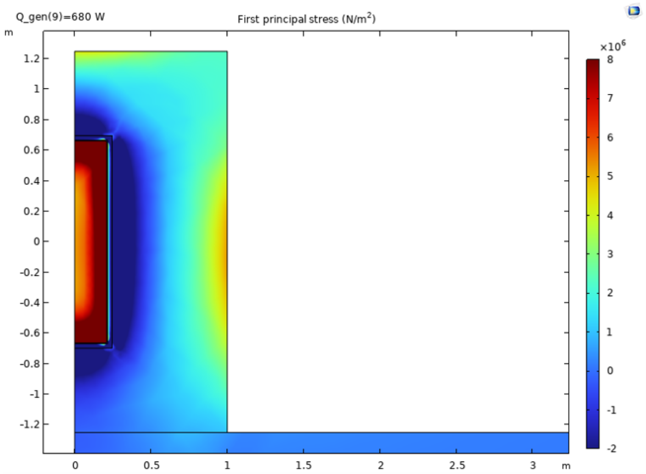

Figure B5: Thermo-mechanical stress on the disposal package for a storage time of 50 years, corresponding to a thermal power of 680 W.

The first principal stress on the disposal package gives a good insight into possible failure modes, as the maximum principal stress indicates the highest tensile force within the material, and therefore, the place where a fracture is the most likely. However, the stresses acting on the disposal package, especially on the buffer, are much more complex. For this reason, the radial and circumferential components of the stress tensor were evaluated separately and plotted as a function of the buffer radius. The evaluation line was the middle of the buffer (in the z direction).

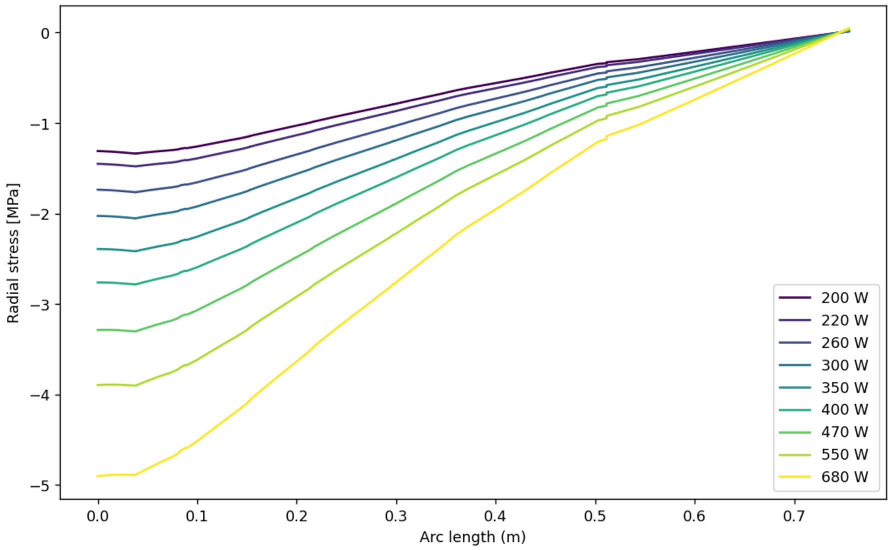

Figure B6: Radial component of the stress tensor acting on the buffer.

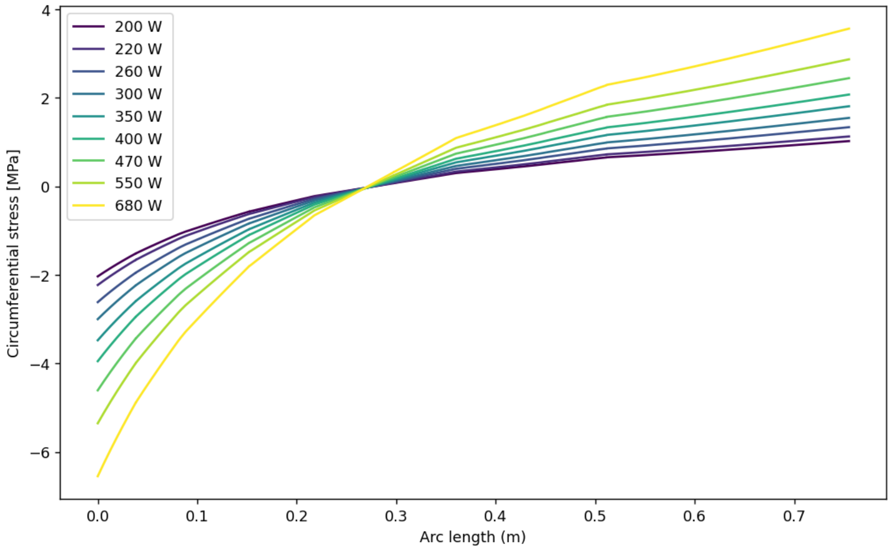

Figure B7: Circumferential component of the stress tensor acting on the buffer.

What is interesting to note about these stress components is that the circumferential component has a point of 0 stress around r = 0.27 m, which remains constant for the different heat fluxes. This indicates that the stress profile for some part is geometric. Since the buffer diameter was constant for this particular set of data points, it is difficult to say what effect it has on the location of the point of no stress. One of the main findings in this decoupling of stress components is that the first principal stress originates mostly from the circumferential tensile stresses.

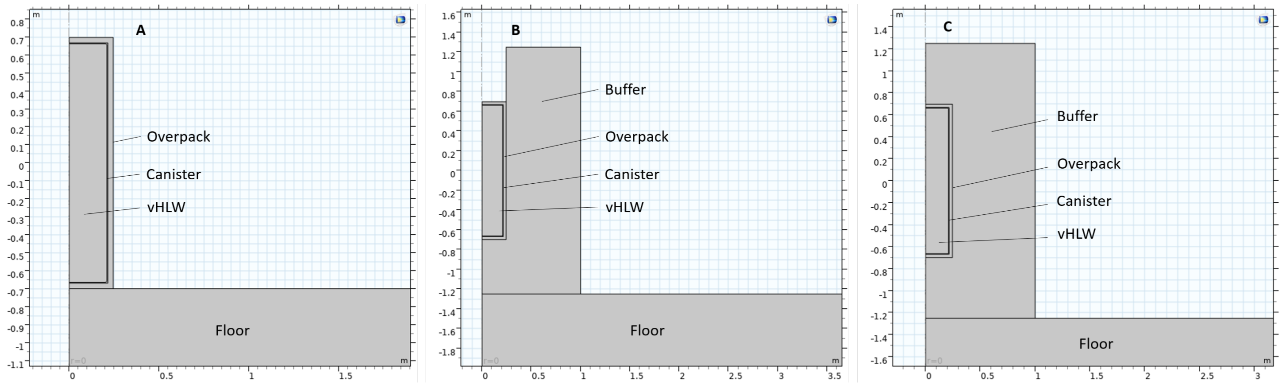

Figure B8: COMSOL geometries used for A) vHLW temperature approximation, B) overpack temperatures after placing into buffer, C) final temperature and thermo-mechanical stress calcualtions

B.2.2 Impact

Apart from thermo-mechanical, several impact stress studies were also performed. In figure B9, the first principal stresses experienced in the buffer are presented for a drop of 2cm. The model geometry is shown in figure B10

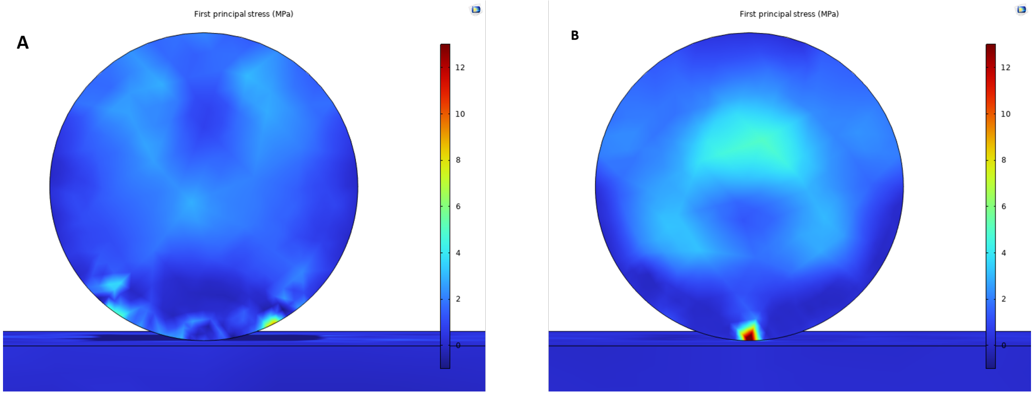

Figure B9: First principal stresses present in the buffer after a drop of 2cm at A) 0.001 s and B) 0.0015 s.

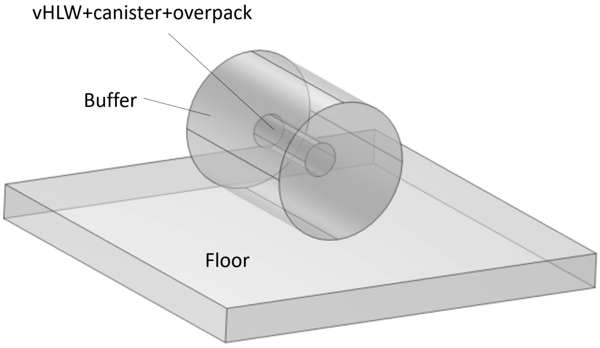

Figure B10: COMSOL geometry used for impact simulations

B.3 Radiation exposure

Table B1: Approximate elemental weight fractions imputed in XCOM for gamma-ray attenuation coefficient estimations.

Elements	Vitrified waste form	Stainless steel	Carbon steel	Magnetite concrete
Fe	0	0.840000	0.980000	0.542883
C	0	0	0.020000	0
Si	0.262220	0	0	0.078301
O	0.504396	0	0	0.342028
Cr	0	0.160000	0	0
B	0.053024	0	0	0
Na	0.117611	0	0	0
Ca	0.017431	0	0	0.031200
H	0	0	0	0.003976
Al	0.012909	0	0	0.001612
Li	0.016996	0	0	0
Mn	0.015413	0	0	0

Appendix C

In this appendix all relevant calculations related with the cement production process can be found, namely chemical reactions for the production of cement, feed of raw materials, production rate, capacity and costs, as well as additional information with regards with the process in question.

C.1 Chemical reactions for cement production

$$CaCO_3 \rightarrow CaO + CO_2 \qquad (700\text{–}900°C) \tag{R12}$$

$$2CaO + SiO_2 \rightarrow Ca_2SiO_4 \qquad (800\text{–}900°C) \tag{R13}$$

$$3CaO + Al_2O_3 \rightarrow Ca_3Al_2O_6 \qquad (900\text{–}1300°C) \tag{R14}$$

$$4CaO + Al_2O_3 + Fe_2O_3 \rightarrow Ca_4Al_2Fe_2O_{10} \qquad (900\text{-}1300°C) \tag{R15}$$

$$CaO + Ca_2SiO_4 \rightarrow Ca_3SiO_5 \qquad (> 1300°C) \tag{R16}$$

C.2 Concrete required for buffer

Based on the available data, approximately 8000 disposal packages are expected to be managed in the coming decades[5]. However, as a conservative assumption (+10%) a total number of 8800 canister was employed in order to prevent the lack of buffer material and to be able provide additional flexibility. In order to estimate the production of cement required to meet this need was calculated as a function of the volume of material. Dimensions of the stainless steel canister were D=430 mm and H=1335 mm, with a carbon steel overpack of 30 mm[5]. As the concrete buffer must have a diameter of 2 m and length of 2.5 m the volume of material was calculated according to equations C1-C4[5].

$$V = \frac{\pi D^2 H}{4} \tag{C1}$$

$$V_{canister-overpack} = \frac{\pi \cdot 0.49^2 \cdot 1.395}{4} = 0.2631\ m^3 \tag{C2}$$

$$V_{buffer} = \frac{\pi \cdot 2^2 \cdot 2.5}{4} = 7.854\ m^3 \tag{C3}$$

$$V_{total,concrete} = (7.854 - 0.2631) \cdot 8800 = 66800\ m^3 \tag{C4}$$

Based on literature values, it was found that concrete with approximately 74 weight percent magnetite displayed enhanced properties, namely with increased density and compressive strength. The high density cement-based composite had the composition presented on table C1, allowing to calculate the corresponding amount of each raw material to fulfil the concrete volume needed for the buffer construction. The aforementioned material was named CM60 due to its magnetite volume fraction, and displayed a standard water to cement ratio of 0.5, while sand (1-2 mm), as well as fine and coarse magnetite aggregates were present in different sizes to improve homogeneity (1-2, 2-4, 4-8, 8-16 in mm)[14]. The high amount of magnetite used in the composition is mainly related to the need for increased density and improved radiation shielding performance of the concrete buffer.

Table C1: Concrete CM60 composition.

	Cement	**Water**	**Sand**	**Magnetite**	**Superplaticizer**
Composition (kg/m^3)	240	120	530	2520	0.96
Total (tonne)	16032	8016	35404	168336	64.1

Hence, for the manufacturing of the corresponding cement, a standard Portland type was selected as starting point, were certain parameters should be met to ensure proper mechanical properties, namely compressive strength, and heat of hydration. In table C2 (cement notation is used from this point onwards), the target and calculated values were listed as a function of limestone, shale, sand and iron ore composition.

Table C2: Clinker composition calculations.

Component	Limestone	Shale	Sand	Iron ore	Target (%)	Actual (%)
C_3S					50-60	54
C_2S					15-25	25
C_3A					8-12	9
C_4AF					8-12	10
C	82.96	5.34			62-65	67
S	10.63	66.25	96.20	11.35	19-21	23
A	3.50	20.32	1.80	2.10	4-6	5
F	1.73	6.40	1.60	86.45	3-5	3

The presented values were calculated based on the composition of each raw material and following Bogue equations, where it is relevant to highlight that computations were designed by assuming no losses of oxides, clinker is formed by four principal phases and Fe_2O_3 and Al_2O_3 appear first in C_4AF and excess alumina in C_3A. Thus, equations C5-C8 were derived from this approach and used to calculate the corresponding weight percentages.

$$\mathrm{C_3S} = 4.071C - 7.602S - 6.719A - 1.430F \tag{C5}$$

$$\mathrm{C_2S} = 2.867S - 0.754\mathrm{C_3S} \tag{C6}$$

$$\mathrm{C_3A} = 2.650A - 1.692F \tag{C7}$$

$$\mathrm{C_4AF} = 3.043F \tag{C8}$$

Finally, three ratios, principally the Alumina Modulus (AM), Silica Modulus (SM) and Lime Saturation Factor (LSF) were checked to investigate whether the different clinker phases were relatively balanced, for which literature values were used, namely 1.4, 2.4 and 1.0, respectively[74]. Using equations C9, C10 and C11, it was found that certain deviation occurred from the theoretical values, but previous calculations with the Bogue equations illustrated that the stoichiometric requirements of raw mixes were within acceptable boundaries[120].

$$AM = \frac{A}{F} = \frac{5.46}{3.14} = 1.74 \tag{C9}$$

$$SM = \frac{S}{A+F} = \frac{23.10}{5.46+3.14} = 2.68 \tag{C10}$$

$$LSF = \frac{C}{2.8S + 1.18A + 0.7F} = \frac{66.62}{2.8 \cdot 23.10 + 1.18 \cdot 5.46 + 0.7 \cdot 3.14} = 0.91 \tag{C11}$$

The total consumption of raw materials was found to be 1570 kg per clinker tonne[104], which is milled with 5% gypsum[74, 121]. Therefore, for the production of 1 tonne of cement of the mentioned specifications, 50 kg of gypsum and 950 kg of clinker was used, leading to an overall raw material inlet of approximately 1500 kg. As a result, to produce 16032 tonnes of cement, the following quantities listed in table C3 of raw materials were needed. It is noteworthy that these values include the loss on ignition of each compound (39.52; 5.15; 1.00; 10.55 in %, respectively[74]), which is a measurement of volatiles, namely CO_2 in the cement industry, that is loss upon heating on a mass basis.

Table C3: Raw materials requirements for clinker and cement production for high density concrete.

	Limestone	Shale	Sand	Iron ore	Gypsum
Composition Loss free basis(%)	80	13	7	7	-
Composition as received (%)	86	9	4	1	-
Total (tonne)	19647	2056	914	229	802

As expected, limestone represents the largest raw material demand because it is the main source of calcium oxide required for clinker production. Calcium-based phases such as alite (C_3S) and belite (C_2S) are the principal compounds responsible for the mechanical strength of Portland cement, which explains the high proportion of limestone used in the process [77].

C.3 Concrete required for backfill

In spite of the difference in required properties between the buffer and backfill concrete, namely being the former a high density with magnetite and the latter a foamed variation, the cement used was considered to be identical to the one described before. Based on literature values, approximately 39 waste packages can be disposed in one tunnel, which had a length of 100 meters and an inner diameter of 4 meters. Hence, a total of 206 tunnel segments would have to be backfilled after the emplacement of 8000 canisters. Assuming a cylindrical tunnel geometry and by subtracting the space occupied by the packages, the total foamed concrete volume needed was calculated by equations C12-C14. Over the computed value a +10% safety margin was assumed in order to ensure a sufficient manufactured volume, leading to a final result of 215345 m^3.

$$V_{tunnel} = \frac{\pi \cdot 4^2 \cdot 100}{4} = 1256.64\ m^3 \tag{C12}$$

$$V_{package} = 7.854 \cdot 39 = 306.31\ m^3 \tag{C13}$$

$$V_{total,concrete} = (1256.64 - 306.31) \cdot 206 = 195768\ m^3 \cdot 1.10 = 215345\ m^3 \tag{C14}$$

The main objective of this composition was to obtain a low-density concrete capable of reducing the amount of material required for tunnel backfilling while still maintaining sufficient compressive strength after 28 days with a value close to 4 MPa.[5]. Therefore, the composition displayed in table C4 with a water/cement and foaming agent/water ratios of 0.63 and 1:10, respectively, was found suitable as it displayed magnitudes of ρ=1127 kg/m^3 and f'_c=4.61 MPa[122].

Table C4: Foamed concrete composition.

	Cement	**Sand**	**Water**	**Foam**
Composition (kg/m^3)	400	450	252	32.1
Total (tonne)	86138	96905	54267	6913

Furthermore, analogous calculations were performed starting from the concrete mass required to determine the raw materials input to manufacture the corresponding cement (see table C5).

Table C5: Raw materials requirements for clinker and cement production for low density concrete.

	Limestone	**Shale**	**Sand**	**Iron ore**	**Gypsum**
Composition Loss free basis(%)	80	13	7	7	-
Composition as received (%)	86	9	4	1	-
Total (tonne)	111118	11629	5168	1293	4307

C.4 Overall cement plant inflows

Owing to the performed calculations, the total cement production capacity of the plant must be approximately 102170 tonnes. By assuming an operation time of 8400 hours per year, a production rate of 12.16 tonne/hour was obtained. As expected, constructing a dedicated cement manufacturing facility for this project would not be economically justified, especially considering the relatively low production demand compared to industrial cement plants. Similar rotary kiln installations are capable of producing around 11000 tonnes of clinker per day[74], meaning that only 9 days of operation would be required to manufacture the total amount of material needed for the purpose.

C.5 Plant's order of magnitude estimates

Several estimations were made to predict the order of magnitude in terms of capital investment that would be needed for the site to be functional. As up/downscaling was not possible to be conducted due to the lack of available data the Bridgewater and Hill methods were used to perform an initial estimation[123]. The PFD depicted in figure C1 was subdivided into functional units (N) following the indications from each methodology, which in both cases led to N=6.

C.5.1 Bridgewater method

The Bridgewater method employs the relationship given in equation C15 for plant capacities (Q) larger than 60000 tons/year, being in this case Q=102170 tons/year. Based on previous conducted calculations the reactor conversion (s) was found to be 0.6369. As a result the direct plant cost (C_{DPC}) totalled approximately 84.56 M$.

$$C_{DPC} = 4320N \left(\frac{Q}{s}\right)^{0.675} = 4320 \cdot 6 \left(\frac{102170}{0.6369}\right)^{0.675} = 84.56\ M\$ \tag{C15}$$

Furthermore, the direct permanent investment cost (C_{DPI}) was obtained by including the OSBL expenses, which assuming grass-roots construction represent an 80% increase. Assuming 40% increase in cost for contingency, and to that an additional 10% for land cost and a 15% for the plant's Working Capital (WC) , the total capital investment (C_{TCI}) was of 332.30 M€ after the corresponding currency update from 2010 to June 2024.

$$C_{DPI} = C_{DPC} \cdot (1 + F_{OSBL}) = 84.56 \cdot (1 + 0.8) = 152.21\ M\$ \tag{C16}$$

$$C_{TDC} = 1.4 \cdot C_{DPI} = 1.4 \cdot 152.21 = 213.10\ M\$ \tag{C17}$$

$$C_{TPI} = 1.1 \cdot C_{TDC} = 1.1 \cdot 213.10 = 234.41\ M\$ \tag{C18}$$

$$C_{TCI} = 1.15 \cdot C_{TPI} = 1.15 \cdot 234.41 = 269.57\ M\$ \tag{C19}$$

$$C_{TCI}^{2024} = \frac{CEPCI_{2024}}{CEPCI_{2010}} \cdot C_{TCI}^{2010} = \frac{798.8}{550.8} \cdot 269.57 = 390.94\ M\$ = 332.30\ \text{M€} \tag{C20}$$

C.5.2 Hill method

The Hill method is based on the production rate factor, F_{PR} (equation C22), to calculate the module cost, MC, for purchase, delivery, and installation of each piece of equipment. From this, the module cost (MC) for each subsection of the system is expressed as formulated in equation C21, where F_M is a factor taking into account different material's costs (F_M=1.3 for stainless steel 304), and P_{design} is equal to the operating pressure of the module. As in this case the entire plant operates at 1 bar, it was set to 7 bar as indicated in the methodology.

$$MC_i = F_{PR} \cdot F_M \left(\frac{P_{design}}{7}\right)^{0.25} \cdot 160000 \tag{C21}$$

$$F_{PR} = \left(\frac{102170}{4536}\right)^{0.6} = 6.48 \tag{C22}$$

$$MC_{<7\,bar} = 6.48 \cdot 1.3 \cdot \left(\frac{7}{7}\right)^{0.25} \cdot 160000 = 1.35\ M\$ \tag{C23}$$

A similar approach as to the one mentioned in the Brigewater method was followed in order to translate the C_{DPC} (here including a process type factor of F_{PI}=1.85 for the handling of solids) into C_{TCI}, with the main difference that the C$_{DPI}$ was described as formulated in equation C25, where the construction factor (F$_C$=0.15 for outdoor construction) was included, giving a total of 64.27M€.

$$C_{DPC} = F_{PI}\left(\frac{CEPCI_{2024}}{CEPCI_{2010}}\right)\sum MC_i = 1.85 \cdot \frac{798.8}{550.8} \cdot 1.36 \cdot 6 = 21.89\ M\$ \tag{C24}$$

$$C_{DPI} = (1 + F_C + F_{OSBL}) \cdot C_{DPC} = (1 + 0.15 + 0.8) \cdot 21.89 = 42.69\ M\$ \tag{C25}$$

$$C_{TDC} = 1.4 \cdot C_{DPI} = 1.4 \cdot 42.69 = 59.77\ M\$ \tag{C26}$$

$$C_{TPI} = 1.1 \cdot C_{TDC} = 1.1 \cdot 59.77 = 65.74\ M\$ \tag{C27}$$

$$C_{TCI} = 1.15 \cdot C_{TPI} = 1.15 \cdot 65.74 = 75.61\ M\$ = 64.27\ \text{M€} \tag{C28}$$

C.5.3 Equipment purchase price estimation

In addition to the aforementioned methodologies, several equipment purchase price were estimated by using Towler-Sinnott[88], Matche[117]. On the one hand, the general equation C29 was employed with a, b and n being constants related to the corresponding equipment type (grinders and mills) and S the sizes listed in table 23.

$$C_e = a + b \cdot S^n \tag{C29}$$

Furthermore, the website Matche was used to compute the value of the cyclone also with the sizes of table 23, as Towler-Sinnott did not present any parameters for this type of equipment. Specifically, the rotary kiln was estimated with the empirical relationship shown in equation C30. All equipment purchase cost were adjusted to June 2024 from their corresponding date by applying a currency correction as shown in previous calculations.

$$C_{kiln} = 9.5 \cdot 10^7 \left(\frac{F_{clinker}}{4000}\right)^{0.64} \tag{C30}$$

It is noteworthy that minor equipment (blowers, bucket elevators, storage tanks, among others) was not accounted for as this calculations only intended to provide a background on the reason why construction of an on-site cement manufacturing plant was not feasible for the reduced volume of material needed for the buffer and backfill. Material, location and installation factors were also not included.

C.6 Process Flow Diagram

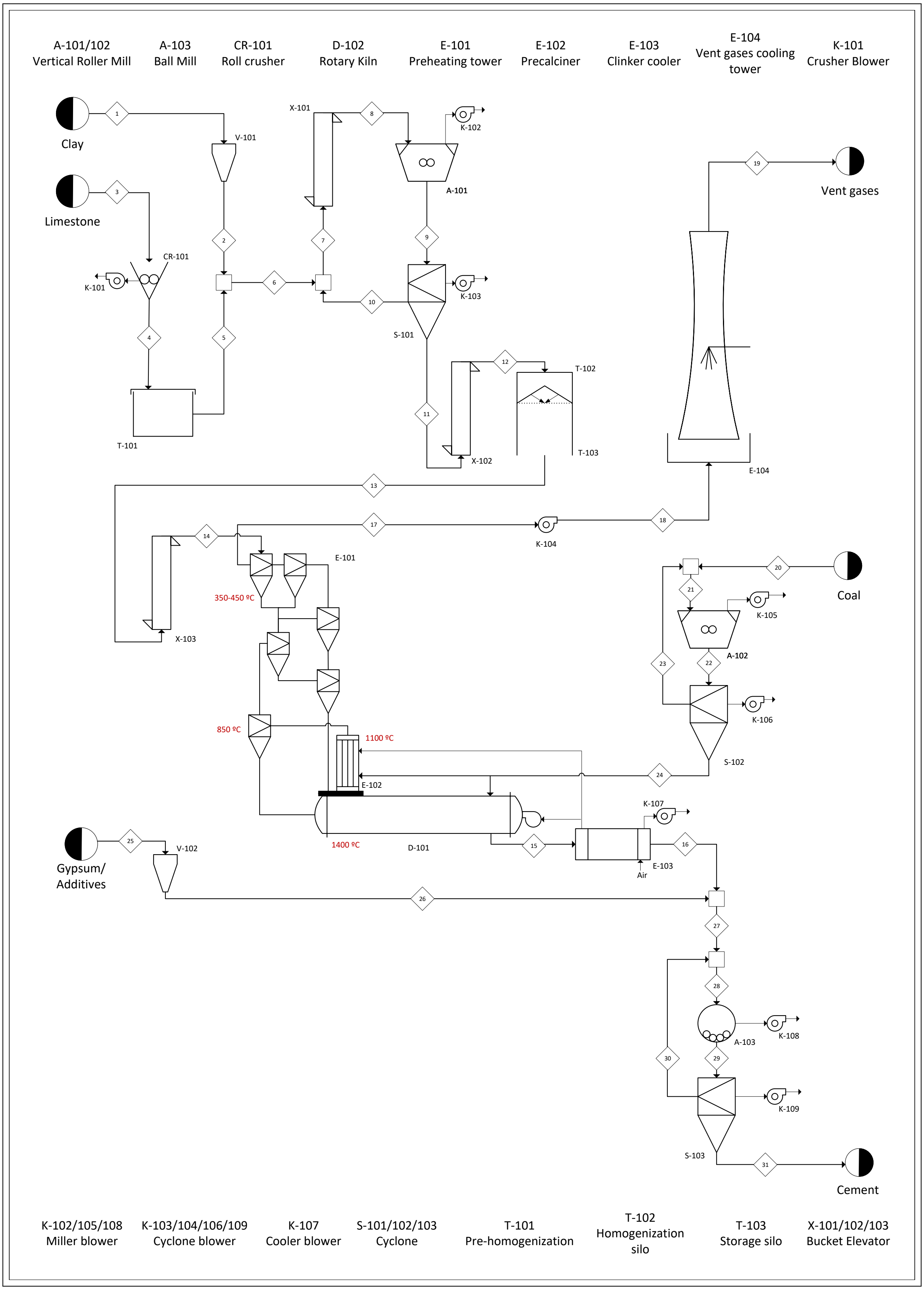

Figure C1: Process Flow Diagram for cement manufacture.

C.7 Piping and Instrumentation Diagram

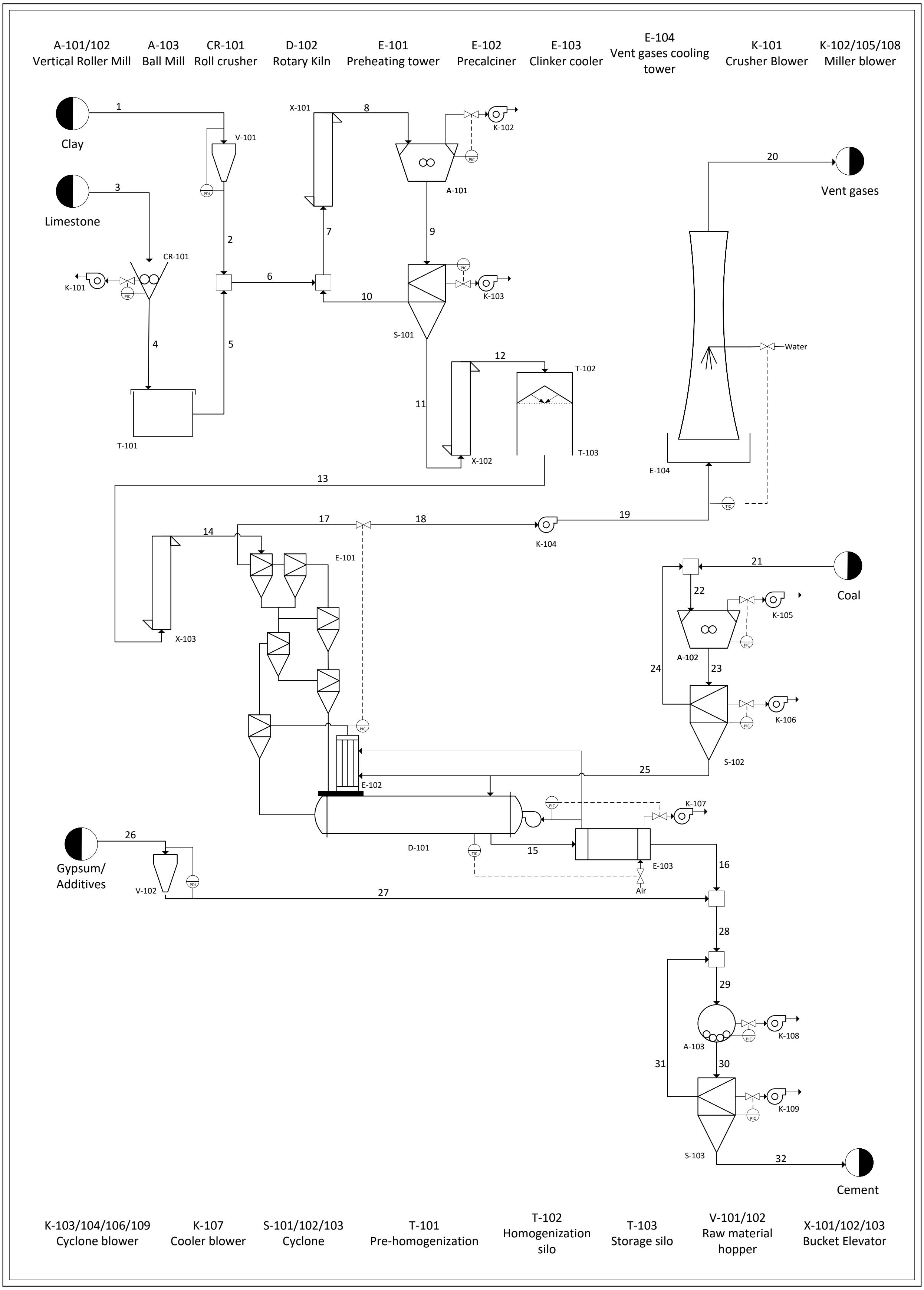

Figure C2: Piping and Instrumentation Diagram for cement manufacture.

Appendix D

In this appendix the derivation of the plug flow model used in the heat balance is shown in detail, as well as supporting calculations for the three cases of heat fluxes (200, 400 and 600W).

D.1 Plug Flow Model

For the system to be modelled as plug-flow, the Reynolds number in the disposal tunnel must be assessed as greater than ~ 4000. Using diameter $D_t = 4$ m, dynamic viscosity $\mu = 1.8 \cdot 10^{-5}$ Pa s, Re was calculated using equation D1. For mass flow rates, the values obtained with the final tunnel temperature calculations are used to confirm the validity of the initial PFS assumption.

$$Re = \frac{\rho_u \, v_d \, D_t}{\mu} = \frac{4 \, \dot{m}_{\text{air}}}{\pi \, \mu \, D_t} \tag{D1}$$

In the cases A, B and C presented in the report, the Re number is found to be respectively: 10610, 21044 and 31654. The result showed turbulent flow as it is $>$ that 4000 which is inline with a plug-flow model. For all cases the flow was calculated to have a flat (plug) velocity profile and strong radial mixing, which indicates uniform temperature at each cross section of the tunnel. Furthermore, it can be assumed that radial gradients are negligible compared to the axial temperature rise, thus 1D analysis is applicable. As for the turbulent pipe flow, the axial dispersion coefficient is approximated as $D_{\text{ax}} \approx 10.1 \cdot R \cdot u^*$ with the tunnel radius $R = (D+2)/2$ and the friction velocity $u^* = v_d \sqrt{f/8}$ with an assumed Darcy friction coefficient of $f = 0.02$. As a result, the thermal Péclet number was formulated as shown in equation D2(for a reasonable assumption of D=2 m), being around 10^3.

$$Pe = \frac{v_d \, L_d}{D_{\text{ax}}} = \frac{v_d \cdot L_d}{10.1 \cdot R \cdot v_d \sqrt{f/8}} = \frac{2 \, L_d}{10.1 \cdot (D+2) \cdot \sqrt{f/8}} \approx 2180 \gg 1 \tag{D2}$$

Since, the Péclet number was high, axial dispersion was therefore negligible compared to convective transport. Finally, the heat source can be approximated as steady state on the timescale of the airflow inside the tunnels as the cooling is superior to the air residence time in the tunnel.

D.2 Plug Flow system heat balance derivation

By applying the PFS balance model at steady state, an energy balance can be established, considering a ventilation duct, which runs along the tunnel roof and carries fresh air from the inlet at $z = 0$ ($T_d = T_{\text{cool}} = 15$ °C) toward $z = L_d$, with spouts releasing air into the tunnel at a uniform rate m_{cool} [kg s^{-1} m^{-1}]. The model used is shown here in the following figure:

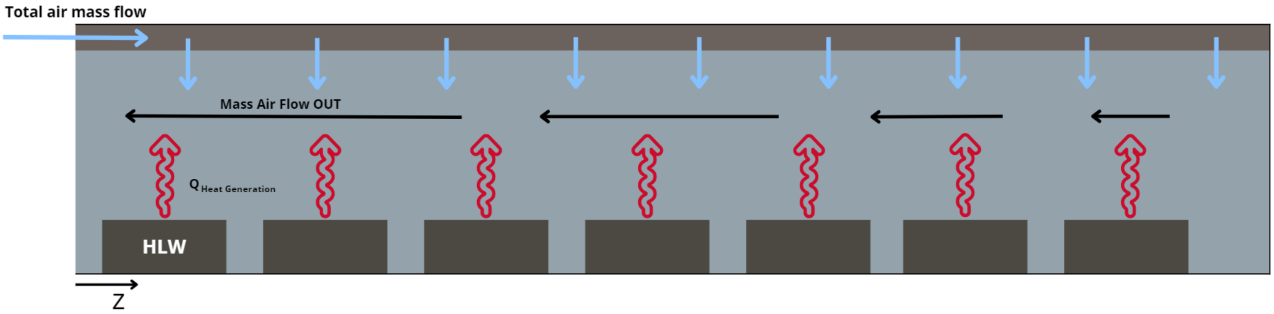

Figure D1: Plug flow approximation of tunnel cooling through ventilation duct.

The air inside the duct travels distance z inside the hot tunnel before being ejected, its temperature is thus, $T_d(z)$ and rises above T_{cool}. This gives an additional $\mathrm{d}T_d$ term that must be taken into account alongside the tunnel air temperature $T(z)$.

At steady state:

$$\frac{d(m_{cool} z T)}{dt} = 0 \tag{D3}$$

$$\frac{d(m_{cool}zT)}{dt} = \underbrace{m(z)\,cp_{air}\,T(z)}_{\text{Q in at } z} + \underbrace{m_{air}\,dz\,cp_{air}.T_{cool}}_{\text{fresh air}} + \underbrace{Q_{tot}\,dz}_{\text{heat}} - \underbrace{m(z+dz)\,cp_{air}\,T(z+dz)}_{\text{Q out at } z+dz} \tag{D4}$$

thus by rearranging this equation by dividing everything by dz

$$m(z)\,cp_{air}\,T(z) \;+\; m_{air}\,dz\,cp_{air}\,T_{cool} \;+\; Q_{tot}\,dz \;-\; m(z+dz)\,cp_{air}\,T(z+dz) = 0 \tag{D5}$$

by expanding on the term,

$$m(z+dz)\,cp_{air}\,T(z+dz) = cp_{air}\left(mT + \frac{d(mT)}{dz}\,dz\right) \tag{D6}$$

this gives :

$$m(z)\,cp_{air}\,T(z) \;+\; m_{air}\,dz\,cp_{air}\,T_{cool} \;+\; Q_{tot}\,dz_{\text{ heat}} \;-\; cp_{air}\left(mT + \frac{d(mT)}{dz}\,dz\right) = 0 \tag{D7}$$

since the heat capacity is constant, the equation can be divided on both sides by by cp_{air} and dz, this gives:

$$\frac{m(z)\,T(z)}{dz} + \frac{m_{air}\,dz\,T_{cool}}{dz} + \frac{Q_{tot}\,dz}{dz\,cp_{air}} - \frac{\left(mT + \frac{d(mT)}{dz}\,dz\right)}{dz} = 0 \tag{D8}$$

Rearranging gives :

$$\frac{d(m\,T)}{dz} = m_{air}T_{cool} + \frac{Q_{tot}}{cp_{air}} \tag{D9}$$

From equation D9, the equation is simplified by using the product rule:

$$T\,\frac{dm}{dz} + m\,\frac{dT}{dz} = m_{air}T_{cool} + \frac{Q_{tot}}{cp_{air}} \tag{D10}$$

However since $m(z) = m_{air} \cdot z$, this gives:

$$m_{air} \cdot z\,\frac{dT}{dz} = m_{air} \cdot (T_{cool} - T) + \frac{Q_{tot}}{cp_{air}} \tag{D11}$$

Giving the governing ODE :

$$\frac{dT}{dz} = \frac{T_{cool} - T}{z} + \frac{Q_{tot}}{cp_{air}\,m_{air}\,z} \tag{D12}$$

To comply to the temperature constraints the problem defines $\Delta T = T - T_{cool}$, so $\frac{d\Delta T}{dz} = \frac{dT}{dz}$, equation (D12) becomes:

$$\frac{d\Delta T}{dz} = -\frac{\Delta T}{z} + \frac{Q_{tot}}{cp_{air}\,m_{air}\,z} \tag{D13}$$

By multiplying both sides by z :

$$z\,\frac{d\Delta T}{dz} + \Delta T = \frac{Q_{tot}}{cp_{air}\,m_{air}} \tag{D14}$$

this can again be simplified with the product rule :

$$\frac{d(z\,\Delta T)}{dz} = z\,\frac{d\Delta T}{dz} + \Delta T\,\frac{dz}{dz} = z\,\frac{d\Delta T}{dz} + \Delta T \tag{D15}$$

$$\frac{d(z\,\Delta T)}{dz} = \frac{Q_{tot}}{cp_{air} \cdot m_{air}} \tag{D16}$$

By integrating both sides with respect to z, this gives:

$$z\,\Delta T = \frac{Q_{tot}}{cp_{air}\,m_{air}} z + C \tag{D17}$$

However for ΔT to remain finite ($z \to 0$), $C = 0$.

Rearranging the equation :

$$\Delta T = \frac{Q_{tot}}{cp_{air}\,m_{air}} \tag{D18}$$

Now re-substituting back $\Delta T = T - T_{cool}$, this gives $T(z)$ as:

$$T(z) = T_{cool} + \frac{Q_{tot}}{cp_{air}\,m_{air}} \tag{D19}$$

D.3 Additional results

$$m_{t,28,A} = \frac{7800}{13065} = 0.60\,kg/s \qquad m_{t,28,B} = \frac{15600}{13065} = 1.19\,kg/s \qquad m_{t,28,C} = \frac{23400}{13065} = 1.79\,kg/s \tag{D20}$$

$$d_{v,\min,A} = \sqrt{\frac{4 \cdot 0.60}{\pi \cdot 1.30 \cdot 8}} = 0.27 \text{ m} \qquad d_{v,\min,B} = \sqrt{\frac{4 \cdot 1.19}{32.67}} = 0.38 \text{ m} \qquad d_{v,\min,C} = \sqrt{\frac{4 \cdot 1.79}{32.67}} = 0.47 \text{ m} \tag{D21}$$

$$\begin{aligned} \dot{m}_{\text{fac},A} &= \frac{1.60 \cdot 10^6}{13065} = 122\ kg/s \quad \dot{V}_A = 94\ m^3/s \\ \dot{m}_{\text{fac},B} &= \frac{3.20 \cdot 10^6}{13065} = 245\ kg/s \quad \dot{V}_B = 188\ m^3/s \\ \dot{m}_{\text{fac},C} &= \frac{4.80 \cdot 10^6}{13065} = 367\ kg/s \quad \dot{V}_C = 282\ m^3/s \end{aligned} \tag{D22}$$

$$W_{\text{cool},A} = \frac{1.60[MW]}{4} = 400\,kW \qquad W_{\text{cool},B} = \frac{3.20[MW]}{4} = 800\,kW \qquad W_{\text{cool},C} = \frac{4.80[MW]}{4} = 1200\,kW \tag{D23}$$

Appendix E

This appendix provides supplementary information to some of the methods employed to assess the sustainability of the product designed.

E.1 Life Cycle Assessment complementary information

Table E1: LCA comparison of different scenarios.

	$CO_{2,eq}$/FU				**Pt/FU**			
	Scenario 1	Scenario 2	Scenario 3	Scenario 4	Scenario 1	Scenario 2	Scenario 3	Scenario 4
Magnetite	18412	33147	18412	18412	1.87	3.36	1.87	1.87
Cement Portland	9985	9985	9985	0	0.46	0.46	0.46	0.00
Limestone	0	0	0	27	0.00	0.00	0.00	0.01
Shale	0	0	0	4	0.00	0.00	0.00	0.00
Sand	0	0	0	1	0.00	0.00	0.00	0.00
Iron ore	0	0	0	7	0.00	0.00	0.00	0.00
Gypsum	0	0	0	2	0.00	0.00	0.00	0.00
Electricity cement production	0	0	0	501	0.00	0.00	0.00	0.01
Coal cement production	0	0	0	58	0.00	0.00	0.00	0.00
Silica sand	601	0	601	601	0.07	0.00	0.07	0.07
Deionized water	6	6	6	6	0.00	0.00	0.00	0.00
Polymer foaming	157	157	157	157	0.06	0.06	0.06	0.06
Plasticiser for concrete	10	10	10	10	0.00	0.00	0.00	0.00
Stainless steel canister	610	478	610	610	0.25	0.07	0.25	0.25
Carbon steel overpack	907	907	907	907	0.29	0.29	0.29	0.29
Concrete mixing	118	118	4	118	0.00	0.00	0.00	0.00
Emplacement	1	1	0	1	0.00	0.00	0.00	0.00
Excavation	313	313	11	313	0.01	0.01	0.00	0.01
Concrete pumping	25	25	1	25	0.00	0.00	0.00	0.00
Transportation	2970	3226	2203	3139	0.25	0.30	0.24	0.25
TOTAL	**34116**	**48372**	**32909**	**24900**	**3.26**	**4.56**	**3.24**	**2.83**

E.2 Vent gas emissions complementary information

Among the different emissions generated during cement production, the most relevant compounds are listed below:

- **Nitrogen oxides (NO_x)**: This compound reacts with water and the ozone layer to form nitric acid that can lead to acid rain that damages infrastructure. Moreover, this compound also facilitates the formation of smog when combined with volatile compounds.
- **Sulphur dioxide (SO_2)**: reacts with ozone and water in the atmosphere and produces sulphuric acid that leads to acid rain and the depletion of the ozone layer, especially if it is paired with NOx.
- **Carbon dioxide (CO_2)**: Carbon dioxide is one of the main gases involved in global warming due to its properties as a greenhouse gas. This gas traps heat inside the atmosphere and makes the planet hotter over the years, causing climate change and harming the environment in the process.
- **Carbon monoxide (CO)** can cause air poisoning, which is a human health-related concern. It harms the environment by destroying the atmosphere's ozone. In addition, it is categorised as a flammable compound.

Appendix F

In this appendix the calculations regarding the economic feasibility of the product can be found, namely describing the associated costs as a function of the buffer diameter for further optimization in the final report.

F.1 Financial margin calculations

The upper-end profitable cost for vHLW disposal is determined by income and expenses incurred by SNF producers.

The income is estimated on the basis of the 2025 average electricity sale price in the Netherlands of 87.4 €/MWh, as reported by the Dutch central bureau for statistics[124], and a fuel burn-up of 50 GWd/tU representing, a conservative estimate for a nuclear reactor fleet composed of a mix of older (Borssele) and newer (currently in the planning stage) power plants. This leads to an estimated income of 104.9 million €/tU.

As for the expenses, the assumption commonly used in the chemical engineering industry according to which their largest fraction is made up by raw materials, cannot be applied. A quick calculation leads to a cost in the order of magnitude of only a few million euros per ton of uranium.

Therefore, a rapid first estimate of the total cost linked to the total expenses incurred over the lifetime of a nuclear power plant is better obtained from literature in the form of a levelized cost of electricity (LCOE), corresponding to the price per MWh set for the electricity produced that would lead to reaching the break even point at the end of reactor operation. This value is found to be equal to 74 €/MWh[108]. This estimate already includes a waste disposal contribution of 2.33 €/MWh, which has to be subtracted for the purposes of this estimate. Finally, inflation is taken into account, with an exchange ratio to 2025 euros of 1:1.196. Converting the so found value of 85.7 €/MWh in units expressed per ton of uranium, on the basis of the previously assumed 50 GWd/tU burn-up, yields a value of 102.8 million €/tU.

The difference between this cost estimate and the electricity cost based earnings estimate, yields a rough estimate of profit for the power plant per unit mass of uranium fuel utilized. Assuming approximate mass conservation in the reactor fuel, and considering the decrease in mass of waste consequent to reprocessing, leads to the final estimate of 8 million € per ton of vitrified waste.

F.2 Cost estimations

The volumes of the three different types of tunnels are estimated here as a function of buffer diameter

- Disposal tunnel Volume:
$$V_d = \pi \left(\frac{D+2}{2}\right)^2 (22{,}600)$$
- Transport tunnel Volume :
$$V_t = \pi \left(\frac{D+5}{2}\right)^2 (6250)$$
- Shaft Volume (with 2 shafts, one for security and one operational):
$$V_s = 2 \times \pi \left(\frac{D+3}{2}\right)^2 (500)$$

The total excavation volume is:

$$V_{tot} = 23.4 \cdot 10^3 \cdot D^2 + 161.9 \cdot 10^3 \cdot D + 590 \cdot 10^3 \tag{F1}$$

expressing volume in m^3. The final cost expression is:

$$C_{tunnelling} = 3.16 \cdot 10^3 \cdot D^2 + 21.9 \cdot 10^3 \cdot D + 79.7 \cdot 10^3 \tag{F2}$$

For buffer production the cost as a function of external diameter is:

$$C_{buffer} = 1.55 \cdot 10^3 \cdot D^2 - 233 \tag{F3}$$

Finally, the cost of backfilling can be expressed as

$$C_{backfill} = 86 \cdot D^2 + 1.29 \cdot 10^3 \cdot D + 4.7 \cdot 10^3 \tag{F4}$$

The total cost per container is then expressed as a sum of these three contributions, leading to the following quadratic expression for cost (in €):

$$C_{tot} = 4.8 \cdot 10^3 \cdot D^2 + 23.2 \cdot 10^3 \cdot D + 84.2 \cdot 10^3 \tag{F5}$$

Appendix G

In this appendix a detail description of the several creative and group process tools used during the project, as well as the planning followed.

G.1 Creativity

G.1.1 TRIZ

The Theory of Inventive Problem Solving (TRIZ), provides a systematic approach to idea generation. The principle of segmentation enabled the improvement of individual componenents of the buffer, backfill, and emplacement, without comprising the overall design.For example, the hybrid of a drum reel and air cushion vehicle was developed for the emplacement and a higher ratio of magnetite was added to the buffer. Furthermore, the prior action, acted as guidance to perform as many possible steps before emplacement (i.e casting), therefore minimising constraints imposed by operating 500 m underground. These principles were applied punctually rather than continuously, reflecting the limited creative freedom of the project.

G.1.2 Brainstorming

Brainstorming was the primary source of creative design solutions, which needs to be grounded in thorough literature research on material properties, availability, and feasibility, including solutions from other industries. Each member researched a specific area, then contributed ideas in a group setting. Nine concepts were identified, three each for the buffer, emplacement, and backfill and evaluated using the Pugh matrix before being presented to the group coach. Table G1, describes all the the methods used for creativity and their most significant outcome (concept evaluation).

Table G1: Overview of creativity methods used during the Concept Stage.

Week	**Method**	**Purpose**	**Outcome**
24/04-28/04	TRIZ	Generate ideas for improvements	Concepts for encasement, emplacement and backfill
28/04-07/05	Brainstorming with drawings	Visual idea generation and concept exploration	Several buffer, backfill and emplacement ideas were developed
23/04-24/04	House of Quality	Requirements into design properties	Key technical criteria were identified
09/05	Pugh Matrix	Compare and rank concepts	Most suitable concepts were selected for further development

G.2 Group process tools

G.2.1 Group Meetings

Weekly meeting were held throughout the entire project to share progress and coordinate tasks.Each member presented their work from the preceding week and flagged outstanding items, while one member took notes. Goals for the following week were then assigned, after which the group worked collaboratively for one to two hours. A shared Excel file tracked task subdivision and progress between the meetings.

G.2.2 Technical advisor meetings

To address highly technical aspects, the team contacted field experts by email, attaching an executive summary and COVRA's proposal. This resulted in a meeting with Dr.ir. A.C. Dieudonné (Associate Professor of Multiphysics Geomechanics) and, through E. Neeft, a visit to *Romein Beton*, a concrete manufacturing company. Prior to each meeting, a list of questions and a progress presentation were prepared, and one member was assigned to take notes.

G.2.3 Group Coach meetings

Weekly Friday meetings with the group coach followed a consistent format: a presentation of weekly progress, decisions, and concerns, followed by coach feedback on next steps for improvements.

G.2.4 Supervisor meetings

These took place thrice throughout the development of the design. The first meeting was scheduled on the 22^{nd} of April to visit the main facility where COVRA operates, and to get a general idea of the proposal. The second was planned for the 27^{th} of May, to visit the facility of *Romein Beton*, where concrete is made for the casting of the containers. Here, the main goal is to better understand the methodologies for production and casting of concrete, as well as to reassess the progress achieved by the team and define with more precision its future steps and goals. These last points are made possible by the presence of E. Neeft at this meeting. Lastly, a final meeting was arranged for the 24^{th} of June to ensure that the final design and the report meets all of the supervisor's needs.

G.2.5 WhatsApp groups between group members and group coach

To maintain a constant flow of information between group members and to clarify possible doubts regarding the project, two WhatsApp groups were created: one for team members only, used for internal coordination and meeting preparation; and one including the group coach, used for quick clarifications, sharing decisions, and maintaining regular contact.

G.3 Planning update

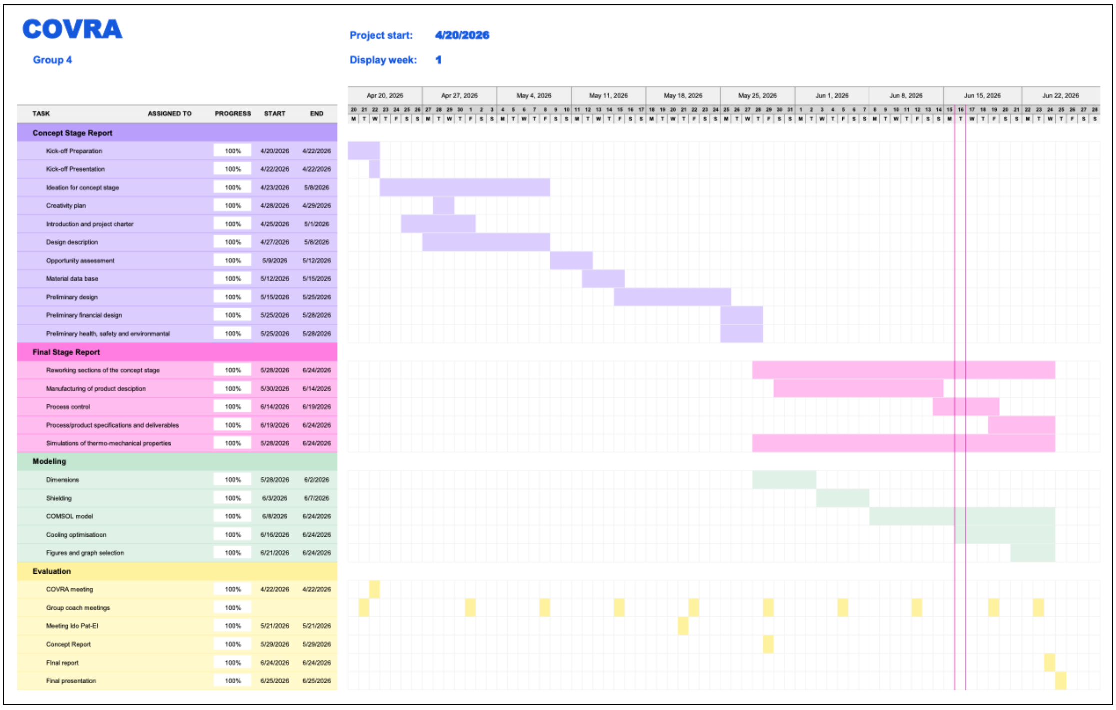
COVRA
Group 4

Project start: 4/20/2026
Display week: 1

TASK	ASSIGNED TO	PROGRESS	START	END
Concept Stage Report				
Kick-off Preparation		100%	4/20/2026	4/22/2026
Kick-off Presentation		100%	4/22/2026	4/22/2026
Ideation for concept stage		100%	4/23/2026	5/8/2026
Creativity plan		100%	4/28/2026	4/29/2026
Introduction and project charter		100%	4/25/2026	5/1/2026
Design description		100%	4/27/2026	5/8/2026
Opportunity assessment		100%	5/9/2026	5/12/2026
Material data base		100%	5/12/2026	5/15/2026
Preliminary design		100%	5/15/2026	5/25/2026
Preliminary financial design		100%	5/25/2026	5/28/2026
Preliminary health, safety and environmental		100%	5/25/2026	5/28/2026
Final Stage Report				
Reworking sections of the concept stage		100%	5/28/2026	6/24/2026
Manufacturing of product desciption		100%	5/30/2026	6/14/2026
Process control		100%	6/14/2026	6/19/2026
Process/product specifications and deliverables		100%	6/19/2026	6/24/2026
Simulations of thermo-mechanical properties		100%	5/28/2026	6/24/2026
Modeling				
Dimensions		100%	5/28/2026	6/2/2026
Shielding		100%	6/3/2026	6/7/2026
COMSOL model		100%	6/8/2026	6/24/2026
Cooling optimisatioon		100%	6/16/2026	6/24/2026
Figures and graph selection		100%	6/21/2026	6/24/2026
Evaluation				
COVRA meeting		100%	4/22/2026	4/22/2026
Group coach meetings		100%		
Meeting Ido Pat-El		100%	5/21/2026	5/21/2026
Concept Report		100%	5/29/2026	5/29/2026
Final report		100%	6/24/2026	6/24/2026
Final presentation		100%	6/25/2026	6/25/2026

Figure G1: Planning update for the concept stage.

Appendix H

In this appendix all the python codes used in the several section are shown.

H.1 Python codes

```python
#Libraries needed
import numpy as np
import scipy.sparse as sp
import scipy.sparse.linalg as spla
import matplotlib.pyplot as plt
import math


#Diffusion calculations via the first method
C_atm = 0.01759         # mol CO2/m^3 (concentration in the air)
a=2867.33               # mol CO2/m3
Temp=50+273             # K
Tref=298                # K
Pref=101.3              # Pa
P=101.3                 # Pa
eps=0.2                 # Porosity
S=0.7                   # Degree of saturation

D_sec=8*10**(-7)*(eps**(4/3))*((1-S)**(10/3))*((Temp/Tref)**(0.934))*((P/Pref)**(3.11))#m2/s
D_day=D_sec*86400
K=math.sqrt((2*D_day*C_atm)/a)

#Diffusion calculations via the first method
Cenv = 0.2               # Environmental coefficient
Cair =1                  # Air entrainment coefficient
a =1800                  # Concrete coefficient
b = -1.7                 # Concrete coefficient
fck =35                  # Concrete strenght
K2 = Cenv * Cair * a *(fck + 8)**(b)

#Time definitions
target_year=10
Days=target_year*365
time_CO2=np.linspace(0,Days,1000)
time_CO22=np.linspace(0,10,1000)


def carbonationfunction (t:np.ndarray,K:float) -> np.ndarray:
    """
    Calculation of the penetration depth of CO2
    Parameters:
        t (np.array): Time
        K (float): carbonization coefficient
    Returns (np.ndarray): penetration depth as a funcion of time
```

```
    """
    x=K*np.sqrt(t)
    return x

#Extract results of each method based on the different K definitions
results_carb=carbonationfunction(t=time_CO2,K=K)
results_carb2=carbonationfunction(t=time_CO22,K=K2)

#Plot
plt.figure()
plt.plot(time_CO2/365, results_carb2, label="Method 1")
plt.plot(time_CO2/365, results_carb*1000, label="Method 2")
plt.scatter(10, results_carb[-1]*1000 , color='#ff7f0e',s=30, zorder=5)
plt.text(
    10 - 0.8,
    results_carb[-1] * 1000,
    f"{results_carb[-1] * 1000:.2f}",
    fontsize=10,
    color="#ff7f0e"
)
plt.scatter(10, results_carb2[-1] , color='#1f77b4',s=30, zorder=5)
plt.text(
    10 - 0.8,
    results_carb2[-1],
    f"{results_carb2[-1]:.2f}",
    fontsize=10,
    color="#1f77b4"
)
plt.xlabel('time (years)')
plt.ylabel('Buffer thickeness (mm)')
plt.title('CO$_2$ penetration depth')
plt.legend()
plt.grid(True)
plt.show()
print(f"The final distance of carbonation is {results_carb[-1]*1000}mm")
```

Listing H1: Python code for computing the penetration depth of carbonation.

```
import numpy as np
import matplotlib.pyplot as plt
from scipy.special import erf
# Diffusion data
Deff_concrete=10**(-11) #m^2/s
Deff_foamed=10**(-9) #m^2/s
#Setting the time array
t_years=1200
t_final=t_years*365*24*3600 #seconds



#Setting the x array
```

```
x_liner_foamed=1.5 #m until the foamed is encountered
x_concrete=2.255 #m until the buffer is encountered
x_range=np.linspace(0,2.5,1200)



#Functions to define the error function and the concentration profile
def erf_of_x(x:float, D:float, t:float)->float:
    ’’’
    Calculation of the error function for the Concentration Cl-
    Parameters :
    x ( float ) : Penetration depth
    D ( float ) : Diffusion coefficient
    t (float) : Time that passed for the species to diffuse
    Returns ( float ) : Value of the error function’’’
    z = x / (2.0 * np.sqrt(D * t))
    return erf(z)

def Cxt_Cl (Cs:float,erf_value:float)->float:
    ’’’
    Calculation of the Concentration Cl-
    Parameters :
    Cs ( float ) : Concentration of Cl- at the surface
    erf_value ( float ) : Value of the error function
    Returns ( float ) : Concentration of Cl-’’’
    C_Cl=Cs*(1-erf_value)
    return C_Cl

#The amount of concrete in the foamed concrete and in the buffer
cement_foamed=400
cement_concrete=240

#Creating the empty arrays
C_Cl_along_x1=[]
C_Cl_along_x2=[]
C_Cl_along_x3=[]
#Initial concentrations of Cl
C_cl_in_water_array=[134.3,541,2227] #mmol/kg
i=1
for C_cl_in_water in C_cl_in_water_array:
    if i==1:
        #Calculating the Cl in water in the bentonite
        C_cl_in_water_kg_m3=C_cl_in_water*(35.45/10**6) #kgCl/kgH2O
        p_clay=1400 #kg/m3
        H20_concentration=p_clay*0.55
        Cl_concentration=H20_concentration*C_cl_in_water_kg_m3
        #Calculating the Cl concentration along the x axis
        for element in x_range:
            #Checking if the penetration is large enough to be in the buffer or only in the backfill
            if element<=1.5:
```

```
                erfvalue=erf_of_x(element,D=Deff_foamed,t=t_final)
                C_Cl_foamed=(Cxt_Cl(Cs=Cl_concentration,erf_value=erfvalue)/cement_foamed)*100
                C_Cl_along_x1.append(C_Cl_foamed)
            else:
                erfvalue=erf_of_x(element,D=Deff_concrete,t=t_final)
                C_Cl_concrete=(Cxt_Cl(Cs=C_Cl_foamed,erf_value=erfvalue)/cement_concrete)*100
                C_Cl_along_x1.append(C_Cl_concrete)
        C_Cl_along_x1=np.array(C_Cl_along_x1)
    if i==2:
        C_cl_in_water_kg_m3=C_cl_in_water*(35.45/10**6) #kgCl/kgH2O
        p_clay=1400 #kg/m3
        H2O_concentration=p_clay*0.55
        Cl_concentration=H2O_concentration*C_cl_in_water_kg_m3
        for element in x_range:
            if element<=1.5:
                erfvalue=erf_of_x(element,D=Deff_foamed,t=t_final)
                C_Cl_foamed=(Cxt_Cl(Cs=Cl_concentration,erf_value=erfvalue)/cement_foamed)*100
                C_Cl_along_x2.append(C_Cl_foamed)
            else:
                erfvalue=erf_of_x(element,D=Deff_concrete,t=t_final)
                C_Cl_concrete=(Cxt_Cl(Cs=C_Cl_foamed,erf_value=erfvalue)/cement_concrete)*100
                C_Cl_along_x2.append(C_Cl_concrete)
        C_Cl_along_x2=np.array(C_Cl_along_x2)
    if i==3:
        C_cl_in_water_kg_m3=C_cl_in_water*(35.45/10**6) #kgCl/kgH2O
        p_clay=1400 #kg/m3
        H2O_concentration=p_clay*0.55
        Cl_concentration=H2O_concentration*C_cl_in_water_kg_m3
        for element in x_range:
            if element<=1.5:
                erfvalue=erf_of_x(element,D=Deff_foamed,t=t_final)
                C_Cl_foamed=(Cxt_Cl(Cs=Cl_concentration,erf_value=erfvalue)/cement_foamed)*100
                C_Cl_along_x3.append(C_Cl_foamed)
            else:
                erfvalue=erf_of_x(element,D=Deff_concrete,t=t_final)
                C_Cl_concrete=(Cxt_Cl(Cs=C_Cl_foamed,erf_value=erfvalue)/cement_concrete)*100
                C_Cl_along_x3.append(C_Cl_concrete)
        C_Cl_along_x3=np.array(C_Cl_along_x3)
    i=i+1

#Plots
plt.figure()
plt.plot(x_range, C_Cl_along_x1, label="Low salinity")
plt.plot(x_range, C_Cl_along_x2, label="Middle salinity")
plt.plot(x_range, C_Cl_along_x3, label="High salinity")
plt.axvline(1.535,color="firebrick",linestyle="--",label="Rebar")
plt.axvline(2.255,color="red",linestyle="--",label="Overpack")
plt.xlabel('Thickness (m)')
plt.ylabel('Weight percentage (Cl$^-$ wt%)')
plt.title('Chloride concentration profile')
```

```python
plt.legend()
plt.grid(True)
plt.show()
```

Listing H2: Python code for computing the concentration of Cl^{-} through the super container.

```python
    import numpy as np
import matplotlib.pyplot as plt
from scipy.special import erf

# Diffusion data
D_buffer = 1e-11
D_backfill = 1e-9
#Creating the time array
years = 1200
t_end = years * 365 * 24 * 3600
time_grid = np.linspace(13140000, t_end, 1000)
x_overpack = 2.255    #Distance of the overpack from the outside in
x_rebar=1.535    #Distance of the overpack from the outside in
#Initial concentrations of Cl-
cl1_water = 134.3  # mmol/kg
cl2_water = 541  # mmol/kg
cl3_water = 2227  # mmol/kg
cl_water_array=np.array([cl1_water,cl2_water,cl3_water])
#Functions to define the error function and the concentration profile
def profile(x:float, D:float, t:float)->float:
    '''
    Calculation of the error function for the Concentration Cl-
    Parameters :
    x ( float ) : Penetration depth
    D ( float ) : Diffusion coefficient
    t (float) : Time that passed for the species to diffuse
    Returns ( float ) : Value of the error function'''
    z = x / (2 * np.sqrt(D * t))
    return erf(z)

def concentration(cs:float, value:float)->float:
    '''
    Calculation of the Concentration Cl-
    Parameters :
    cs ( float ) : Concentration of Cl- at the surface
    value ( float ) : Value of the error function
    Returns ( float ) : Concentration of Cl-'''
    return cs * (1 - value)

#Amount of cement used in backfill and buffer to calculate the weight percentage of Cl- and evaluate corrosion
cement_backfill = 400
cement_buffer = 240
#Interface where the backfill ends and teh buffer starts
x_interface = 1.5
#Creating the empty arrays
```

```
cl_backfill_1 = []
cl_buffer_1 = []
cl_rebar_1= []
cl_backfill_2 = []
cl_buffer_2 = []
cl_rebar_2= []
cl_backfill_3 = []
cl_buffer_3 = []
cl_rebar_3= []
i=1
#Stablishing the for loop for each of the Surface Cl concentrations
for cl_water in cl_water_array:
    #Calculating the amount of Cl- in the bentonite
    cl_mass = cl_water * (35.45 / 1e6)
    rho_clay = 1400
    water_content = rho_clay * 0.55
    cl_source = water_content * cl_mass
    if i==1:
        #Setting the time loop to calculate the penetration of Cl-
        for t in time_grid:
            #Calculating the Concentration of Cl- first
            value = profile(x_interface, D_backfill, t)
            c_backfill = concentration(cl_source, value)
            c_backfill = (c_backfill / cement_backfill) * 100
            cl_backfill_1.append(c_backfill)
            #Setting up some ifs that check that if the concentration on the end of the backfill is more than one, the buffer is beginning to have Cl- into itself
            if c_backfill > 0:

                value = profile(x_overpack, D_buffer, t)
                c_buffer = concentration(c_backfill, value)
                c_buffer = (c_buffer / cement_buffer) * 100

            if c_backfill > 0:

                value = profile(x_rebar, D_buffer, t)
                c_rebar_Cl = concentration(c_backfill, value)
                c_rebar_Cl = (c_rebar_Cl / cement_buffer) * 100

            else:
                c_buffer = 0
                c_rebar_Cl=0

            cl_buffer_1.append(c_buffer)
            cl_rebar_1.append(c_rebar_Cl)
    elif i==2:
        for t in time_grid:
            value = profile(x_interface, D_backfill, t)
            c_backfill = concentration(cl_source, value)
            c_backfill = (c_backfill / cement_backfill) * 100
```

```
            cl_backfill_2.append(c_backfill)

            if c_backfill > 0:

                value = profile(x_overpack, D_buffer, t)
                c_buffer = concentration(c_backfill, value)
                c_buffer = (c_buffer / cement_buffer) * 100

            if c_backfill > 0:

                value = profile(x_rebar, D_buffer, t)
                c_rebar_Cl = concentration(c_backfill, value)
                c_rebar_Cl = (c_rebar_Cl / cement_buffer) * 100

            else:
                c_buffer = 0
                c_rebar_Cl=0

            cl_buffer_2.append(c_buffer)
            cl_rebar_2.append(c_rebar_Cl)
    elif i==3:
        for t in time_grid:
            value = profile(x_interface, D_backfill, t)
            c_backfill = concentration(cl_source, value)
            c_backfill = (c_backfill / cement_backfill) * 100
            cl_backfill_3.append(c_backfill)

            if c_backfill > 0:

                value = profile(x_overpack, D_buffer, t)
                c_buffer = concentration(c_backfill, value)
                c_buffer = (c_buffer / cement_buffer) * 100

            if c_backfill > 0:

                value = profile(x_rebar, D_buffer, t)
                c_rebar_Cl = concentration(c_backfill, value)
                c_rebar_Cl = (c_rebar_Cl / cement_buffer) * 100

            else:
                c_buffer = 0
                c_rebar_Cl=0

            cl_buffer_3.append(c_buffer)
            cl_rebar_3.append(c_rebar_Cl)
    i=i+1
#Converting the time in seconds to the time in years
time_years = time_grid / (365 * 24 * 3600)
mask = time_years >= 10

```

```python


# Plots
plt.figure()
plt.plot(time_years[mask],np.array(cl_rebar_1)[mask],label=f'Low salinity')
plt.plot(time_years[mask],np.array(cl_rebar_2)[mask],label=f'Medium salinity')
plt.plot(time_years[mask],np.array(cl_rebar_3)[mask],label=f'High salinity')
plt.xlabel('Time (years)')
plt.ylabel('Weight percentage (Cl$^-$ wt%)')
plt.title('Chloride concentration profile (rebar)')
plt.grid(True)
plt.legend()
plt.show()


plt.figure()
plt.plot(time_years[mask],np.array(cl_buffer_1)[mask],label=f'Low salinity')
plt.plot(time_years[mask],np.array(cl_buffer_2)[mask],label=f'Medium salinity')
plt.plot(time_years[mask],np.array(cl_buffer_3)[mask],label=f'High salinity')
plt.xlabel('Time (years)')
plt.ylabel('Weight percentage (Cl$^-$ wt%)')
plt.title('Chloride concentration profile (overpack)')
plt.grid(True)
plt.legend()
plt.show()
print()

print(f'The Concentration of  Cl  in the rebar is {np.array(cl_rebar_1[-1]):.3f}% in the low salinity medium, {np.array(cl_rebar_2[-1]):.3f}% in the medium salinity medium, {np.array(cl_rebar_3[-1]):.3f}%$in the high salinity medium')

print(f'The Concentration of  Cl  in the buffer is {np.array(cl_buffer_1[-1]):.3f}% in the low salinity medium, {np.array(cl_buffer_2[-1]):.3f}% in the medium salinity medium, {np.array(cl_buffer_3[-1]):.3f}% in the high salinity medium')
```

Listing H3: Python code for computing the concentration of Cl^- through time in the rebar and overpack.

```python
import numpy as np
import time

#Assesment of radiation exposure on workers in HLW disposal facility tunnels

def walk(coords:np.array, n:np.array, res:tuple, radii:np.array, crack:np.array, step:float, containers:np.array) -> np.array:
    x, y, z = coords
    crack_zp, crack_zm, crack_dpt = [crack[2] + crack[0]/2, crack[2] - crack[0]/2, crack[3]]            #[m], margins of the crack in the buffer in the z coordinate
    crack_xp, crack_xm = [crack[1]/2, -crack[1]/2]                                                      #[m], margins of the crack in the x coordinate (vertically)

    gap, h_total, h_waste, n_canister = containers                                                      #[m, m, m, -], air gap between buffers, total height including gap, height of the waste form, number of canisters measurably irradiating the worker

```

```
    t_can = radii[1] - radii[0]                                                                          #[m], radial thickness of the stainless steel canister layer
    t_ovp = radii[2] - radii[1]                                                                          #[m], radial thickness of the overpack layer

    hz_waste = h_waste/2                                                                                 #[m], half heights (all is considered using symmetry wrt z=0) of different package components
    hz_can = hz_waste + t_can                                                                            #[m], ...
    hz_ovp = hz_can + t_ovp                                                                              #[m], ...
    hz_buf = (h_total - gap)/2                                                                           #[m], ...

    rho = np.array([2.76, 7.7, 7.8, 3.7])                                                                #[g/cm3], densities of each material considered
    att_coef = np.array([7.5e-2 , 7.2e-2, 7.2e-2, 7.4e-2])                                               #[cm2/g], attenuation coefficients of each layer at 700 keV
    lin_att = rho*att_coef*100                                                                           #[m-1], linear attenuation coefficient

    attenuation = np.zeros((res))
    outside = np.ones((res))
    position = np.array([np.full((res), x), np.full((res), y), np.full((res), z - n_canister*h_total)])          #starting position of the rays is taken, expressing z in relative coordinates to the center of each evaluated canister

    count = 0
    while True:
        radial_dist = np.sqrt(position[0,:,:]**2 + position[1,:,:]**2)

        attenuation = np.where((radial_dist <= radii[0]) & (np.absolute(position[2,:,:]) <= hz_waste), attenuation + lin_att[0],                                                                                                #waste form
                               np.where(((radial_dist > radii[0]) & (radial_dist <= radii[1]) & (np.absolute(position[2,:,:]) <= hz_waste)) | ((np.absolute(position[2,:,:]) > hz_waste) & (np.absolute(position[2,:,:]) < hz_can) & (radial_dist <= radii[1])), attenuation + lin_att[1],                                                                                         #canister
                                        np.where((((radii[1] < radial_dist) & (radial_dist <= radii[2]) & (np.absolute(position[2,:,:]) <= hz_can)) | ((np.absolute(position[2,:,:]) > hz_can) & (np.absolute(position[2,:,:]) < hz_ovp) & (radial_dist <= radii[2]))), attenuation + lin_att[2],                                                                                 #overpack
                                                  np.where(((((radial_dist > radii[2]) & (radial_dist <= radii[3] - crack_dpt)) | ((radial_dist > radii[3] - crack_dpt) & (radial_dist <= radii[3]) & (((position[2,:,:] >= crack_zp) | (position[2,:,:] <= crack_zm)) | ((position[0,:,:] >= crack_xp) | (position[0,:,:] <= crack_xm))))) & (np.absolute(position[2,:,:]) <= hz_ovp)) | ((np.absolute(position[2,:,:]) > hz_ovp) & ((np.absolute(position[2,:,:]) < hz_buf) | (np.absolute(position[2,:,:]) > hz_buf + gap)) & (radial_dist <= radii[3])),        #buffer
                                                         attenuation + lin_att[3], attenuation))))
        outside = np.where(radii[3] < radial_dist, outside*0, outside)

        count += 1
        position += step*n

        #the estimation is interrupted if either all the rays have exited the shielding layers or if the ones still in have negligible intensity
        if np.sum(outside) < 1 or np.max(np.exp(-attenuation*step)*outside) < 1e-18:
            break
```

```python

    return np.exp(-attenuation*step)


def rad_frac(coords:np.array, man:np.array, res:np.array, radii:np.array, crack:np.array, step:float, containers:np.array) -> np.array:
    #Assesses the fraction of total radiation intensity emitted from the source, that reaches the worker
    x, y, z = coords
    h, w, xp, yp, zp = man
    nh, nw = res

    D = np.sqrt((y-yp)**2 + (z-zp)**2)                                              #[m], distance from emission point to center of worker
    theta = np.arctan2(z-zp, yp-y)                                                  #angle: origin - center of worker - emission point

    dA = h*w/(nh*nw)

    H, V = np.meshgrid(np.linspace(-w/2, w/2, nw), np.linspace(h/2, -h/2, nh))      #horizontal and vertical coordinate map with respect to the center of the worker

    X = xp + V                                                                      #
    Y = yp + H*np.sin(theta)                                                        #coordinates of the points on the worker in the absolute cartesian system of coordinates
    Z = zp + H*np.cos(theta)                                                        #

    R = np.sqrt((X-x)**2 + (Y-y)**2 + (Z-z)**2)                                     #matrix of distances between each point in the worker and the source point
    dom = dA*D/R**3                                                                 #matrix of "infinitesimal" solid angle elements (one for each dA of the worker). Sum of these = solid angle occupied by the worker

    n = np.array([(X-x)/R, (Y-y)/R, (Z-z)/R])                                       #matrix of normalized versors indicating the direction from the emitting point to each point on the target
    I_ratio = walk(coords, n, res, radii, crack, step, containers)                  #attenuation of the rays is assessed by "walking" from the emission point along the versors indicated in n

    return np.sum(dom*I_ratio)



#User input variables

print("----------------------Disposal facility parameters----------------------")
package_radius = float(input("Enter external radius of the disposal package [m] (minimum value = 0.25m): "))
if package_radius < 0.49/2:
    print("Error")
    quit()
store_time = float(input("Enter over-ground storage time before emplacement [years]: "))
print()

#Incidental scenario: a crack (missing slice of concrete buffer) is introduced
print("----------------!! Parameters for incidental scenario !!----------------")
```

```python
crack_w = float(input("Enter crack horizontal width [m] (enter 0 to assess undamaged disposal package): "))
if crack_w != 0:
    crack_h = float(input("Enter crack vertical width [m]: "))
    crack_z = float(input("Enter crack position along the container [m]: "))
    crack_dpt = float(input("Enter crack depth [m]: " ))
    if crack_dpt > package_radius - 0.49/2:
        print(" ")
        print("Error: crack depth superior to buffer thickness")
        print(" ")
        quit()
    step = min(crack_w/10, crack_h/10, 1e-4)                                          #1/10 is ok, 1/100 should be preferred
else:
    crack_h = 0
    crack_z = 0
    crack_dpt = 0
    step = 1e-4
crack = np.array([crack_w, crack_h, crack_z, crack_dpt])                              #width, height, position and depth of crack in the buffer
print()


print("Run started...")
start_time = time.time()
print()

#Target definition
height, width, distance = [1.83, 0.5, 1.5]                                                #[m], average dimensions of a dutch man and distance from HLW center (counted from the worker's vertical axis, perpendicularly to it)

#Control volume and waste shape definition
d_max = 0.41                                                                              #[m], radius of waste form
radii = np.array([d_max/2, 0.43/2, 0.49/2, package_radius])                               #[m], radii of waste form, stainless steel canister, carbon steel overpack and concrete buffer
z_lim = (distance - radii[0])/np.tan(np.arcsin((package_radius - radii[0])/2))            #[m], maximum value of z for which any radiation  passes through less than 2 meters of shielding (assumed fully attenuated)

z_tot = z_lim*2                                                                           #[m], length of tunnel that will be studied
Delta_x, Delta_y, Delta_z = [d_max, d_max, z_tot/2]                                       #[m], grid range -> will define margins of the matrix used to describe HLW points (Delta_z uses symmetry!)

Dz_waste = 1.325                                                                          #[m], height of the vHLW in one canister
Dz_DispPack = 2.5                                                                         #[m], height of the disposal package
gap = 0.04                                                                                #[m], gap spacing between canisters
Dz_withgap = Dz_DispPack + gap

#x is the height coordinate, y is the horizontal coordinate, z indicates the depth along the tunnel/package axis

#Waste volume grid parameters
nx, ny, nz = [23, 23, 105]                                                                #grid points along axes x,y,z
dx, dy, dz = [Delta_x/nx, Delta_y/ny, Delta_z/nz]                                         #[m]
```

```
#Worker surface grid parameters
nh, nw = [161, 55]                                                                       #!!!   both must be ODD for proper small-crack assessments   !!!

#Central coordinates of target
divot_depth = 0.4                                                                       #[m], depth of the tunnel divot
xp, yp, zp = [-package_radius + divot_depth + height/2, distance, 0]                    #central coordinates of the worker
man = np.array([height, width, xp, yp, zp])

middlepoints = np.array([0])
n_canisters = int(np.ceil(z_tot/2/Dz_withgap))                                          #number of canisters measurably irradiating the worker
for i in range(1, n_canisters):
    middlepoints = np.append(middlepoints, Dz_withgap*i)

tot_frac = 0
counter = 0
L_counter = 0
for k in range(nz):
    print("Completed percentage ", k/nz*100, "%")
    z = (k + 0.5)*dz
    if np.min(np.absolute(middlepoints - z)) <= Dz_waste/2:                             #if true, then the point is in a HLW occupied z coordinate
        n_canister = np.argmin(np.absolute(middlepoints - z))
        L_counter += 1
        containers = [gap, Dz_withgap, Dz_waste, n_canister]

        for i in range(nx):
            x = (i + 0.5)*dx - Delta_x/2
            for j in range(ny):
                y = (j + 0.5)*dy - Delta_y/2

                coords = [x, y, z]
                r = np.sqrt(x**2 + y**2)

                if r < d_max/2:                                                         #if true, then the point is in the HLW volume
                    tot_frac += rad_frac(coords, man, [nh, nw], radii, crack, step, containers)/(4*np.pi)
                    counter += 1

BU = 120                                                                                #Build up factor, takes into account scattering effects inside the shielding redirecting radiation towards the worker
tot_frac = tot_frac*BU/counter                                                          #Averagers exposure over all points in the waste, taking BU increase into accunt


#Activity calculation
sA0 = 1e11                                                                              #[Bq/cm3], assumed to be fully due to 137Cs -> 137mBa -> 137Ba
lin_att_human = 0.032*0.985                                                             #[cm-1], mass energy absorption coefficient * density
```

```

sAt = sA0*np.exp(-np.log(2)/30.08*store_time)                                           #[Bq/cm3]
At = sAt*(d_max**2/4*np.pi*z_tot*L_counter/nz)*1e6                                      #[Bq]

E_tot = At*0.662e6*1.602177e-19*tot_frac                                                #[J/s], again assumed to be fully due to 137Cs -> 137mBa -> 137Ba
dep_frac = 1 - np.exp(-20*lin_att_human)                                                #the worker is assumed to be 100% water and 20cm thick
E_dep = E_tot*dep_frac
mass = 85                                                                               #[kg], mass of worker

final_time = time.time()

print()
print("Calculation completed in", time.strftime("%H:%M:%S", time.gmtime(final_time - start_time)))
print()
print("-------------- Data for radius =", package_radius , "and storage time =", store_time, "-----------------")
print("Shielding efficiency: intensity reaching the worker is", tot_frac*100, "% of that emitted by the waste")
print("Radiation exposure [muSv/s] = ", E_dep/mass*1e6)
print("Maximum allowable time <6mSv [h]: ", 6/(E_dep/mass*1e3*3600))
print()
```

Listing H4: Python code for computing radiation exposure for an average worker as a function of buffer thickness, pre-emplacement storage time and, if modeling an accidental scenario is desired, size and depth of a crack in the buffer.

Declaration of AI Use

This section serves to explain the use of AI tools throughout the CDP project.

In this project, AI was used for several purposes:

- Overleaf formatting
- BibTeX formulation
- Spelling checks

For the overleaf formatting, AI was mainly used to aid in making large tables, such as tables 11 16,18. These sometimes required specific packages to get the intended layout. When using AI for formatting, the tables were left empty, so that the data in the table is not influenced by the AI. After compiling, a visual check was performed to ensure the readability of the table.

For the BibTeX formulation, the DOI of several sources was put in, with the request of returning the BibTeX for the source. This BibTeX was compared to the data in the publication to ensure it is correct. Here it was found that in some cases the AI would not correctly cite the paper, instead putting in an incorrect source/authors or other information. Since the provided BibTeX files were checked with the source itself, these mistakes were filtered out.

In the use of AI for spelling checks, certain sentences were provided to the AI with the request of checking the spelling and grammatical structure. The output was then evaluated, and suggestions were manually incorporated in the text. By being critical to the output and never directly copying the suggestions into the text, it was ensured no mistakes made by the AI ended up in the text.